**The Dissertation Committee for Mohsen Nakhaeinejad Certifies that this is the approved version of the following dissertation:**

# Fault Detection and Model-Based Diagnostics in Nonlinear Dynamic Systems

**Committee:**

Michael D. Bryant, Supervisor

Mircea D. Driga

Eric P. Fahrenthold

Benito Fernandez

Raul G. Longoria

# Fault Detection and Model-Based Diagnostics in Nonlinear Dynamic Systems

**by**

**Mohsen Nakhaeinejad, B.S; M.S.**

**Dissertation**

Presented to the Faculty of the Graduate School of

The University of Texas at Austin

in Partial Fulfillment

of the Requirements

for the Degree of

**Doctor of Philosophy**

**The University of Texas at Austin**

**December 2010**

# Dedication

To my parents, for believing in me and providing me endless love and support. I could not have done this without them.

# Acknowledgements

I am grateful to all the people who were with me throughout my Ph.D. program. Most special appreciation goes to my advisor, Professor Michael D. Bryant, for his help and guidance. It was an honor to work with him. Special thanks go to my committee members, Prof. Benito Fernandez, Prof. Longoria, Prof. Fahrenthold, and Prof. Driga for their interests in my work and carefully reviewing this dissertation. I was very fortunate to have a great and knowledgeable Ph.D. committee. Special appreciation goes to Prof. Bob Randall from The University of New South Wales, Australia for his valuable advice and guidance and for providing experimental data of bearings with rough surface faults. Thanks to Prof. Dragan Djurdjanovic, Jaewon Choi, Sankar Rengarajanin, and other colleagues in the Department of Mechanical Engineering for their valuable and helpful discussions. Finally, this work was not possible without endless love and support of my parents, and my brothers. I heartily thank all of them.

# Fault Detection and Model-Based Diagnostics in Nonlinear Dynamic Systems

Publication No._____

Mohsen Nakhaeinejad, Ph.D.

The University of Texas at Austin, 2010

Supervisor: Michael D. Bryant

Modeling, fault assessment, and diagnostics of rolling element bearings and induction motors were studied. Dynamic model of rolling element bearings with faults were developed using vector bond graphs. The model incorporates gyroscopic and centrifugal effects, contact deflections and forces, contact slip and separations, and localized faults. Dents and pits on inner race, outer race and balls were modeled through surface profile changes. Experiments with healthy and faulty bearings validated the model. Bearing load zones under various radial loads and clearances were simulated. The model was used to study dynamics of faulty bearings. Effects of type, size and shape of faults on the vibration response and on dynamics of contacts in presence of localized faults were studied.

A signal processing algorithm, called feature plot, based on variable window averaging and time feature extraction was proposed for diagnostics of rolling element bearings. Conducting experiments, faults such as dents, pits, and rough surfaces on inner race, balls, and outer race were detected and isolated using the feature plot technique.

Time features such as shape factor, skewness, Kurtosis, peak value, crest factor, impulse factor and mean absolute deviation were used in feature plots. Performance of feature plots in bearing fault detection when finite numbers of samples are available was shown. Results suggest that the feature plot technique can detect and isolate localized faults and rough surface defects in rolling element bearings. The proposed diagnostic algorithm has the potential for other applications such as gearbox.

A model-based diagnostic framework consisting of modeling, non-linear observability analysis, and parameter tuning was developed for three-phase induction motors. A bond graph model was developed and verified with experiments. Nonlinear observability based on Lie derivatives identified the most observable configuration of sensors and parameters. Continuous-discrete Extended Kalman Filter (EKF) technique was used for parameter tuning to detect stator and rotor faults, bearing friction, and mechanical loads from currents and speed signals. A dynamic process noise technique based on the validation index was implemented for EKF. Complex step Jacobian technique improved computational performance of EKF and observability analysis. Results suggest that motor faults, bearing rotational friction, and mechanical load of induction motors can be detected using model-based diagnostics as long as the configuration of sensors and parameters is observable.

## Table of Contents

# List of Tables

# List of Figures

# Chapter 1

# Introduction

## 1.1 Motivation and Objectives

Rotating components, motors and rolling element bearings are among the most popular machine elements in industry. A well-developed diagnostic system can reduce industry costs, due to production outage, energy consumption, and maintenance and increases safety for human, environment and machine. In working conditions under high load rates and speeds, bearings are readily susceptible to different types of faults and failure. Based on statistical research [1], bearing faults are the most common source of the failure in induction motors, see Figure 1. Early detection of bearing faults allows replacement of the bearing, rather than replacement of the whole rotating machine.

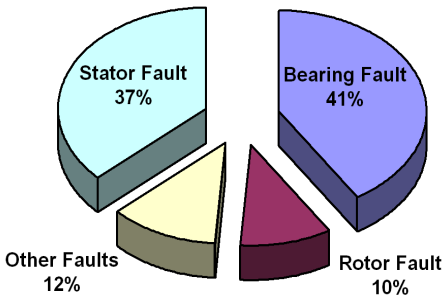


Figure 1 Distribution of failures in induction motors

Condition monitoring and diagnostics of rolling element requires a good understanding of the system with faults interactions. A detailed physics-based model can be used to study dynamics of rolling element bearings. Available models of rotating machinery and rolling element bearings are not detailed enough for a direct one to one

correspondence between the model parameters and the physical system parameters. Several analytical models, modeling software, and virtual design tools for rolling element bearings and rotating machines have been developed. But there is no generic universal platform for the whole system. Bond graphs introduced by Paynter [2] can create a detailed model of rotating machinery which can be integrated into other elements of the machine. Each aspect of the system such as rotor dynamics, bearings dynamics, tribology issues of bearings, contact flexibilities, dynamics of faults, and contact can be modeled separately, and integrated.

Diagnostics in rotating machinery can be either signal-based or model-based. Model-based diagnosis requires a detailed model. The model should exhibit a direct one to one correspondence between parameters of the model and components in the physical system, and incorporate all critical effects of the device into the model including faults, and clearly define how a healthy or faulty machine behaves. Bond graphs also can be used for modeling in model-based diagnostics. An accurate and efficient parameter tuning technique is another essential task to model-based diagnostics. The complexity and nonlinearity of the system make parameter tuning more difficult. Also, uncertainties in the model makes the parameter tuning more complicated. Therefore an optimum parameter tuning technique, which is applicable for any integrated model, is crucial to model-based diagnostics. A super detailed model with an efficient parameter tuning can highly improve the performance of model-based diagnostics. However, the performance also highly depends on the amount of information from sensors. If measured signals do not provide enough information to track the system, the system is called unobservable and diagnosis may fail. Therefore, observability analysis needs to be studied before developing a model-based diagnostic system.

Model-based diagnostics detects machine degradation by monitoring states and parameters of the system. Small changes in parameters can be detected. However, for severe damage from shocks, collision, or other instantaneous damage modes, parameters change too fast for the model, or the behavior of the altered system is beyond the scope of the model. A signal-based diagnostic system, in conjunction with the model-based module, can alert of an impending catastrophe. The signal-based technique will monitor time and frequency features of measured signals to provide fault indicators and for detailed fault information model-based diagnostics will be employed.

The objective of this research is to describe rolling element bearings with faults by developing a super model, develop a signal-based machine diagnostics technique to provide fault indicators, and provide a model-based diagnostic framework including modeling, observability analysis and parameter tuning.

## 1.2 BACKGROUND

### 1.2.1 Machine Diagnostics

Machine diagnostics may be classified into signal-based and model-based techniques [3]. In signal-based diagnostics, the system output is processed to detect and analyze faults, and the plant is studied as a black box, based solely on inputs and outputs. Simplicity and ease of implementation have made signal-based methods popular throughout industry. Signal-based diagnostic systems can be implemented through different approaches such as limit checking, spectrum analysis or logic reasoning[4]. Limit checking compares features of signals against fixed thresholds, and detects faults when signals exceed a threshold. Spectrum analysis detects faults based on the fact that most plant variables exhibit a distinctive frequency spectrum under normal conditions

and any deviation from the normal spectrum is a signature of abnormality [3]. Logic reasoning compares the current behavior of a system against previously stored behavior.

On the other hand, the model-based diagnostics uses a model of the system to analyze performance. Physical values or any change in model can be observed by tuning the parameters of the model. Once the model is constructed, parameters in the model have to be identified. Some parameters can be directly measured, calculated, approximated, or assumed. Given measurements from the machine, parameters are tuned until simulations closely mimic measurements. For a healthy system, this produces a set of nominal parameter values that describes a fault-free situation and for a faulty system, this can find a set of changed parameter values that describes faults. A well-developed model-based diagnostics with the detailed model can provide early detection of small faults, more precise fault isolation, fault detection in closed loop systems, and process supervision in transient states [4]. Figure 2 shows typical structure of signal-based diagnostic system, which consists of residual generation and residual evaluation.

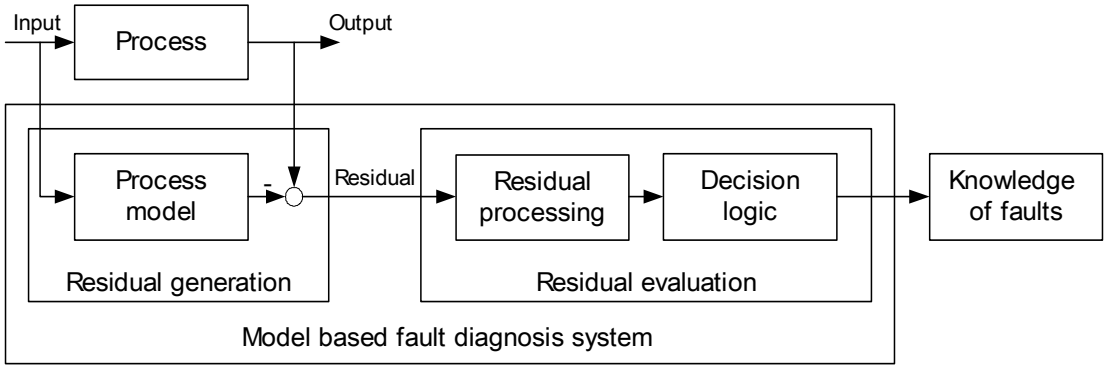


Figure 2 General structure of model-based diagnosis [5]

### 1.2.2 Diagnostics of Rolling Element Bearings

Under high loads and speeds, rolling element bearings are susceptible to faults and failures. Early detection and precise isolation of bearings can increase safety and decrease maintenance costs by reducing machine downtime. Several advanced signal processing schemes to improve reliability of machine diagnostics and prevent misdiagnosis have been developed. Yet, industry mostly relies on vibration frequency techniques. For industry, the problem is not lack of sophisticated diagnostic techniques but scarcity of simple yet reliable approaches to help unskilled operators for making important decisions without a specialist. Model-based diagnostics detects machine degradation by monitoring states and parameters of the system. Small changes in parameters can be detected. However, for severe damage from shocks, collision, or other instantaneous damage modes, parameters change too fast for the model, or the behavior of the altered system is beyond the scope of the model. Therefore, a signal-based diagnostic system, in conjunction with the model-based module, can alert of an impending catastrophe.

Bearing faults, comprising 41% of failures in induction motors [6] are important in machine diagnostics. Also, in many industrial applications bearing failures can damage other elements of the machine and enlarge machine downtime. Non-stationary signals and dynamic complexity of rolling element bearings make bearing diagnostics challenging. Various sensor signals can render information on faults, to monitor health condition. Wear particle [7] and lubricant inspections [8] are tribological techniques. Common non-destructive techniques are ultrasonic tests [9], thermography [10], magnetic flux and current measurements in electrical machines [11], acoustic emission [12], and vibration analysis from accelerometers or displacement gauges. Oscillatory motions produce vibrations containing information on health of the machine. Vibration-

based techniques are the most common methods categorized as time, frequency, and time-frequency techniques.

Time-domain statistical analysis investigate time features of signals such as mean, RMS, kurtosis, skewness, crest factor, impact factor, shape factor, etc [13] to evaluate faults, but neglect frequency contents. Also, randomness and irregularities in waveform vibration signals from bearing faults sometimes mislead time-based diagnosis systems. Frequency-based techniques, the most popular approaches, extract spectra contents by signal processing. Extensive research and successful techniques have been reported for frequency-based diagnostics of bearing [14]. Recent works on bearing diagnostics using envelope analysis were promising [15]. However, selection of the best demodulation band in envelope analysis is always challenging [16]. Ho and Randall [17] have demonstrated that a self-adaptive noise cancellation method, in conjunction with envelope analysis improves bearing diagnostics. In general, frequency techniques, based on identification of bearing fault frequencies, are often affected by fault types and loading conditions [18]. For instance, ball faults generate chaotic vibrations due to three dimensional rotations of balls, and inner race faults produce modulated vibrations due to load zone effects. Pure frequency analysis of signals can miss time information of original signals. Also, filtering used in frequency techniques might remove unwanted signals useful to diagnostics.

Recent time-frequency approaches such as wavelet transform [18, 19], Wigner-Ville distribution [20, 21], and synchronous averaging of time frequency distributions have been widely acknowledged [22]. Zhu [23] suggested time-synchronous averaging based on specific frequency references with fast Fourier transform to extract periodic signals from noisy signals. A time-domain averaging technique combined with wavelet analysis was proposed in [24] to extract fault information. However, these techniques

provide no information on time features. Despite the extensive research in bearing diagnostics, still a reliable time-feature diagnostic technique that provides frequency information with minimal data processing of unfiltered signals is highly desirable.

### 1.2.3 Modeling of Rolling Element Bearings

Several modeling software and virtual design tools have been developed. Many available models represent dynamics of rolling element bearings, but, a generic modular model which can be adjusted based on the complexity of the system to represent dynamics of both normal and defective bearings is not available yet. In 2003, a workshop on Virtual Machine Design was held at the Purdue University to define requirements for the next generation of analytical design software for the rotating components [25]. The objective was to evaluate the current state of the art in the virtual rotating machine design and to discuss a strategy to eventually integrate all analytical software under a common platform. Analytical approaches and software, presented and discussed in this workshop, addressed the following aspects of rotating components: bearing dynamics, rotor dynamics, finite element software for heat transfer and stress analysis, computational dynamics, solid modeling, and tribological aspects of bearings. Twelve presentations covered all topics listed above. Although this workshop showed the diversity of the codes and software packages available for rotating components, there is no universal compilation platform. Each company or institution has its own developed closed source software package, which impedes integration of codes into a holistic package. Finally, they found that it would be challenging to implement a modular modeling approach that allows software interchange under a generic universal platform.

Despite the long history of dynamic modeling of rolling element bearings, relatively few models consider faults. Most simplify models or neglect the details of faults. In 1960, Jones introduced bearing element stiffness, damping, constraint forces, and moments [26]. In 1979, Gupta [27] introduced a 6-DOF (degree of freedom) model of a bearing and validated the model experimentally. In early 1980s, McFadden and Smith [28] incorporated localized defects of bearings using impulse functions. Assuming a rotor-bearing system with a stationary outer ring, Afshari and Loparo [29] introduced a one dimensional linear time invariant state space model, see Figure 3(a). Adams [30] presented an analytical 29-DOF model of a shaft supported by two rolling element bearings using Lagrange's approach, assuming only radial motion of the balls with no contact slip, see Figure 3(b). Harsha [31] developed an analytical model using Lagrange's approach, assuming no slip and no friction between balls and races. Incorporating gyroscopic effects and shaft bending, Fawzi [32] formulated dynamics of rotor- bearing systems using finite elements and Lagrange's equations. In 2002, Liew et al. [33] obtained a 5-DOF analytical model of angular contact ball bearing, including bearing centrifugal loads and axial and tilting stiffness effects.

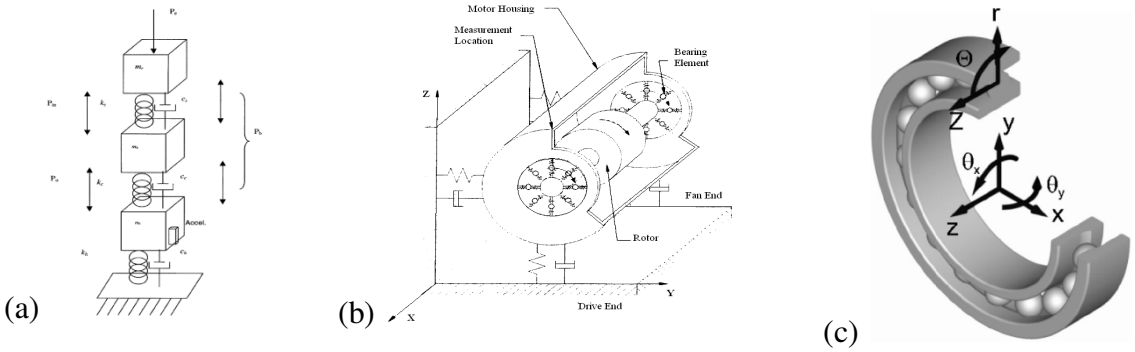


Figure 3 (a) 3-DOF model of the rolling element bearing by Afshari [29], (b) 29-DOF model of the rotor-bearing model by Adams [30], and (c) 5-DOF model of the ball bearing by Liew [33]

In 2003, Sopanen and Mikkola's model of a deep-groove ball bearing included localized and distributed defects, Hertzian contact deformations, and elastohydrodynamic (EHD) effects [34, 35], but neglected centrifugal effects and slip between components. Analytical models by Jang and Jeong [36] and a 5-DOF (degree of freedom) model by Ghangqing and Qingyu [37] considered the waviness faults neglecting contact slip and contacts separations. Patil et al. [38] studied dynamics of defects in bearings using a planar model neglecting slip, centrifugal force and gyroscopic moments. Wensing developed a finite element model of rolling element bearings [39]. Sassi and Badri [40] developed a simple 3-DOF model of ball bearings and introduced a numerical model to predict damaged bearing vibrations. Karkkainen et al. [41] studied dynamics of rotor systems with misaligned retainer bearings. Ashtekar et al. [42] used a dry contact elastic model to modify the Hertzian relationships for contacts with small surface faults. Also, they used superposition to include the effects of dents or bumps smaller than the Hertzian ellipse on bearing dynamics [43] assuming the contact stiffness $K$ is unaffected by the presence of faults.

### 1.2.4 Observability and Parameter Tuning for Induction Motors

Faults and degradation in machines are related to the change of states or parameters. A model-based diagnostic system consisting of physics-based model, parameter tuning module, and decision making unit shown in Figure 4 tracks states and parameters of the system to detect degradation or to predict components failure [44]. Observations $\mathbf{Y}$ measured by sensors are compared to the corresponding outputs $\widehat{\mathbf{Y}}$ of the model. The difference generates the residual $\mathbf{r}$. The parameter tuning module minimizes the residuals by tuning the states $\mathbf{X}$ and parameters $\mathbf{P}$ of the model. The decision making

and fault assessment units detect or predict the occurrence of faults by interpreting changes of parameters.

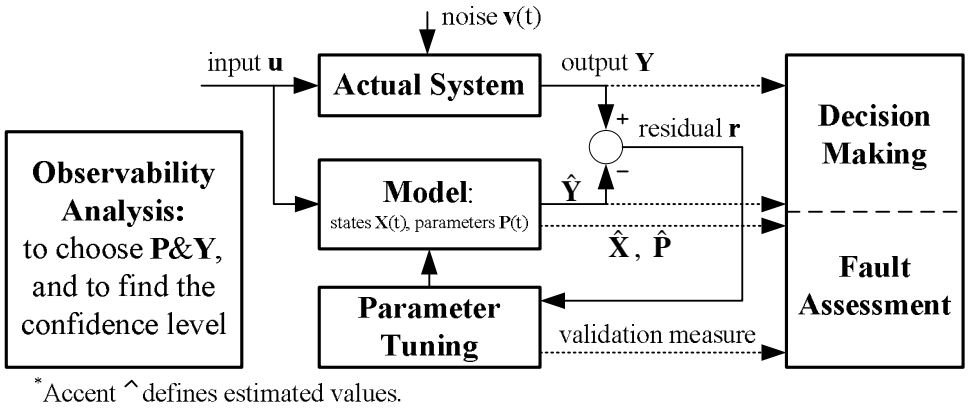


Figure 4 General Structure of the Model-Based Diagnostics

Beside the simplicity of the process, implementing a practical model-based diagnostic system is challenging. Tasks such as detailed physics-based modeling, designing a proper sensor configuration to get enough information from the system, parameter tuning in highly nonlinear systems with efficient computational performance, and a reliable validation technique to evaluate the accuracy of the diagnosis are still much in demand.

Bond graph modeling, an energy-based approach, with modularity that permits system growth and integration [2], is a good modeling solution for model-based diagnostics. Kim and Bryant's [45, 46] introduced a physically explicit representation of a squirrel cage motor with bond graph model, incorporating a magnetic field and mechanical parts as shown in Figure 5. Lee and Bryant [47] embedded the Finite Element Method (FEM) into bond graphs and combined FEM techniques for bending of rotating shafts with Hubbard's bond graph of motion of a flywheel in a rotating reference frame [48]. Afterward, Oh [49] developed an extended bond graph model of a squirrel cage

induction motor, consisting of rotor, stator, and journal bearings. Also, in [50] a bond graph model of the squirrel cage induction motor and centrifugal pump was developed and model-based diagnostics of the system was studied. But rolling element bearings are not modeled in detail in this research. Therefore, bearing faults cannot be detected and isolated by this model.

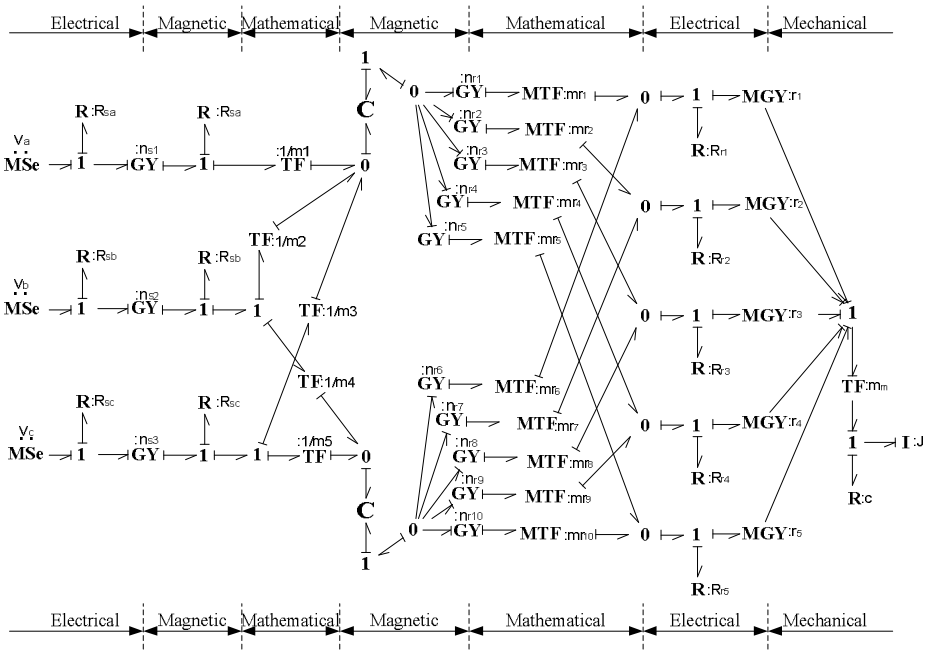


Figure 5 Bond graph model of a 3-phase induction motor with 5 rotor bars [46]

Observability analysis is a major and crucial task in model-based diagnostics. If sensors do not provide enough information to track and distinguish states or parameters, the system is unobservable. In model-based diagnostic of unobservable systems, diagnosis may fails or the parameter tuning converges to incorrect values, misleading the decision making unit. Therefore, observability analysis to determine the presence of enough information in measured signals for estimation of states and parameters is needed. Results will find effective combinations of sensors and parameters for a model-

based diagnostics and provide a systematic procedure to select proper sensors and parameters. Also, for sensor fault detection, an observability analysis can detect redundant sensors and evaluates levels of redundancy.

Previous research on observability for induction motors include linear observability analysis for the Kalman filter [51], observability of induction motors at low frequencies [52] and under sensorless conditions [53], observability tests in design of the controllers [54], linear observability of induction motors under faults [55], observability of a simplified model of the induction motor for speed detection [56], linear observability through bond graphs for online fault detection and isolation [57], observability analysis of deep-space autonomous navigation system [58, 59], and Identifiability analysis using Markov parameters [60]. Few works searched for a general solution. A general approach to nonlinear observability to support design for model-based diagnostics is still needed.

Estimation of states and parameters in induction motors were extensively studied during last few decades, including EKF-based (Extended Kalman Filter) parameter estimation using a simple stochastic model [61], sensitivity analysis [62] adaptive genetic algorithm [63], and output optimizations [64, 65]; model-based mapping identification from transient data [66]; empirical model-based diagnosis for induction motors using neural networks and signal processing methods [67]; EKF state estimation of induction motors for control purposes [68, 69]; parameter estimation of induction motors for broken bar detection [70, 71]; and stator winding fault detection using an adaptive observer [72]. A general approach to parameter tuning for model-based diagnostics that includes a systematic scheme to set up a model-based diagnostic system with an efficient parameter tuning algorithm is still in demand.

## 1.3 DISSERTATION OVERVIEW

This chapter introduced motivation and objectives of the research. Signal-based and model-based diagnostics were introduced. Backgrounds of diagnostics and dynamic modeling of rolling element bearings, observability analysis, and parameter tuning of induction motors in model-based diagnostics were reviewed.

Chapter 2 will develop a detailed vector bond graph model of rolling element bearings. Multibody dynamics of bearings including elastic deflections, non-linear Hertzian contacts, tractions, contact slips, centrifugal effects and surface separations will be modeled. Localized faults such as dents and pits will be modeled as surface profile changes, and incorporated into the model.

In chapter 3, the bearing model with inner race faults, outer race faults, and ball faults will be simulated using the model of chapter 2 and validated with experiments. Dynamic aspects of the bearing such as centrifugal effects and contact impact forces due to localized faults will be studied. Also, effects of geometry and type of faults, bearing clearance, and radial loads on vibration response will be studied using the model.

Chapter 4 will propose and formulate a signal-based diagnostic technique, called feature plot, based on time features extraction and variable window averaging. A diagnostics algorithm using the feature plot technique will be applied to 28 sets of bearing measurements with different faults and sensor conditions. Time features such as skewness, Kurtosis, peak value, crest factor, impulse factor and mean absolute values will be used in feature plots to detect and isolate faults. Also, performance of the feature plot technique for diagnostics of bearing mild faults such as surface roughness will be shown.

Chapter 5 and 6 will develop a model-based framework consisting of bond graph modeling, nonlinear observability analysis, and parameter tuning for induction motors. A physics-based bond graph model of the induction motor will be developed, simulated,

and validated with experiments. Nonlinear observability analysis based on Lie derivatives will be introduced. Singular value decomposition of the observability matrix will determine the most and least observable configurations of measurements and parameters. Complex step Jacobian technique will be used to improve computational performance of the observability and parameter tuning analysis. A continuous-discrete Extended Kalman Filter (EKF) with dynamic process noise will be used for parameter tuning to detect stator and rotor faults and to estimates bearing friction and mechanical loads on the motor. Finally, chapter 7 will present summary, conclusions, and contributions of the research with recommendations for future work.

# Chapter 2

# Bond Graph Modeling of Rolling Element Bearings

## 2.1 INTRODUCTION

Little has been done in detailed bond graph modeling of rotating systems [49, 73, 74], including rolling element bearings, multibody dynamics, tribological aspects and localized defects. Bond graphs are energy-based modeling techniques, with modularity that permits system growth. Different submodels can be integrated into a large system. Despite the apparent simplicity of rolling element bearings, the presence of faults complicates dynamics. Most existing models cannot fully explain dynamic behavior of bearings with faults since simplified models do not fully contain details of the fault. Here, tribological aspects of rolling element bearings, non-linear contacts and surface defects are modeled in detail separately, and integrated into a unified bond graph model. The goal is generic models of systems which can be simple or detailed, based on the complexity of the system, needed to support model-based diagnostics.

A detailed model of Rolling Element Bearings (REB) with a direct physical correspondence between parameters of the model and physical system components and faults is presented. First, multibody dynamics of bearings including elastic deflections with non-linear Hertzian contacts, tractions with contact slips, and surface separations are modeled in a generic bond graph. Localized faults such as dents and pits are modeled as surface profile changes, and incorporated into the bond graph.

## 2.2 SYSTEM AND MODEL DESCRIPTIONS

A deep groove ball bearing consisting of balls, inner race and outer race was modeled as a multibody system using vector bond graphs. Nonlinear contact stiffness, contact damping effects, contact slip, contact separations, bearing clearance, traction between elements, rotational friction torques, and localized faults were included. Axial motion, lubrication effects, structural flexibility except at contacts, and dynamics of the cage were neglected. A 33-DOF bond graph model was constructed for a bearing with nine balls and two rings (11 bodies). The model can be extended to any n-body rolling element bearing with $(3 \times n)$-DOF in planar motions and $(6 \times n)$-DOF in 3D motions.

## 2.3 GEOMETRY CONSIDERATIONS

Assuming planar motions, each element of the rolling element bearing has three DOF. Figure 6 shows a three-element rolling system representing inner race (a), ball (b) and outer race (c) in contact, with global fixed coordinate system XYZ and rotating body coordinates $x^i y^i z^i$ defined for each moving element, and coincident with the principal axes of moving elements.

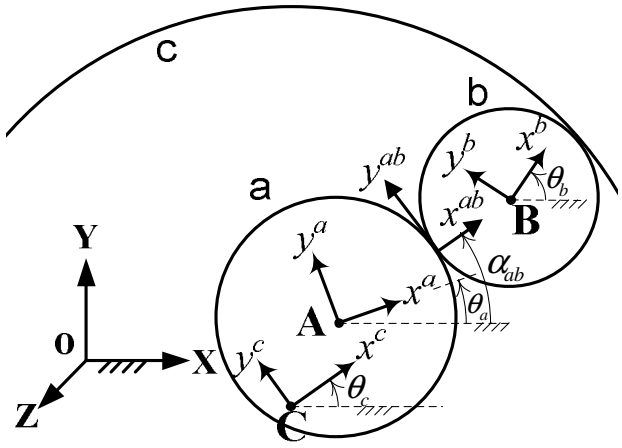


Figure 6 Geometry and coordinates of a three-body rolling element system

Misalignments and eccentricity can be included by relocation of inner race and outer race centers. Position and orientation of each element can be described in the global coordinate system by a position vector $\mathbf{R}_{\mathrm{i}} = [\mathrm{X_i} \quad \mathrm{Y_i} \quad \mathrm{Z_i}]^{\mathrm{T}}$ and $\theta_i$ respectively. For each contact between two elements $i$ and $j$, a moving contact frame $x^{ij} y^{ij} z^{ij}$ with origin at the contact is defined with orientation $\alpha_{ij}$ described in the global coordinate as

$$\alpha_{ij} = \mathrm{Arctan}\left(\frac{\mathrm{Y_i} - \mathrm{Y_j}}{\mathrm{X_i} - \mathrm{X_j}}\right). \tag{1}$$

Any vector $\mathbf{X}$ defined in the global frame can be transformed to a vector $\overline{\mathbf{X}}$ in the moving frame via

$$\overline{\mathbf{X}} = \mathbf{T}\mathbf{X} \tag{2}$$

where transformation matrix $\mathbf{T}$ for the body coordinate systems is:

$$\mathbf{T}^i = \begin{bmatrix} \cos\theta_i & \sin\theta_i & 0 \\ -\sin\theta_i & \cos\theta_i & 0 \\ 0 & 0 & 1 \end{bmatrix} \tag{3}$$

and for the contact coordinate systems is

$$\mathbf{T}^{ij} = \begin{bmatrix} \cos\alpha_{ij} & \sin\alpha_{ij} & 0 \\ -\sin\alpha_{ij} & \cos\alpha_{ij} & 0 \\ 0 & 0 & 1 \end{bmatrix}. \tag{4}$$

## 2.4 CONTACT MODELING

### 2.4.1 Contact Stiffness and Damping

According to Hertzian theory [75] the load-deflection relation in the $x$ direction for the contact between the two bodies with different radii of curvature in a pair of principal planes as shown in Figure 7 is

$$F = K\delta^{3/2}. \tag{5}$$

where the contact force $F$ is in N, deformation $\delta$ is in mm and the contact stiffness $K$ is in $\mathrm{N/mm^{2/3}}$.

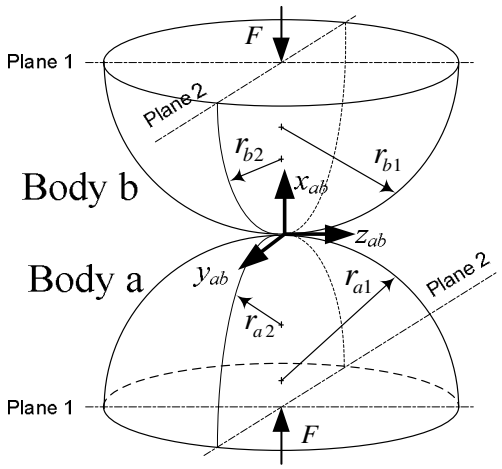


Figure 7 Geometry of two curved bodies (a) and (b) in contact under the normal force $F$

The contact stiffness $K$ is defined as

$$K = \frac{2E\sqrt{2}}{3\delta^{*3/2}\left(\sum\rho\right)^{1/2}\left(1-\upsilon^2\right)} \tag{6}$$

where $E$ is the modulus of elasticity in MPa, and $\rho$ is the curvature in 1/mm defined as $\rho = 1/r$ and the curvature sum $\sum \rho$ is

$$\sum\rho = \frac{1}{r_{a1}} + \frac{1}{r_{a2}} + \frac{1}{r_{b1}} + \frac{1}{r_{b2}}. \tag{7}$$

Subscripts $a$ and $b$ refer to bodies $a$ and $b$ and subscripts 1 and 2 refer to the bodies principal planes, in which curvatures are defined for each body. In rolling element bearings, $\Sigma\rho$ includes main curvatures of ball and raceway, as well as side groove curvatures, considering the sign convention for convex and concave surfaces. In Eq. (6),

$\delta^*$ is a dimensionless deflection factor graphed by Harris [75] as a function of curvature difference $F_\rho$ defined as

$$F_\rho = \frac{\left(\frac{1}{r_{a1}} - \frac{1}{r_{a2}}\right) + \left(\frac{1}{r_{b1}} - \frac{1}{r_{b2}}\right)}{\sum \rho}. \tag{8}$$

Note that the order of planes 1 and 2 should be selected in such a way that $F_\rho$ is positive. For computational applications, the curvature function $F_\rho$ is formulated as [76]

$$\delta^* = -327.61 + 1883.34 F_\rho - 3798.11 F_\rho^{\,2} + 3269.62 F_\rho^{\,3} - 1026\, F_\rho^{\,4}.$$

Since contact damping in ball bearings is relatively small, a constant damping value, based on the average load, can be used in the model. Kramer [77] estimated bearing damping by frequency analysis of the equivalent linear spring-mass-damper system as

$$b = k(0.25 \text{ to } 2.5)\times 10^{-2} \qquad (N.s/\text{mm}) \tag{9}$$

where $k$ is the equivalent linear stiffness of the bearing in N/mm. Here, $b$ is selected as $b = 10^{-2}k$ (N.s/mm). Therefore, the normal contact force including damping force along $x_{ab}$ is

$$F_x = K\delta^{3/2} + b\dot{\delta}, \tag{10}$$

where $\dot{\delta}$ is the first derivative of the contact deformation in mm/s. Note that, when faults are smaller that the Hertzian contact ellipse, the Hertzian contact relationships should be modified for more accurate results [42, 43]. Here, it is assumed that Hertzian contact relationship is valid for contacts with faults.

### 2.4.2 Traction Model

Based on the rolling or slip regions, the traction model follows different behavior with different coefficient of friction. Kragelsky et al. [78] described the dry contact coefficient of the friction as a function of sliding speed as

$$\mu = (C_1 + C_2 s^2) e^{-\lambda s^2} \operatorname{sign} s + C_2 s$$

where $C_1, C_2$ and $\lambda$ are constants obtained experimentally based on the materials and surfaces. Here the traction force is modeled using traction-slip behavior in elastohydrodynamic contacts [79]. Traction forces in directions $y_{ab}$ and $z_{ab}$ are functions of the normal force and the friction coefficient as

$$F_y = \mu F_x . \tag{11}$$

The friction coefficient can be calculated based on the contact lubrication modes, determined by the oil film parameter $\Lambda$ (a ratio of oil film thickness and contact surface roughness) [80] as

$$\mu = \begin{cases} \mu_{bd} & \Lambda < 0.01 \\ \dfrac{\mu_{bd} - \mu_{hd}}{(0.01 \text{ to } 1.6)^6} (\Lambda - 1.5)^6 + \mu_{hd} & 0.01 \le \Lambda < 1.5 \\ \mu_{hd} & 1.5 \le \Lambda \end{cases} \tag{12}$$

Friction coefficient $\mu_{hd}$ under hydrodynamic lubrication mode is a function of EHD parameters and temperature. Under boundary lubrication mode, friction coefficient $\mu_{bd}$ is a function of slide-roll ratio $s$ as

$$\mu_{bd} = (-0.1 + 22.28 s)\, e^{(-181.46 s)} + 0.1 . \tag{13}$$

Therefore, assuming planar motion $(F_z = 0)$, the contact force vector consisting of stiffness, damping and traction forces as a function of contact $\delta$, $\dot{\delta}$, and slip $s$ is given by

$$\mathbf{F} = \begin{bmatrix} F_x \\ F_y \\ F_z \end{bmatrix} = \begin{bmatrix} K\delta^{3/2} + b\dot{\delta} \\ \mu_{bd}\left(K\delta^{3/2} + b\dot{\delta}\right) \\ 0 \end{bmatrix} = f(\delta, \dot{\delta}, s). \tag{14}$$

## 2.5 BEARING FRICTION TORQUES

In rolling element bearings, contact deformation, viscous lubrication, and seal rubbing generate rotational resistive torque

$$T_f = T_{load} + T_{\text{lub}} + T_{seal}, \tag{15}$$

where $T_{load}$ is the torque caused by bearing radial loads and contact deformations. For a ball bearing under radial load, $T_{load}$ has been formulated [75] as

$$T_{load} = 0.0003\left(\frac{F_s}{C_s}\right)^{0.55} F_\beta d_p \tag{16}$$

where $C_s$ is the bearing static load rating defined by the bearing's manufacturer, $F_s$ is the static equivalent load defined as

$$F_s = \begin{cases} 0.6F_r + 0.7F_a & (F_r < F_a) \\ F_r & (F_r > F_a) \end{cases} \tag{17}$$

and $F_\beta$ depends on the magnitude and direction of the applied loads, which equals to $F_r$ in radial ball bearings under pure radial loads.

The lubricant friction torque, $T_{lub}$, is defined by empirical equations [80] as:

$$T_{\text{lub}} = \begin{cases} 10^{-7} f_o\left(\upsilon_o f_r\right)^{2/3} {d_p}^3 & \upsilon_o f_r \geq 2000 \\ 16\times10^{-6} f_o {d_p}^3 & \upsilon_o f_r < 2000 \end{cases} \tag{18}$$

where $f_r$ is the rotational speed in revolution per minute, $\upsilon_o$ is kinematic viscosity of the lubricant in centistokes and coefficient $f_o$, which depends on the bearing type and

lubrication, equals unity for deep-groove ball bearings lubricated with oil mist and is given in [75] for other types of bearings with different lubrications. The rubbing seal friction torque, $T_{seal}$ , which depends on the geometry and design of the seal, is assumed constant.

## 2.6 FAULT MODELING

Bearings fail by numerous fault modes: corrosion, wear, plastic deformation, fatigue, lubrication failure, electrical damage, fracture, and incorrect design, among others. Most common, spalling fatigue leaves pits on races or rollers, as in Figure 8(a), because of periodic contact stress [81]. Most models for rolling element bearing faults have introduced mathematical impulse functions based on fault frequencies. Here, a kinematics-based fault modeling is introduced, where the faults are defined in the model based on the surface profile change.

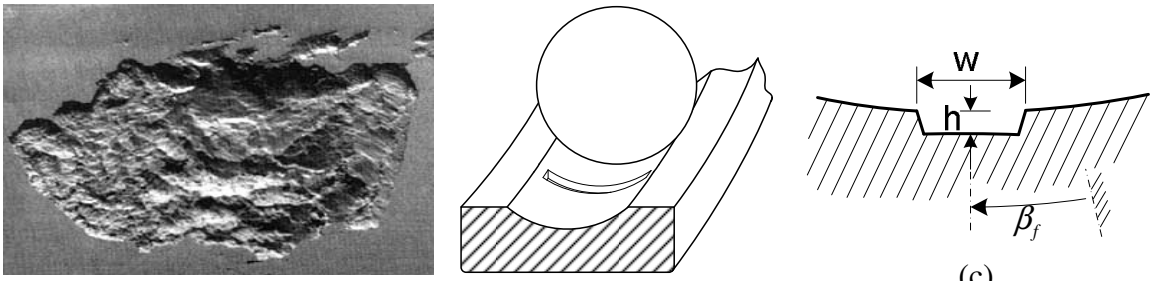


(a) (b) (c)

Figure 8 (a) Subsurface-initiated fatigue spall [81], (b) outer race fault model, (c) cross section of an outer race fault

For each fault, width $w$, depth $h$ , and location of the fault $\beta_f$ in the body coordinate system are defined as shown in Figure 8(c). Parameters $T_f, w, h, r_f$ and $\beta_f$ in the model define type, size, shape and location of localized faults as shown in the block

diagram of Figure 9. $T_f$ defines type of the fault, $w$ and $h$ represent size, $r_f$ determines the shape of the fault, and the location of the fault on each element is determined by $\beta_f$ in the model.

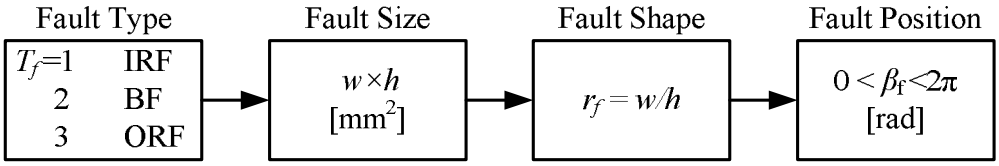


Figure 9 Four parameters $T_f, w, h, r_f$ and $\beta_f$ represent type, size, shape and location of faults in the model

As a fault passes through the contact, the profile changes induce deflections that result in dynamic interactions between elements, which generate force impulses that induce fault vibrations. Multiple faults of different size and shape, at any location of the bearing, can be modeled via the proposed scheme.

## 2.7 BOND GRAPHS

Bond graphs introduced in 1950 by Paynter [2], map energy storage, energy dissipation and power flow between components in a system through energy bonds and elements[82]. Associated with each bond are power conjugates, effort and flow, the product of which is the instantaneous power flowing to or from physical elements. Efforts and flows in mechanical systems are forces and velocities. Energy dissipation is modeled by the resistive element **R**, energy storage devices such as springs and inertia are modeled by elements **C** and **I**, sources of efforts and flows are represented by **Se** and **Sf**, and power transformations are modeled by transformers **TF** or gyrators **GY**. Power bonds join at **0** junctions summing flows to zero with equal efforts or at **1** junctions

summing efforts to zero with equal flows, which implements Newton's 2nd law. With constitutive laws for each element such as Eqs. (5) and (10), state equations are extracted from bond graphs. Bond graphs have many advantages. Multiphysic dynamic systems such as electrical, mechanical, magnetic, fluid, chemical, and thermodynamic systems can be modeled and linked together. Also, FEM models can be embedded in model [32]. Furthermore, the modularity characteristic of bond graphs permits system growth.

### 2.7.1 Multibody Dynamics with Bond Graphs

Dynamics of a 6-DOF rigid body system with the global coordinate XYZ and the body coordinate *xyz* as shown in Figure 10(a) can be represented with Newton-Euler's equations [83]

$$\mathbf{M}\ddot{\mathbf{x}} = \sum_1^n \mathbf{F}_i \tag{19}$$

$$\bar{\mathbf{J}}\ddot{\boldsymbol{\theta}} = \bar{\boldsymbol{\tau}} + \sum_1^n \left(\bar{\mathbf{r}}_i \times \bar{\mathbf{F}}_i\right) - \dot{\boldsymbol{\theta}} \times \bar{\mathbf{J}}\,\dot{\boldsymbol{\theta}}, \tag{20}$$

expressed in the global and the body coordinate systems respectively.

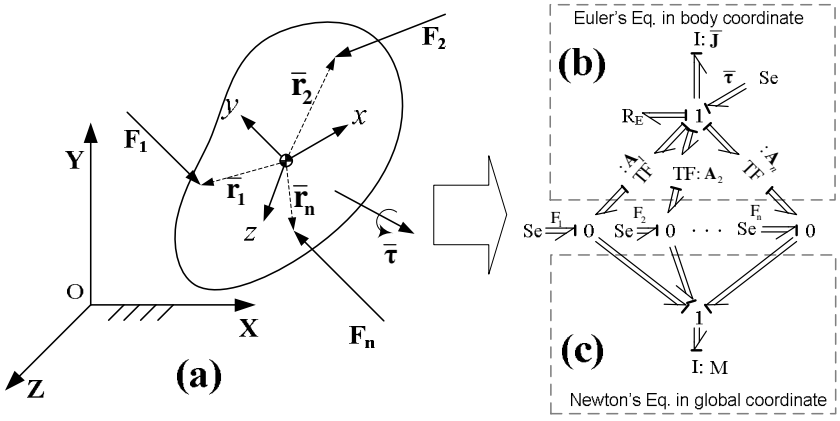


Figure 10 dynamics of a rigid body under external loads is represented with a diamond shape vector bond graph model.

The body is subjected to external forces $\mathbf{F}_i$ and moment $\bar{\boldsymbol{\tau}}$, also expressed in the global and the body coordinates respectively. The second term on the right side of Euler's equation (20) represents moments due to external forces. The last term is the Eulerian junction term representing gyroscopic force.

A cross product $\mathbf{C} \times \mathbf{B}$ can be represented in matrix form using the cross product operator $[\mathbf{A} \times]$ as:

$$\mathbf{C} \times \mathbf{B} = \begin{bmatrix} \mathbf{C}_x \\ \mathbf{C}_y \\ \mathbf{C}_z \end{bmatrix} \times \begin{bmatrix} \mathbf{B}_x \\ \mathbf{B}_y \\ \mathbf{B}_z \end{bmatrix} = \begin{bmatrix} 0 & -\mathbf{C}_z & \mathbf{C}_y \\ \mathbf{C}_z & 0 & -\mathbf{C}_x \\ -\mathbf{C}_y & \mathbf{C}_x & 0 \end{bmatrix} \begin{bmatrix} \mathbf{B}_x \\ \mathbf{B}_y \\ \mathbf{B}_z \end{bmatrix} = [\mathbf{C} \times]\mathbf{B} \tag{21}$$

Applying this to the second term, Euler's equation becomes

$$\bar{\mathbf{J}}\ddot{\bar{\boldsymbol{\theta}}} = \bar{\boldsymbol{\tau}} + \sum_1^n [\bar{\mathbf{r}}_i \times]\bar{\mathbf{F}}_i - \dot{\bar{\boldsymbol{\theta}}} \times \bar{\mathbf{J}}\,\dot{\bar{\boldsymbol{\theta}}} \tag{22}$$

External forces in the global coordinates can be transformed to the body coordinates as

$$\bar{\mathbf{F}}_i = \mathbf{T}_{\mathrm{GB}} \mathbf{F}_i \tag{23}$$

where $\mathbf{T}_{\mathrm{GB}}$ is the transformation matrix obtained from Euler angles or direction cosines [83].

Rewriting the Newton-Euler equations (19) and (22), we have

$$\begin{aligned} \mathbf{M}\ddot{\mathbf{x}} &= \sum_1^n \mathbf{F}_i \\ \bar{\mathbf{J}}\ddot{\bar{\boldsymbol{\theta}}} &= \bar{\boldsymbol{\tau}} + \sum_1^n \mathbf{A}_i \mathbf{F}_i - \dot{\bar{\boldsymbol{\theta}}} \times \bar{\mathbf{J}}\,\dot{\bar{\boldsymbol{\theta}}} \end{aligned} \tag{24}$$

where

$$\mathbf{A}_i = [\bar{\mathbf{r}}_i \times]\mathbf{T}_{\mathrm{GB}}\,. \tag{25}$$

In terms of vector bond graphs, as shown in Figure 10(b,c), Newton's and Euler's equation can be represented as **1** junctions that embed conservation of linear momentum, and conservation of angular momentum. Transformers TF with modulus of $\mathbf{A}_i$ transform coordinates between Euler's and Newton's equations and also convert external forces to moments acting on the center of mass. External moments $\bar{\boldsymbol{\tau}}_i$ are represented by sources of efforts **Se**. The gyroscopic term $\dot{\bar{\boldsymbol{\theta}}} \times \bar{\mathbf{J}}\, \dot{\bar{\boldsymbol{\theta}}}$ is incorporated as a modulated $\mathbf{R}_E$ element. The overall bond graph structure of the system in Figure 10(a) with dynamic Eqns. (24) is the diamond-shaped bond graph structure of Figure 10(b-c). A multibody system consisting of n rigid bodies can be modeled by connecting $n$ diamond-shape bond graph structures together through constraints models.

## 2.8 BOND GRAPH MODEL OF ROLLING ELEMENT BEARINGS

A deep-groove ball bearing consisting of nine balls, inner race, and outer race is modeled as a multibody system using vector bond graphs. The outer race is fixed in a housing characterized by stiffness and damping in the vertical and horizontal directions. The inner race moves and rotates under external forces and torques, (Figure 11a). Weights are applied as external loads on each body. Each element is modeled using the diamond-shaped vector bond graph structure of Figure 10. Contacts are modeled as nonlinear **C** elements representing nonlinear stiffness, damping, and traction forces inherent in Eq. (14).

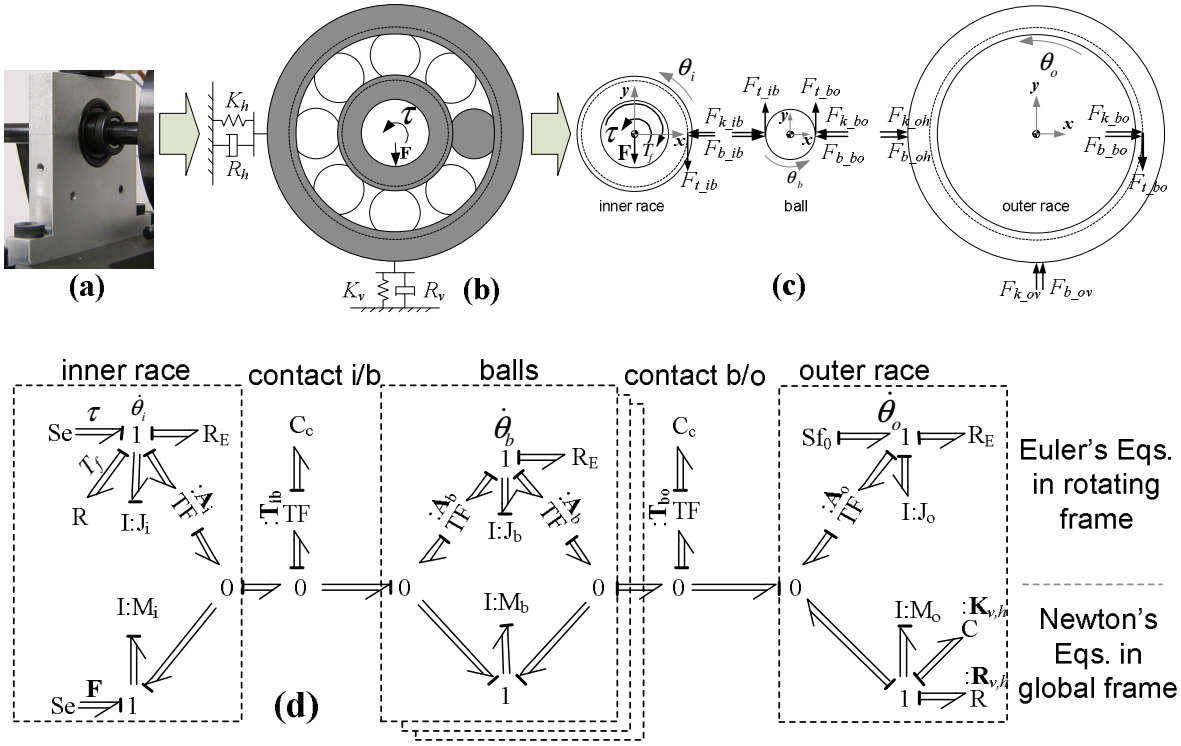


Figure 11 Rolling element bearing with single roller. a) bearing with housing, b) system with external loads and constraints, c) free body diagram, d) bond graph models of each element and contacts

The bond graph model of a bearing with races and one ball, in Figure 11(d), has three of the diamond-shape bond graph structures with two contact models in between. Each diamond structure applies Newton-Euler's Eqs. (24) to inner race, balls, and outer race via the **1** junction. Each has rotational inertia **J** , translational inertia **M**, transformer **TF** with modulus matrix **A** transforming body coordinate system to the global coordinate system (Eqs. 23-25), and Eulerian junction elements $\mathbf{R}_E$ representing gyroscopic moments. External torque $\boldsymbol{\tau}$ and external force vector **F** are applied to the **1** junctions through **Se** elements. Bearing rotational friction torques are modeled as resistive elements **R** in the inner race model, with the constitutive law described by Eqs. (15-18). Housing stiffness and damping effects are modeled through **C** and **R** elements with

structural stiffness and damping matrices $\mathbf{K}_{v,h}$ and $\mathbf{R}_{v,h}$. Each contact model consists of a transformer and a $\mathbf{C}_c$ element. Transformers **TF** transform the contact coordinate systems to the global coordinate system, as expressed in Eq. (2). Nonlinear elements $\mathbf{C}_c$ with the constitutive law of Eq. (14) represent contact and traction forces. Here, the bond graph model of the bearing with 9 balls and 2 races, consists of 11 diamond shape models combined through 18 contact models as shown in Figure 12. Each ball has the dynamics structure shown in Figure 11(d). The bonds that converge onto the inner and outer races signify the forces transmitted between ball and races. Faults are modeled by surface profile changes as shown in Figure 8(c). During simulations, the geometry of elements changes based on locations and growth of faults. Fault impulses and forces are generated via the kinematics and dynamics of balls interacting with surface profile changes.

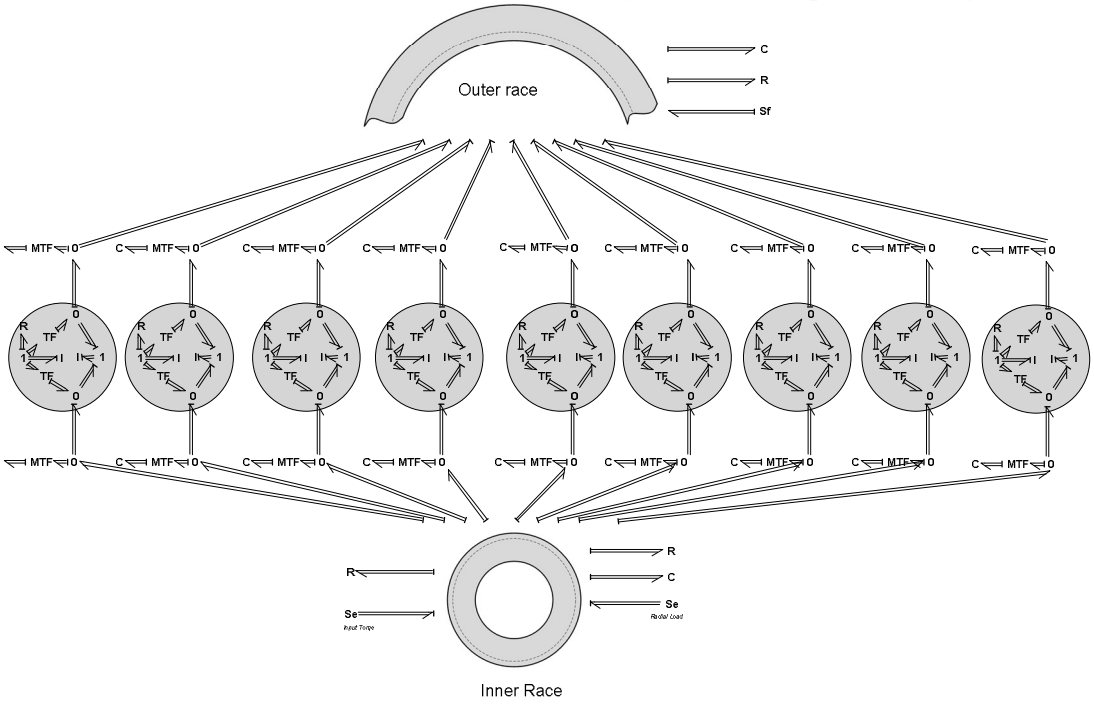


Figure 12 Unified vector bond graph model of a rolling element bearing with 9 balls and 2 rings.

## 2.9 STATE EQUATIONS

State equations, extracted from the bond graph of Figure 12 with state vectors $\dot{\mathbf{h}}_i$, $\dot{\mathbf{P}}_i$, $\dot{\mathbf{q}}_{ib}^k$, $\dot{\mathbf{h}}_b^k$, $\dot{\mathbf{P}}_b^k$, $\dot{\mathbf{q}}_{bo}^k$, $\dot{\mathbf{P}}_o$ and $\dot{\mathbf{q}}_o$ are

$$\dot{\mathbf{h}}_i = \boldsymbol{\tau} - \left[\mathbf{R}\mathbf{J}_i^{-1}\mathbf{h}_i\right] - \left[\mathbf{R}_E\mathbf{J}_i^{-1}\mathbf{h}_i\right] - \mathbf{A}_i^k\mathbf{T}_{ib}^k\left[\mathbf{C}_c^k\mathbf{q}_{ib}^k\right] \tag{26}$$

$$\dot{\mathbf{p}}_i = \mathbf{F} + \mathbf{T}_{ib}^k\left[\mathbf{C}_c^k\mathbf{q}_{ib}^k\right] \tag{27}$$

$$\dot{\mathbf{q}}_{ib}^k = \mathbf{T}_{ib}^k\left(-\mathbf{M}_i^{-1}\mathbf{p}_i + \mathbf{A}_i^k\mathbf{J}_i^{-1}\mathbf{h}_i - \mathbf{M}_b^{-1}\mathbf{p}_b^k + \mathbf{A}_b^k\mathbf{J}_b^{k^{-1}}\mathbf{h}_b^k\right) \tag{28}$$

$$\dot{\mathbf{h}}_b^k = -\left[\mathbf{R}_E^k\mathbf{J}_b^{-1}\mathbf{h}_b\right] - \mathbf{A}_b^k\mathbf{T}_{bo}^k\left[\mathbf{C}_c^k\mathbf{q}_{bo}^k\right] - \mathbf{A}_b^k\mathbf{T}_{ib}^k\left[\mathbf{C}_c^k\mathbf{q}_{ib}^k\right] \tag{29}$$

$$\dot{\mathbf{p}}_b^k = \mathbf{T}_{ib}^k\left[\mathbf{C}_c^k\mathbf{q}_{ib}^k\right] - \mathbf{T}_{bo}^k\left[\mathbf{C}_c^k\mathbf{q}_{bo}^k\right] \tag{30}$$

$$\dot{\mathbf{q}}_{bo}^k = \mathbf{T}_{bo}^k\left(\mathbf{A}_b^k\mathbf{J}_b^{k^{-1}}\mathbf{h}_b - \mathbf{M}_b^{-1}\mathbf{p}_b^k + \mathbf{M}_o^{-1}\mathbf{p}_o\right) \tag{31}$$

$$\dot{\mathbf{p}}_o = -\mathbf{K}_{v,h}\mathbf{q}_o - \mathbf{R}_{v,h}\mathbf{M}_o^{-1}\mathbf{p}_o - \mathbf{T}_{bo}^k\left[\mathbf{C}_c^k\mathbf{q}_{bo}^k\right] \tag{32}$$

$$\dot{\mathbf{q}}_o = \mathbf{M}_o^{-1}\mathbf{p}_o \tag{33}$$

Superscript $k$ has range $1 \le k \le N$, where $N$ is the number of balls. Subscripts $i$, $b$, and $o$ denote inner race, ball and outer race respectively, $\mathbf{h}_i$ and $\mathbf{h}_b$ are angular momentums of inner race and balls, $\mathbf{p}_i$, $\mathbf{p}_b$ and $\mathbf{p}_o$ are linear momentum of inner race, balls and outer race respectively, and $\mathbf{q}_{ib}$ and $\mathbf{q}_{bo}$ are contact displacements. For a rolling element bearing with $N = 9$ balls ( $k = 1, 2, ..., 9$ ),equations (26) - (33) comprise 40 equations.

Nonlinear terms in brackets $\left[\mathbf{R}\mathbf{J}_i^{-1}\mathbf{h}_i\right]$, $\left[\mathbf{R}_E\mathbf{J}^{-1}\mathbf{h}\right]$ and $\left[\mathbf{C}_c^k\mathbf{q}^k\right]$ represent constitutive laws for elements $\mathbf{R}$, $\mathbf{R}_E$ and $\mathbf{C}_c$ associated with bearing rotational torque, gyroscopic force and contact forces. Related constitutive laws are

$$\left[\mathbf{R}\mathbf{J}_i^{-1}\mathbf{h}_i\right]=\begin{bmatrix}0\\0\\T_f\end{bmatrix}=\begin{bmatrix}0\\0\\T_{load}+T_{\text{lub}}+T_{seal}\end{bmatrix} \tag{34}$$

$$\begin{aligned}\left[\mathbf{R}_E\mathbf{J}^{-1}\mathbf{h}\right]&=\dot{\boldsymbol{\theta}}\times\mathbf{J}\,\dot{\boldsymbol{\theta}}\\&=\mathbf{J}^{-1}\mathbf{h}\times\mathbf{J}\;\mathbf{J}^{-1}\mathbf{h}=\mathbf{J}^{-1}\mathbf{h}\times\mathbf{h}\end{aligned} \tag{35}$$

$$\left[\mathbf{C}_c^k\mathbf{q}^k\right]=\begin{bmatrix}K\delta^{3/2}+b\dot{\delta}\\ \mu_{bd}\left(K\delta^{3/2}+b\dot{\delta}\right)\\0\end{bmatrix}=f(\mathbf{q},\dot{\mathbf{q}})\qquad;\qquad\mathbf{q}=\begin{bmatrix}\delta\\0\\0\end{bmatrix} \tag{36}$$

where $K$, $b$ and $\mu_{bd}$ are defined by Eqs. (6), (9) and (13) respectively. In the state equations above, coordinate transformation matrices $\mathbf{A}^k$ and $\mathbf{T}^k$ are transformer moduli associated with body and contact coordinates given as

$$\begin{aligned}\mathbf{A}^k&=[\bar{\mathbf{r}}\times]\mathbf{T}_{\text{GB}}\\&=\begin{bmatrix}0&0&-R\sin(\alpha-\theta)\\0&0&R\cos(\alpha-\theta)\\R\sin(\alpha-\theta)&-R\cos(\alpha-\theta)&0\end{bmatrix}\begin{bmatrix}\cos\theta&\sin\theta&0\\-\sin\theta&\cos\theta&0\\0&0&1\end{bmatrix}\end{aligned} \tag{37}$$

$$\mathbf{T}^k=\begin{bmatrix}\cos\alpha&\sin\alpha&0\\-\sin\alpha&\cos\alpha&0\\0&0&1\end{bmatrix}. \tag{38}$$

Here, $R$ is the radius of the element, $\theta$ is the body orientation, and $\alpha$ is the contact coordinates orientation defined in Eq. (1). Matrices $\mathbf{K}_{v,h}$ and $\mathbf{R}_{v,h}$ in state equations define structural stiffness and damping of the bearing housing along vertical and horizontal directions.

## 2.10 SUMMARY AND CONCLUSIONS

A detailed model of rolling element bearings developed in vector bond graphs, incorporated multibody dynamics of elements, centrifugal effects, dynamics of contacts,

and surface defects. Newton-Euler's equations for each element were encoded into bond graphs, with dynamics of contacts, traction forces, and rotational frictions formulated as constitutive laws of elements. A kinematic-based fault model was introduced. Tribological faults were modeled as surface profile changes, which generate impulses via dynamic interactions of faults and bearing elements. Fault parameters define type, size, shape, and locations of faults. The modular and generic rolling element bearing bond graph model represent complex dynamics of both normal and defective bearings, for rolling element bearings with different geometry and specifications.

# Chapter 3

# Model Verification and Fault Analysis of Rolling Element Bearings

## 3.1 INTRODUCTION

A detailed physics-based model of rolling element bearing is a valuable tool for bearing design, fault analysis and condition monitoring. The model can be used to study dynamic and kinematic behavior of rolling element bearings in presence of faults. In this chapter, a bond graph model of a rolling element bearing with localized fault is constructed and simulated. Experiments on bearing with IRF, ORF and BF were conducted to validate the model. Dynamic aspects of bearing such as centrifugal effects were studied and simulations are compared with the available models to validate the model. Then, effects of geometry of faults, bearing clearance, and radial loads on vibration responses are investigated. Also, dynamics of contacts with presence of localized faults is studied in detail using the model.

## 3.2 SIMULATION AND EXPERIMENT SETUP

Bond graph model of a deep groove ball bearing with specifications in Table 1 was built and numerically simulated with software 20-sim 4.0. The Runge-Kutta Dormand Prince integration method with variable step size was used in simulations. Initial velocities and accelerations were zero. A radial load was applied to the inner race vertically downward. Running torque and external rotational loads were applied to the inner race.

Table 1 Bearing specifications and simulations parameters

| Parameter | Value |
|---|---|
| Bearing model No. | MB ER-16K |
| Number of balls | 9 |
| Material Density [g/cm3] | 7.75 |
| Elastic modulus [MPa] | 210 |
| Ball/inner race/outer race dia. [mm] | 7.94 / 31.38 / 47.26 |
| Pitch diameter [mm] | 39.32 |
| Race groove radius [mm] | 4.1 |
| Poisson's ratio | 0.25 |
| Radial load on inner race [N] | 110 |
| Inner race rotational speed [Hz] | 35 |
| Housing vertical/horizontal stiffness [N/mm] | 4×107 |

Effects of the clearance and radial loads on the load zone distribution were studied. Three cases of clearance and two cases of radial loads were simulated. Healthy and faulty bearings with localized faults on inner race, outer race, and balls were simulated. For each type of fault, 16 cases with different fault size (Table 2) were simulated to study effects of fault type, size and shape on the vibration response. For each case, the vertical vibration signal of the housing will be presented. Also, normal contact force and displacements in the presence of ball faults are presented.

Table 2 Studied Faults: surface profile changes defined by width w and h

| 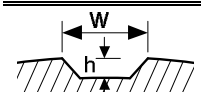 | faults size: w × h [$mm^2$] | | | |
|---|---|---|---|---|
| | $w = 5h$ | $w = 2h$ | $w = h$ | $w = 0.5h$ |
| Fault Level I | 2.25×0.45 | 1.00×0.50 | 0.71×0.71 | 0.22×0.44 |
| Fault Level II | 3.15×0.63 | 1.42×0.71 | 1.00×1.00 | 0.32×0.64 |
| Fault Level III | 6.30×1.26 | 2.82×1.41 | 1.41×1.41 | 0.45×0.90 |

For a bearing with stationary outer race and rotating inner race under downward vertical load **F**, the loading zone is stationary. In the load zone, reaction forces transfer load **F** between housings and shaft. Based on the angular position of the Outer Race Fault (ORF), the vibration response can change. However, in the case of Inner Race Fault (IRF) and Ball Fault (BF), fault locations do not affect the response since faults are not stationary with respect to the load zone. Here, the model is simulated with ORF located down at the load zone

Experiments were conducted on the test rig shown in Figure 13 with three types of rolling element bearing faults IRF, BF, and ORF. The test rig consists of a rotating shaft supported by two rolling element bearings (Table 1). A 3-phase induction motor rotates the shaft through a beam coupling. Bearing loaders apply static radial loads to bearings, and a magnetic loader applies rotational loads to the shaft through a gearbox and belts. Accelerometers measure vertical and horizontal vibrations of the outboard bearing housing. Eddy current proximity probes measure vertical and horizontal displacements of the shaft close to the bearing. A tachometer and an encoder measure shaft speed. Also, voltages and currents of the induction motor can be measured. Localized faults were created on inner race, outer race and balls by spot grindings. A vertical load was applied to the inner race via the bearing loader. Since excessive vibrations can invalidate results, waterfall plots and hammer tests found machine critical speeds and natural frequencies, which were avoided during tests. At the shaft speed of 35 Hz, bearing vibration signals and rotor speed were recorded at sampling rate of 76800 Hz and computer analyzed.

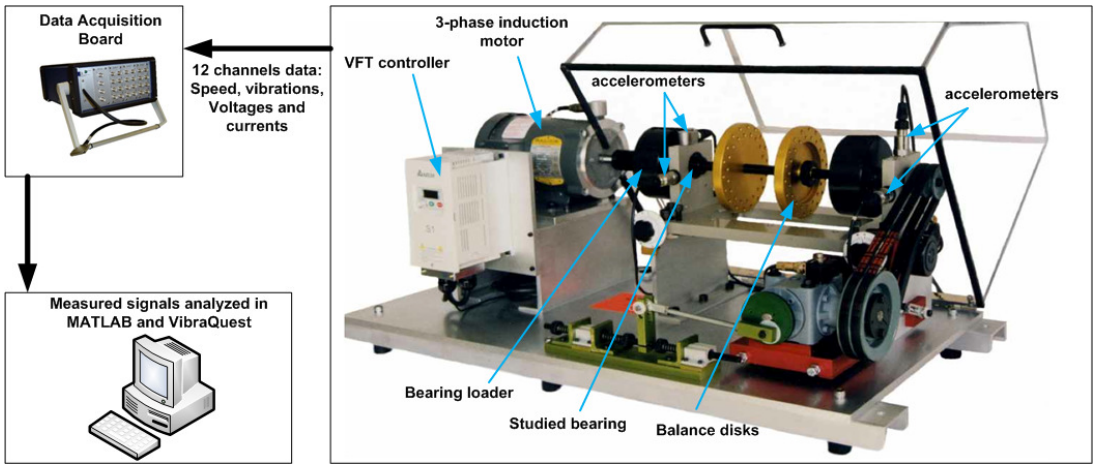


Figure 13 Experiment setup for bearing Experiments.

## 3.3 BEARING MODEL VERIFICATION

### 3.3.1 Load Zone Tests

Clearance in bearings changes the profile of contact tractions in the load zone. Defects within the load zone generate much bigger impulses than at other locations in a bearing. This behavior is observed as modulations of the vibration responses for Inner Race Fault (IRF) and Bearing Fault (BF), wherein faults are not stationary. Outer race faults, when located in the load zone, create a much larger response than at other locations. Vibration responses in faulty bearings can change significantly with clearance of the bearing. The model should be detailed enough to include this behavior. Figure 14 shows simulation results for a rolling element bearing with 0.08 mm clearance, 0 clearance, and 0.02 mm preloads. For each case, the load zone profile for radial load conditions of 100N and 60N were calculated.

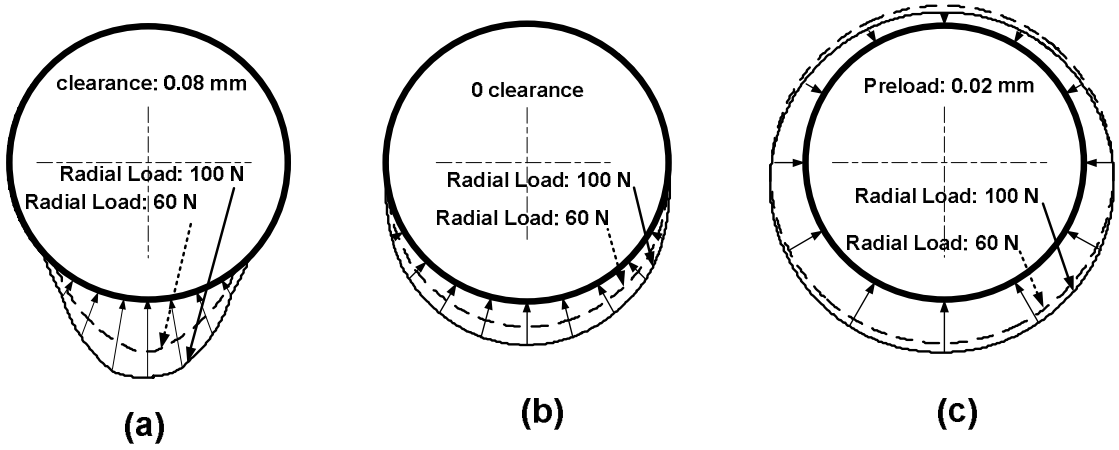


Figure 14 Simulation results: effects of clearance and radial loads on load distribution in rolling element bearings. (a): 0.08 mm clearance, (b): 0 clearance, (c): 0.02 mm preload.

For a given clearance, the load zone widens and lengthens with increased radial load. For zero clearance, the load zone covers half the ring regardless of the radial load, and expands with load. In case of preloads usually demanded by the design of the bearing, the load zone extends completely around the ring with zero radial loads, and shifts to one side when radial load is applied. The simulated results of the load zone show the ability of the detailed model to incorporate load zone effects in vibration results.

### 3.3.2 Fundamental Fault Frequencies

To validate the model, experiments were conducted and vibration signals of the bearing in the vertical direction, in time- and frequency-domains, were measured and compared with simulations. Results are presented in Figure 15 for Inner Race Faults (IRF), in Figure 16 for Ball Faults (BF), and in Figure 17 for Outer Race Faults (ORF). For each fault, upper plots are simulations and bottom plots are experimental results. Plots to the left present vibration waveforms with the magnified portions in middle plots.

The right plots are power spectra of these vibration signals. To isolate fault signals, bearing fundamental frequencies, which depend on the bearing geometry and rotor speed [28], are

Inner Race Fault Frequency: $$f_{IRF} = \frac{n}{2} f_r \left(1 + \frac{d_b}{d_p} \cos \phi\right) \quad (1)$$

Outer Race Fault Frequency: $$f_{ORF} = \frac{n}{2} f_r \left(1 - \frac{d_b}{d_p} \cos \phi\right) \quad (2)$$

Ball Fault Frequency: $$f_{BF} = \frac{d_p}{d_b} f_r \left(1 - \frac{{d_b}^2}{{d_p}^2} \cos^2 \phi\right) \quad (3)$$

Case Frequency: $$f_{cage} = \frac{f_r}{2} \left(1 - \frac{d_b}{d_p} \cos \phi\right) \quad (4)$$

Here $n$ is the number of balls, $f_r$ is the rotor frequency, $d_b$ is the balls diameter, $d_p$ is the bearing pitch diameter, and $\phi$ is the contact angle which is zero for radial bearings. Given $f_r = 35$ Hz, for the bearing of Table 1, the bearing frequencies are $f_{IRF} = 189.28$ Hz , $f_{ORF} = 125.72$ Hz , $f_{BF} = 166.32$ Hz , $f_{cage} = 13.96$ Hz .

Figure 15(a) contains simulated vibration signals of acceleration vs. time for IRF. Here, fault impact signals are modulated with rotor frequency $f_r$, because the inner race fault, fixed on the inner race, passes through the load zone at a rate of $f_r$ as the inner race rotates . Similar behavior with the same frequency is observed in the corresponding experimental signals shown in Figure 15(d). The magnified portion of vibration signal plotted in Figure 15(b) shows fundamental fault frequencies of the bearing, which is confirmed by the experiments in Figure 15(e). As the IRF passes through the contact, two

impact responses appear in the vibration signal. The leading and trailing edges of a surface profile dent would cause impacts with the balls in the load zone. The distance between these two impact signals contains information on the size faults. Figure 15(c,f) present power spectrum of the vibration signals. Depending on the frequency range, harmonics of the fault frequencies (indicated by dashed lines) might appear in the power spectrum.

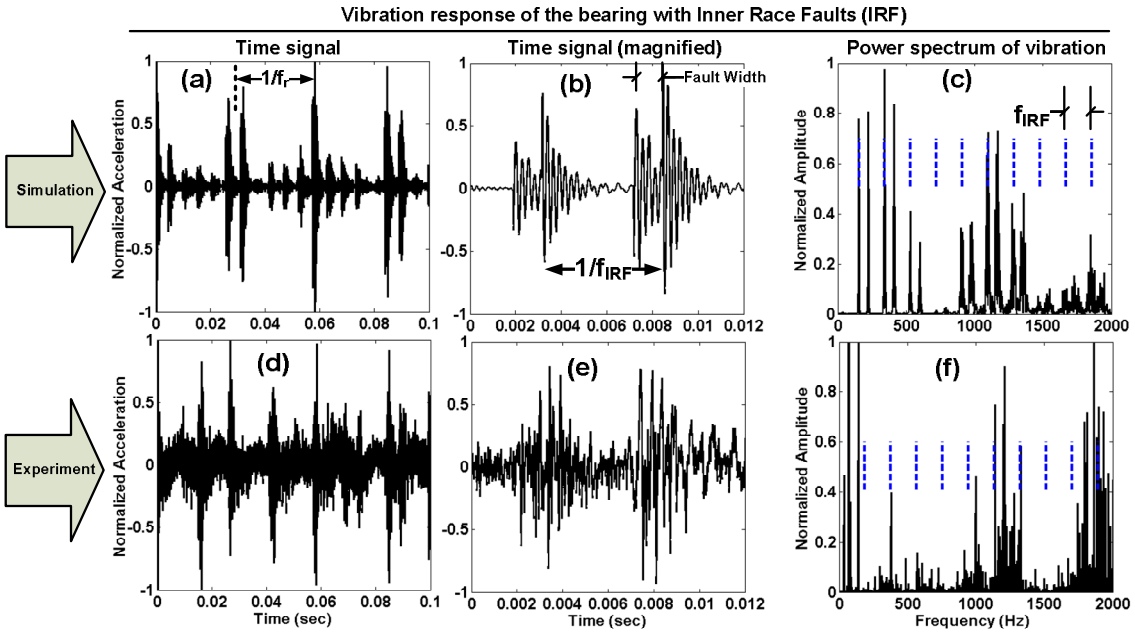


Figure 15 Simulation vs. experiment: Vertical vibration response of the bearing with inner race fault (fault size: w×h = 3×1 [$mm^2$]). Fault is located at the load zone (down). a,d) time response b,e) time response (magnified) and c,f) vibration power spectrum. (shaft speed: 35 Hz)

Figure 16 shows vibration signals of a bearing with a single Ball Fault (BF). Fault impact signals spaced by the fault frequency timing ($1/f_{BF}$) are clearly observed in both simulation and experimental data. Also, simulated signals are modulated by the cage frequency $f_{cage}$. However, in real bearings, three dimensional rotations of balls can

prevent engaging of ball faults with races, causing randomness in measured signals. This phenomenon generates random modulations of vibration signals (see Figure 16d), which can be used to separate ball faults from other types of bearing faults. Another vibration signal feature that agrees with experiments is shape of the impact signals, as shown in Figure 16(b,e). As shown in the magnified plots, vibration signals due to BF consist of a single impact response signal for each fault, compared with the IRF and ORF which generate two impacts. The power spectrum of simulated signals (Figure 16c) reveals harmonics of the fault frequency, which are not very clear in measured signals because of three dimensional motions of balls.

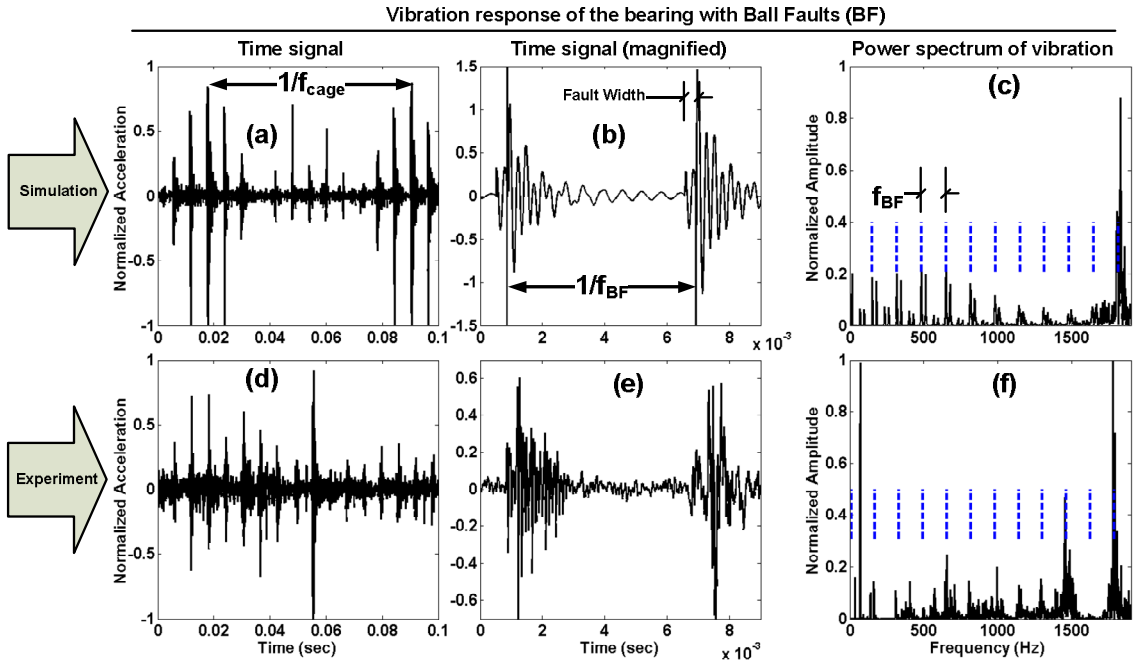


Figure 16 Simulation vs. experiment: vibration response of bearing with ball faults (fault size: w×h = 1.0×0.8 [mm$^2$]). a,d) time response b,e)time response (magnified) and c,f) vibration power spectrum. (shaft speed: 35 Hz)

Simulated vibration signals of the bearing with ORF are compared with experimental results in Figure 17. Simulated vibration signals shown in Figure 17(a) reveal a regular pattern of fault impacts spaced at the fault frequency timing, which appears in the experimental data of Figure 17(d). Two impact signals generated in ORF by the two edges of fault are observed in simulations. Similar to the IRF case, the ORF impact signals contain information on the fault size, which indicate the fault severity. In ORF, since the fault is stationary (not moving), the vibration signal has a regular pattern, and fault frequency harmonics can be clearly observed in the power spectrum.

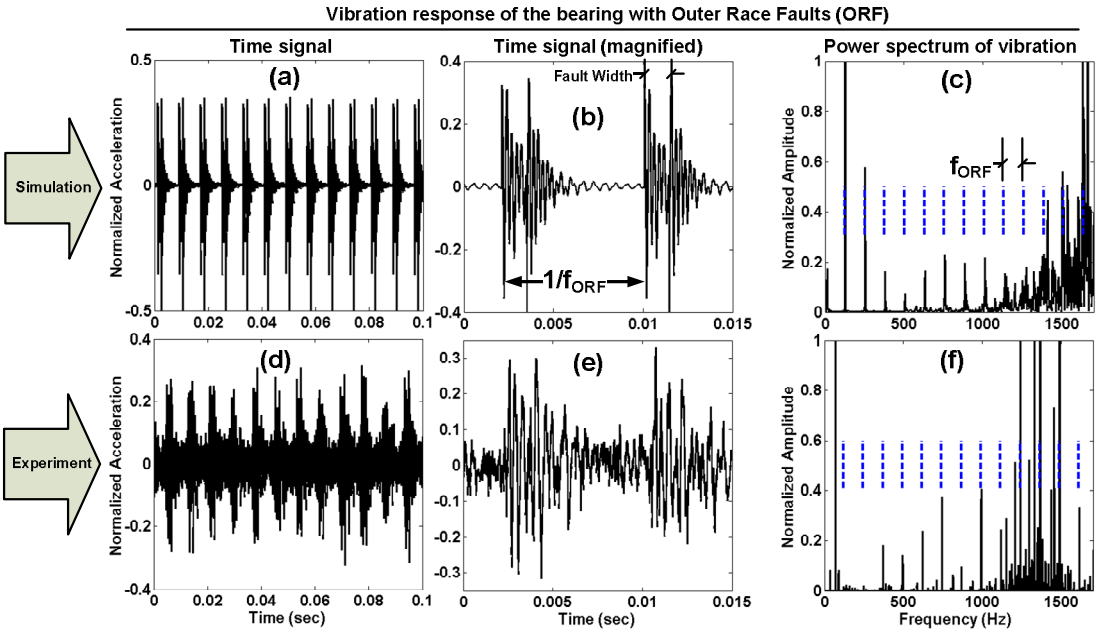


Figure 17 Simulation vs. experiment: vibration response of bearing with outer race faults (fault size: w×h = 2.7×1.0 [mm$^2$] ). a,d) time response b,e) time response (magnified) c,f) vibration power spectrum (shaft speed: 35 Hz).

Comparing simulation signals and measured signals in Figure 15-Figure 17, the natural frequencies of the model and the machine seem to be slightly different. To investigate this issue, startup/coast down tests and hammer tests were conducted to find

critical speeds and natural frequencies of the machine. For the startup/coast down test, the motor speed was controlled by a variable frequency drive (VFD) controller to ramp up from zero to 85 Hz and back down to zero in 80 seconds. Bearing vibration signals in vertical direction were recorded with sampling frequency of 76800Hz. Results are shown in the water plot in Figure 18. The waterfall plot is a 3D graph that shows frequency content of measured vibration signals at each time, or for each shaft speed. Figure 18 suggests that the first and second critical speeds are about 70 and 85 Hz. The Vee shaped curve shows the effects of ramping speed up and down.

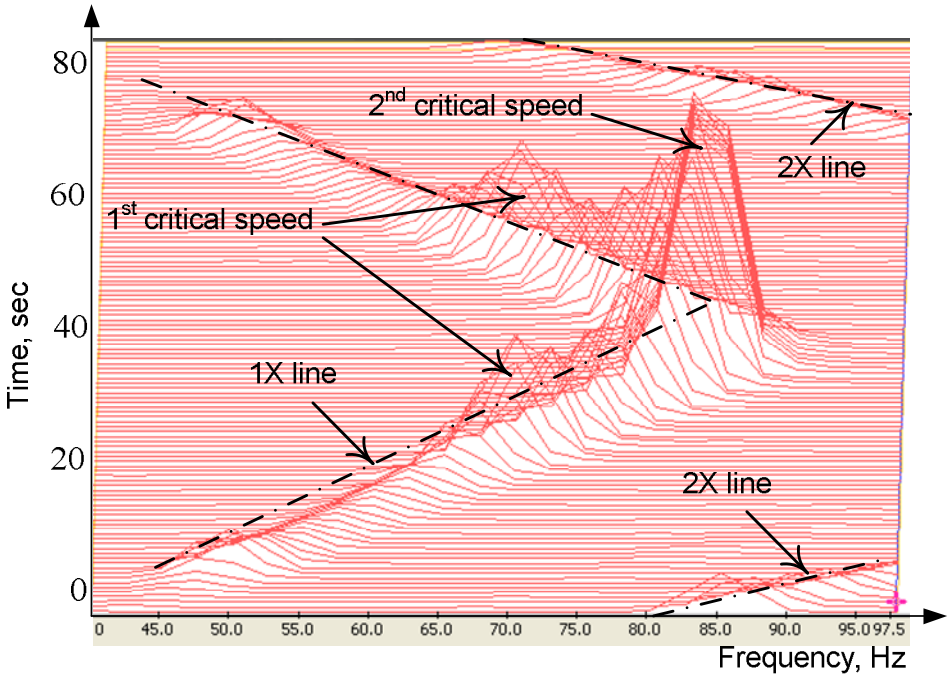


Figure 18 Waterfall plot of bearing vibrations shows the 1st and 2nd critical speeds of the machine.

For hammer tests, the machine base was struck by hammer at different locations of the machine, and the vibration response of the bearing housing was recorded.

Frequency spectra of vibration responses suggest the natural frequencies of the machine at the bearing housing location. Results including time waveform vibration response and related frequency spectra are presented in Figure 19 and Figure 20. Principal natural frequencies from hammer tests were about 480 and 2100 Hz. The most dominant natural frequencies observed in measurement signals during bearing experiments are about 2100 Hz, very close to the main natural frequency of the machine.

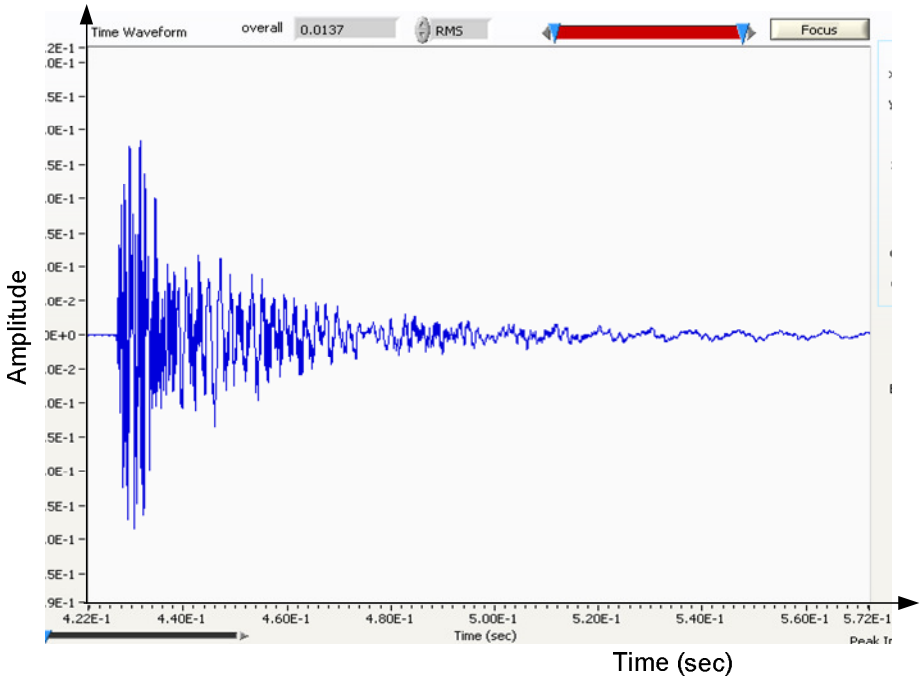


Figure 19 vibration waveform response of the machine in hammer test

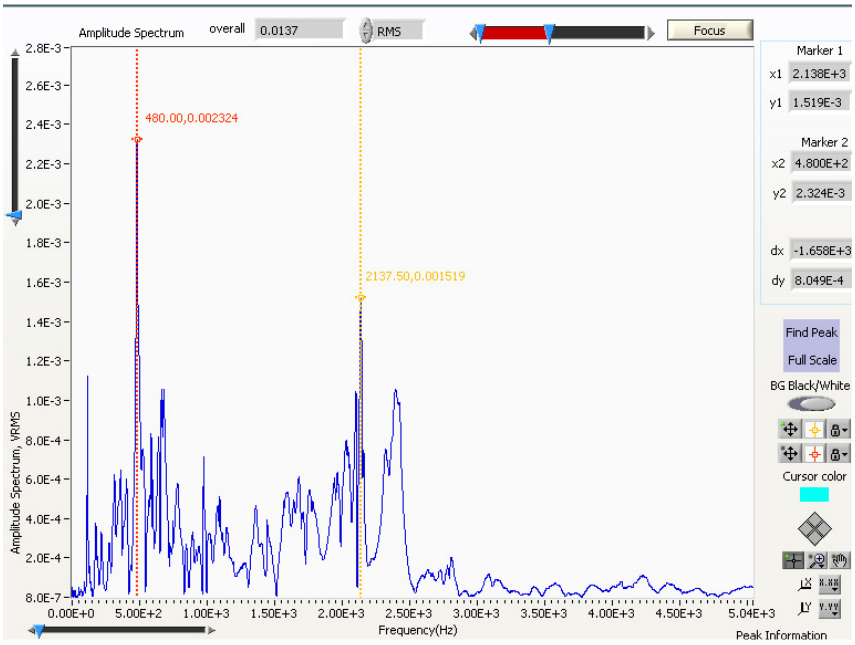


Figure 20 vibration spectrum of the hammer test signals showing the main natural frequencies of the machine about 480 and 2100 Hz.

The structure of the machine, including rotor and other components, are not included in the model. Therefore, natural frequencies of the real machine appear in measured signals but not in simulations. Unmodeled frequencies from the machine frame, bearing housing, rotating shaft, couplings, etc., can be easily appended to the bond graph model.

Simulations suggest that information on type and size of faults exist in the vibration signals from the bearing. However, the real system has numerous natural frequencies not in the bearing model that might mask the original spikes from faults. Tools such as high frequency filters might remove masking signals and retrieve fault information in the real system. Also, factors such as imbalance and misalignments can alter the regular patterns of the faults in a real machine. Interpreting the pattern of damage in real faults needs more than one snapshot of the signal and some statistical

analysis to determine the confidence level of the results. This need is more critical in the case of ball faults and inner race faults, in which faults are moving.

### 3.3.3 Centrifugal Effects in Bearings

The model includes centrifugal forces on balls. To illustrate, a roller bearing with zero clearance under radial load was simulated for different shaft speeds. Bearing radial deflections almost overlay data of Harris [84] in Figure 21. The quadratic relation between radial deflections and shaft speed in Figure 21 represents the centrifugal effects in the bearing. The centrifugal force increases quadratically with the orbital speed of balls, which increases the contact force and bearing radial deflections. Centrifugal effects mainly appear at high speeds, and are not significant at low speeds.

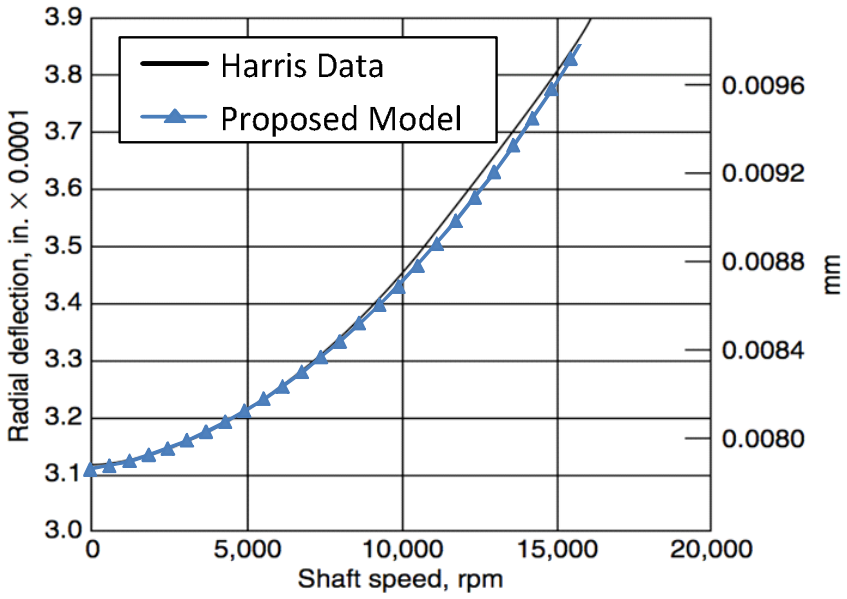


Figure 21 Radial deflection vs. speed for a roller bearing. The centrifugal force on rollers increases contact loads and radial deflections when shaft speed increases. Simulations are compared with the results of Harris [84].

### 3.4 FAULT SEVERITY TEST

A model-based diagnostic employs a model to detect and assess faults, by estimating parameters in the model associated with faults. Therefore, a parametric study is needed. Here effects of type (IRF, BF, ORF), size ($w \times h$) and shape of the fault on vibration responses are studied. Referring to Table 2, faults in three levels corresponding to different sizes of $w \times h$ are simulated and shown in Figure 22, Figure 23, and Figure 24 for IRF, BF and ORF respectively. In time waveform and frequency signals, fundamental fault frequencies ($f_{IRF}, F_{BF}, F_{ORF}$) for all types of faults, cage frequency $f_{cage}$ for BF, and rotor frequency $f_r$ for IRF are observed. More severe faults with bigger defect sizes generate impacts with higher amplitudes, for all types of faults. In IRF and ORF cases, vibration signals have a fault-element impact waveform characterized by two distinct peaks, with distance between these peaks proportional to the fault width, as shown in Figure 22(b,e,h) and Figure 24(b,e,h). However, in the case of BF as shown in Figure 23, the fault size only affects impact amplitudes rather than the distance between two impact peaks.

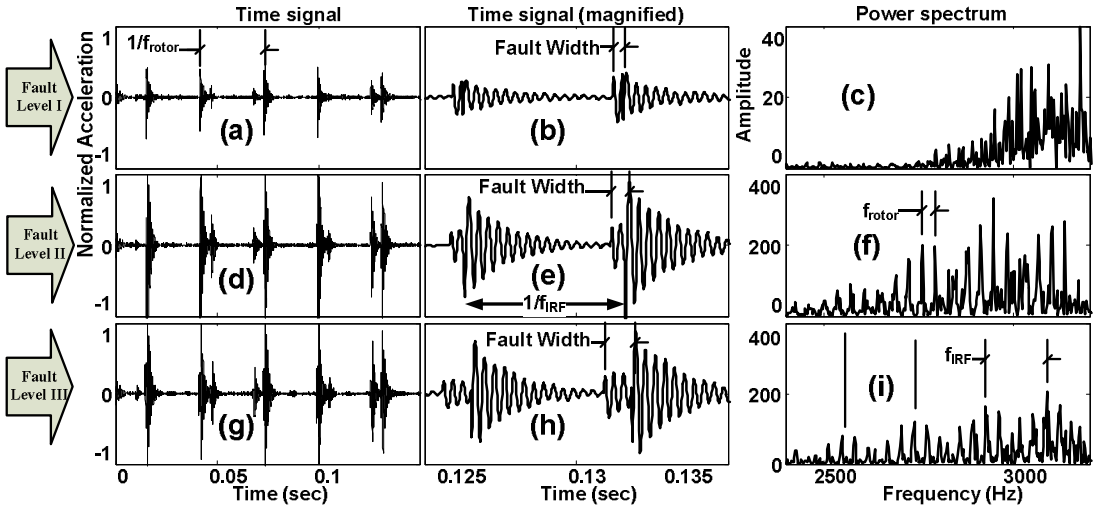


Figure 22 Vibration response of a bearing with Inner Race Fault (IRF) for different fault severities: $w \times h = 1 \times 0.5$ (level I), $1.42 \times 0.71$ (level II), $2.82 \times 1.41$ (level I) [$\text{mm}^2$] and $f_r = 35\text{Hz}$.

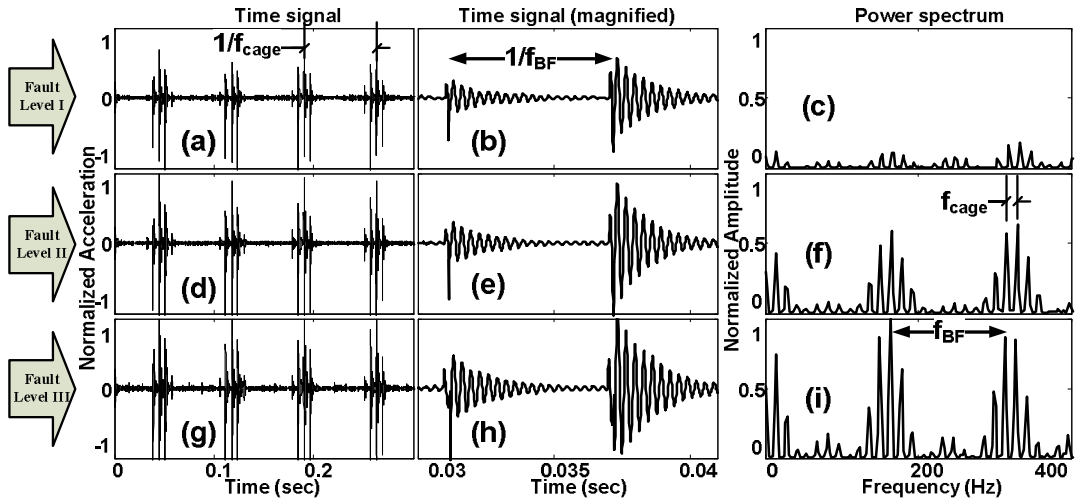


Figure 23 Vibration response of a bearing with Ball Faults (BF) for different fault severities: $w \times h = 1 \times 0.5$ (level I), $1.42 \times 0.71$ (level II), $2.82 \times 1.41$ (level I) $[mm^2]$ and $f_r = 35$Hz.

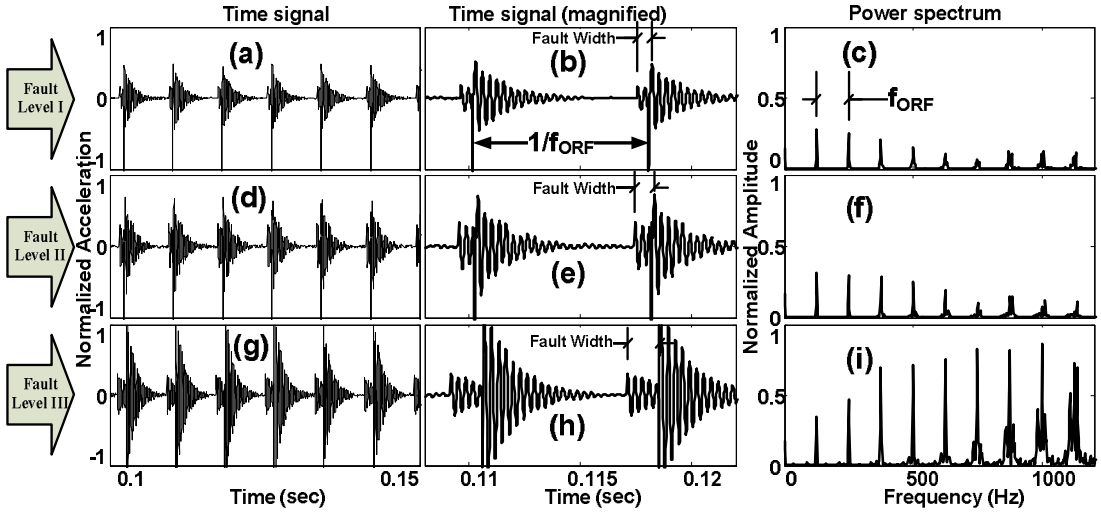


Figure 24 Vibration response of a bearing with Outer Race Fault (ORF) for different fault severities: $w \times h = 1 \times 0.5$ (level I), $1.42 \times 0.71$ (level II), $2.82 \times 1.41$ (level I) $[mm^2]$ and $f_r = 35$Hz.

To investigate the effect of fault shapes on the vibration response, faults with different size ratios ($w/h = 5, 2, 1$) were simulated and results are shown in Figure 25. For IRF and ORF, increasing the fault size ratio $w/h$ enlarges the distance between the two impact peaks, but does not change the impact amplitude much. For BF, the vibration response is relatively insensitive to $w/h$.

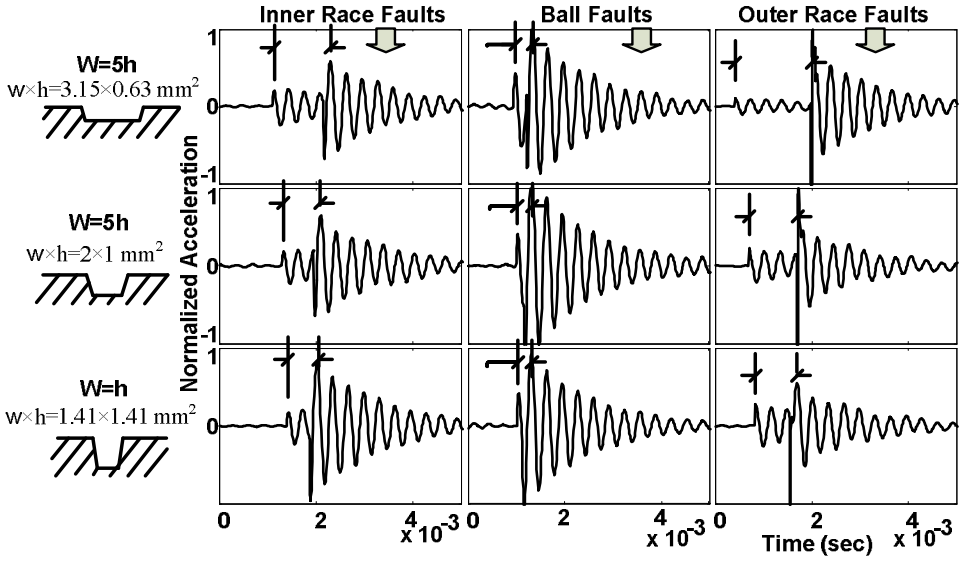


Figure 25 Vibration responses of faulty bearings (IRF, BF, ORF) with different fault shape. $f_r = 35$Hz

## 3.5 DYNAMICS OF ROLLING CONTACTS UNDER SURFACE FAULTS

Simulation results for single surface faults engages with bearing and dynamics of contacts presented in Figure 26, Figure 27, and Figure 28 for IRF, BF, and ORF respectively. Each case present contact forces and displacements for (a): inner race/ball contacts and (b): ball/outer race contacts. Also, vibration signals of the bearing housing are shown in subfigures (c). In subfigures (a) and (b) positive and negative values of forces pertain to tension and compression respectively, and positive and negative values of contact displacements pertain to separation and compression of surfaces respectively.

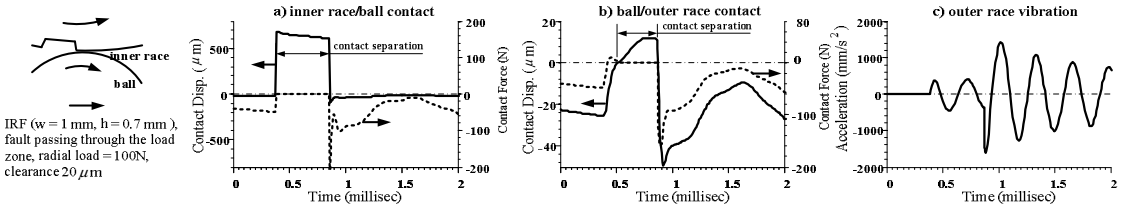


Figure 26 Nonlinear dynamics of rolling contacts with IRF, a) inner race/ball contact, b) ball/outer race contact, c) bearing vibrations

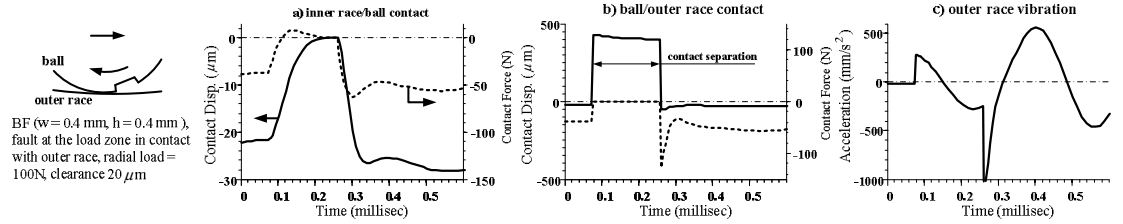


Figure 27 Nonlinear dynamics of rolling contacts with BF, a) inner race/ball contact, b) ball/outer race contact, c) bearing vibrations

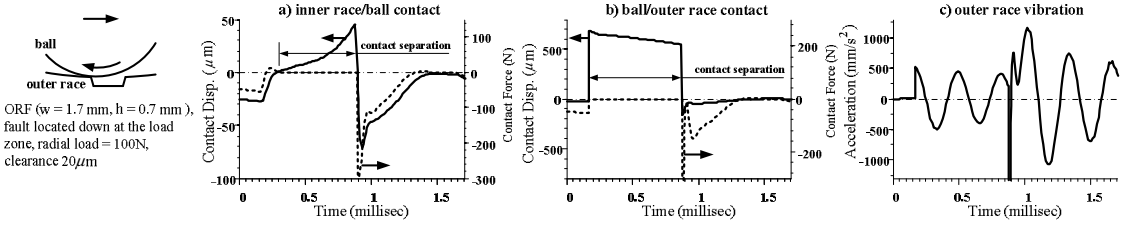


Figure 28 Nonlinear dynamics of rolling contacts with ORF, a) inner race/ball contact, b) ball/outer race contact, c) bearing vibrations

Localized faults can induce surface separations, with concomitant zero contact force. At the same time, the other contact of the ball, with no faults engaged, is affected by the fault. Surface defects generate a nonlinear force pattern consisting of two parts. The first part occurs when the leading edge of the defect engages the contact. The second part, which contains the main impulse signals, occurs when the roller element impacts the

trailing edge of the defect. This feature can be directly used in fault assessments to estimate the size of defects. However, amplitude of the impulse can be highly influenced by locations of faults with respect to the load zone, and by the radial load. Contact impulse signals pass through elements and create vibrations observed at the outer ring. Therefore, in model-based diagnostics, given the bearings model and presence of loads, the severity of the fault can be assessed from impulse signals.

To study effects of size of faults on the impulse response of rolling element bearings, bearings with faults of different type and size were simulated. Figure 29 and Figure 30 show effects of defect size (w) on dynamics of ball/outer race and inner race/ball contacts respectively, when ORF is engaged. The fault is located at the bottom center of the load zone. Impulses are bigger as the fault size increases. Also, for each case, the time span between two impulses depends on the width of faults.

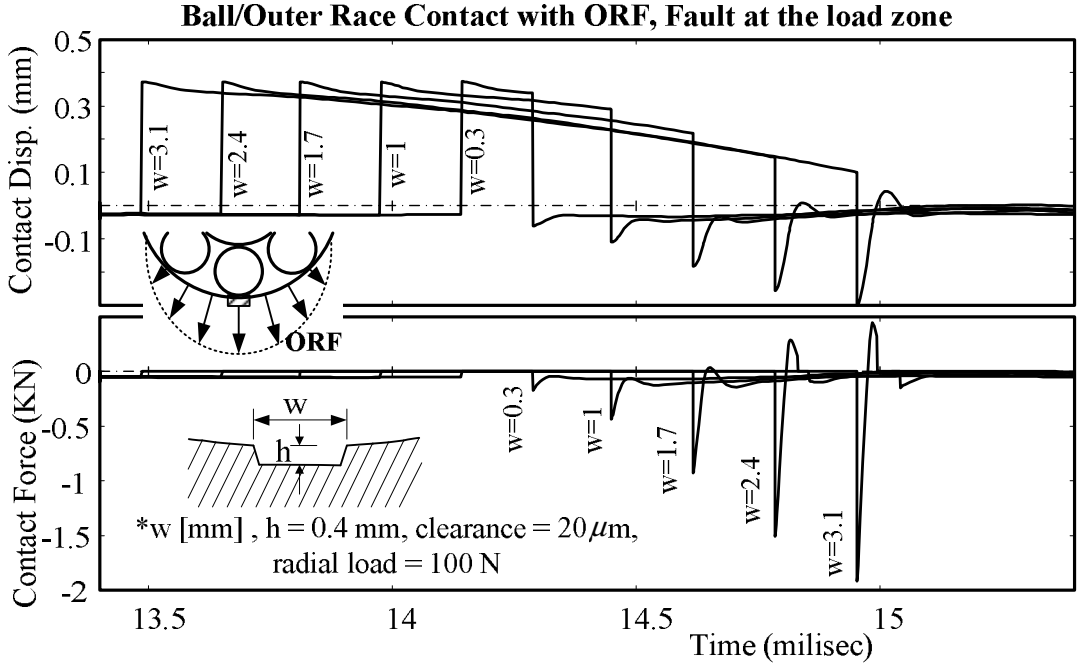


Figure 29 Effects of size of ORF on dynamics of rolling contacts. Displacements (top) and contact forces (bottom) for the contact between balls and outer race.

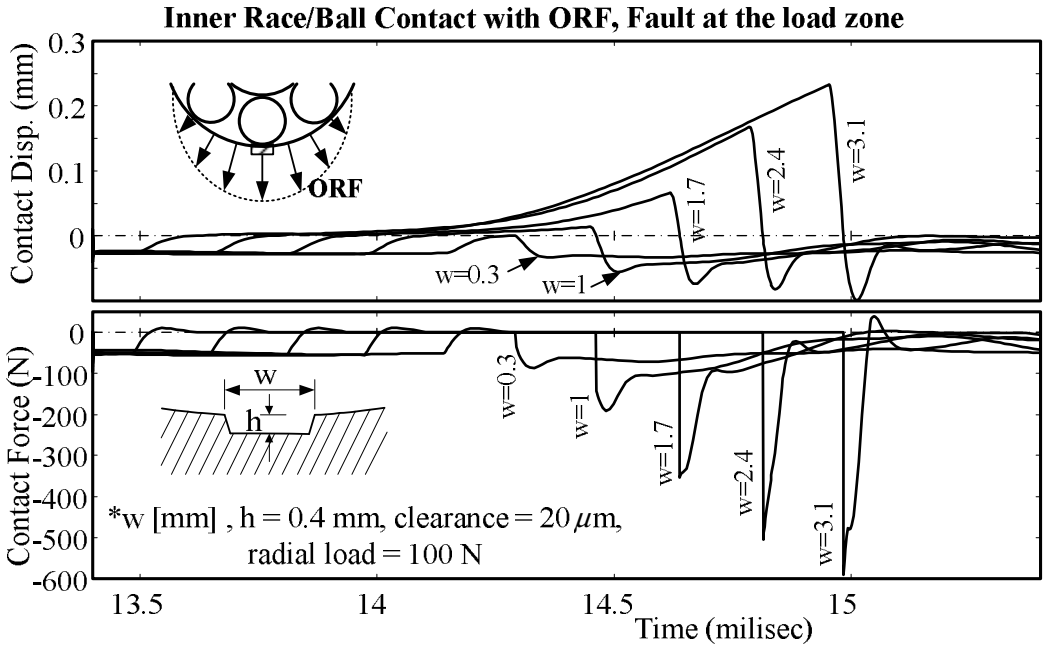


Figure 30 Effects of size of ORF on dynamics of rolling contacts. Displacements (top) and contact forces (bottom) for the contact between inner race and balls.

Maximum absolute values of the impulses due to localized surface defects at contacts are shown for BF and ORF in Figure 31. Nonlinear 2nd order relations between the size of faults ($w$) and maximum values of impulses are observed for BF and ORF. The load zone effect is one of the major sources of nonlinearities. The defective ball is moving down toward the bottom of the load zone. Size of a defect changes the location of trailing edge of the fault in load zone. This change can increase the contact normal loads which intensifies the effect of the fault size in the observed nonlinear relations.

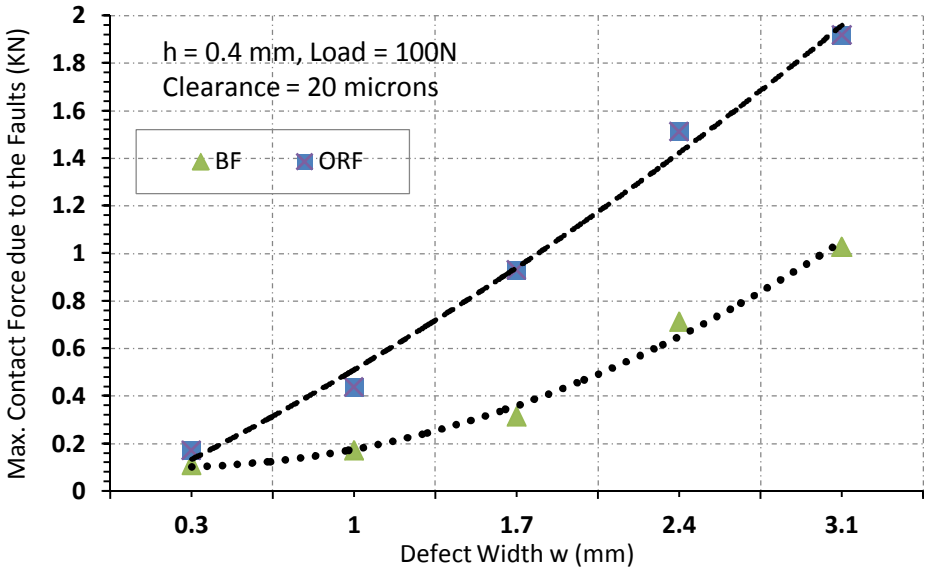


Figure 31 Effects of fault size (w) on the maximum values of impulses generated at rolling contacts due to IRF and BF

## 3.6 SUMMARY AND CONCLUSIONS

A detailed model of rolling element bearings developed in vector bond graphs, incorporated multibody dynamics of elements, centrifugal effects, dynamics of contacts, and surface defects. Newton-Euler's equations for each element were encoded into bond graphs, with dynamics of contacts, traction forces, and rotational frictions formulated as constitutive laws of elements. A kinematic-based fault model was introduced. Tribological faults were modeled as surface profile changes, which generate impulses via dynamic interactions of faults and bearing elements. Fault parameters define type, size, shape, and locations of faults. Simulations for different clearances and radial loads show ability of the model to incorporate load zone effects in vibration signals. Experiments for healthy and faulty rolling element bearings validated the model. A parametric study investigated effects of type, size, and shape of faults on vibration responses. Dynamics of contacts under faults demonstrated how fault impulses are physically generated.

The modular and generic rolling element bearing bond graph model represent complex dynamics of both normal and defective bearings, for rolling element bearings with different geometry and specifications. With physical and kinematic parameters assigned to faults, the model can predict bearing response for fault conditions, and thus be used in model-based diagnostics of rolling element bearings, for information processing necessary for predictive maintenance of machinery.

# Chapter 4

# Feature Plots for Diagnostics of Rolling Element Bearing

## 4.1 INTRODUCTION

Model-based diagnostics detects machine degradation by monitoring states and parameters of the system. Small changes in parameters can be detected. However, for severe damage from shocks, collision, or other instantaneous damage modes, parameters change too fast for the model, or the behavior of the altered system is beyond the scope of the model. A signal-based diagnostic system, in conjunction with the model-based module, can alert of an impending catastrophe.

In this chapter, a machine diagnostic technique, called feature plot, based on time-domain feature extraction and variable window averaging is proposed. Feature plots offer multi-resolution frequency decomposition of time signals, where resolution is inversely proportional to frequency. Unlike wavelet transformation [18, 19], the higher resolution provided by feature plots in low frequencies are ideal for identification of fundamental fault frequencies. First, the feature plot technique will be introduced and formulated in discrete form. The signal processing algorithm will be illustrated for sinusoidal signals. Then, a diagnostics algorithm based on the feature plot technique will be proposed for bearing fault detection and isolation. A test setup will be presented, and the proposed diagnostic technique applied to 28 sets of vibration measurements with different faults and sensor conditions. Results will then be discussed in detail, and fault indicators obtained from frequency feature plots based on shape factor of vibration signals. Furthermore, performance of the proposed diagnostics technique using other time features such as skewness, Kurtosis, peak value, crest factor, impulse factor and mean

absolute values will be evaluated and results presented. Finally, the effectiveness of feature plots in bearing diagnostics with a short available set of data will be shown.

## 4.2 FEATURE PLOT TECHNIQUE

### 4.2.1 Signal Processing Algorithm

Given a waveform signal measured at sampling frequency $f_s$ over time $T$ stored in an array $\mathbf{D}$ with $N$ samples, the feature plot can b obtained by first splitting $\mathbf{D}$ into $n_s$ segments $\mathbf{d}_i$ containing $n$ samples each. Hence, $n_s$ is the integer quotient as $n_s = N \setminus n$, where the operator $\setminus$ in ratio $N \setminus n$ obtains the integer part of the ratio and truncate the remainder. Therefore, the $k^{\text{th}}$ entity of the segment vector $\mathbf{d}_i$ is

$$\mathbf{d}_i(k) = \mathbf{D}(k + n(i-1)), \quad i = 1,2,...,n_s \text{ and } k = 1,2,...,n \tag{1}$$

Then, average signal vector $\overline{\mathbf{d}}$ is constructed from the $n_s$ segments of $\mathbf{d}_i$ as

$$\begin{aligned} \overline{\mathbf{d}}(k) &= \frac{1}{n_s}\sum_{i=1}^{n_s}\mathbf{d}_\mathbf{i}(k) \\ &= \frac{1}{(N \setminus n)}\sum_{i=1}^{N \setminus n}\mathbf{D}(k + n(i-1)), \quad k = 1,2,...,n \end{aligned} \tag{2}$$

The average signal vector $\overline{\mathbf{d}}$ contains $n$ samples and is a function of the total number of samples $N$, and the number of samples in each segment $n$.

After averaging, time domain features of the average signal such as mean, RMS, Kurtosis, crest factor, skewness, shape factors or impact factors are extracted. Values of extracted features are functions of $n$ since $\overline{\mathbf{d}}$ is determined by the size of segments. Time-domain features can be plotted over the range of $n$, constructing the feature plot. Depending on the nature of faults and signals, different time-domain features can assess data and monitor the health condition of the system. Here, shape factor is selected as a time feature to demonstrate the algorithm. Note that negative values of signals can set

average values to zero, losing information in feature plots. Absolute values of signals $|\mathbf{D}|$ can keep fault impulses information. Using absolute values of signals may result peaks in feature plots at the frequencies twice the original frequency.

Shape factor, defined as the ratio of RMS to the average value, for the average signal $\bar{\mathbf{d}}$ is

$$\mathrm{SF}(n,N) = \frac{\mathrm{RMS}(\bar{\mathbf{d}})}{\mathrm{Avg}(\bar{\mathbf{d}})} = \frac{\sqrt{\frac{1}{n}\sum_{k=1}^{n}\left[\bar{\mathbf{d}}(k)\right]^2}}{\frac{1}{n}\sum_{k=1}^{n}\bar{\mathbf{d}}(k)}. \tag{3}$$

Substituting $\bar{\mathbf{d}}(k)$ from Eq. (2) into Eq. (3), the shape factor feature plot is obtained as

$$\mathrm{SF}(n,N) = \frac{\sqrt{\frac{1}{n}\sum_{k=1}^{n}\left[\frac{1}{N\setminus n}\sum_{i=1}^{N\setminus n}\left|\mathbf{D}\left(k+n(i-1)\right)\right|\right]^2}}{\frac{1}{n}\sum_{k=1}^{n}\frac{1}{N\setminus n}\sum_{i=1}^{N\setminus n}\left|\mathbf{D}\left(k+n(i-1)\right)\right|}, \tag{4}$$

which simplifies to

$$\mathrm{SF}(n,N) = \frac{\sqrt{n(N\setminus n)\sum_{k=1}^{n}\left[\sum_{i=1}^{N\setminus n}\left|\mathbf{D}\left(k+n(i-1)\right)\right|\right]^2}}{\sum_{k=1}^{n}\sum_{i=1}^{N\setminus n}\left|\mathbf{D}\left(k+n(i-1)\right)\right|}. \tag{5}$$

Given $N$ data samples, the SF can be plotted over the segment size $n$, constructing the SF feature plot of the signal.

The segment size $n$ can be related to the time $t$ and frequency $f$ as

$$t = \frac{n}{f_s} \tag{6}$$

$$f = \frac{f_s}{n} \tag{7}$$

where $f_s$ is the sampling frequency. Substituting $n$ from Eqs. (6) or (7) into Eq. (5), the SF will be a function of time, giving the time feature plot, or a function of frequency, giving the frequency feature plot. Time feature plots are plotted versus the segment size

in samples $n$ or in time $t$, and frequency feature plots are plotted versus frequency $f$, corresponding to the segment size. Note that feature plots are not constructed by frequency analysis techniques such as Fourier transforms, but obtained directly from time analysis. The ordinate represents time features of the signal and the abscissa is either time or frequency.

Constructing shape factor feature plots for a periodic signal with frequency components $f_{\mathrm{i}}$, large peaks appear as harmonics in the time feature plot at segment sizes $n_{\mathrm{i}}$ or $t_i$ defined by Eqs. (6) and (7), and in the frequency feature plot at equivalent frequencies $f_i$. Having vibration signals from a rotating machine with faults, feature plots may contain peaks at fault frequencies or at segment sizes associated with fault signals. This extracted information from feature plots can produce fault indicators for a system to detect and isolate faults.

### 4.2.2 Example

To illustrate, measurement data D in vector form containing 3141 samples from sinusoidal function $y = \sin(x)$ was sampled at frequency $f_{\mathrm{s}} = 3141$ Hz for 1 second. Figure 32(A) plots $\mathbf{D}$ and absolute values $|\mathbf{D}|$. Signal vector $\mathbf{D}$ was then divided into segments of $n$ samples each, and segments were averaged via Eq. (2), see Figure 32(B). For example, for the case (a), each segment $\mathbf{d}_i$ contains 314 data points ($n = 314$), and 10 non-overlapping consecutive segments are produced by splitting the set of data $|\mathbf{D}|$ ($n_s = {}^{3141}/_{314} = 10$). Taking the average of 10 segments $\mathbf{d}_i$, the average vector $\bar{\mathbf{d}}$ is produced. For cases (a), (c) and (e), shapes of averaged signals resemble the original segments, since segments overlap. Then, shape factors are plotted versus segment size in Figure 32(C), to construct the time feature plot. The first peak at $n = 314$ in Figure

32(C) corresponds to the segment (a) which is based on the first 314 samples. This peak at $n = 314$ implies that RMS$(\bar{\mathbf{d}})$ is 1.116 times Avg$(\bar{\mathbf{d}})$. However, for cases (b) and (d) with $n = 471$ and 785 respectively, individual segments overlap out of phase so the overall shape resembles rectified sinusoidal ripples with much smaller amplitude and twice the original frequency. Therefore, average values are close to RMS values with shape factors near unity (1.005), see Figure 32(C). For segments bigger than half the main signal D, since just one segment is available ($n_s = 1$), the average signal equals the original segment, and calculated features equal the features of the original signal. Therefore, in general feature plots are constructed for half of the data $(0 < n < N/2)$. Time feature plot in Figure 32(C) with horizontal axis: segment size $n$ is transformed to the frequency feature plot in Figure 32(D) by substituting $n$ with $f_s/f$.

The original frequency of the absolute sinusoidal signal is 10 Hz. The time feature plot in Figure 32(C) shows a peak at $n = 314$, and the frequency feature plot shows the corresponding peak at 10 Hz. These values corresponds to the segment (a) representing the fundamental frequency of the signal. Therefore, first harmonics from left in the time feature plot and from right in the frequency feature plot pinpoint the main oscillation of the signal.

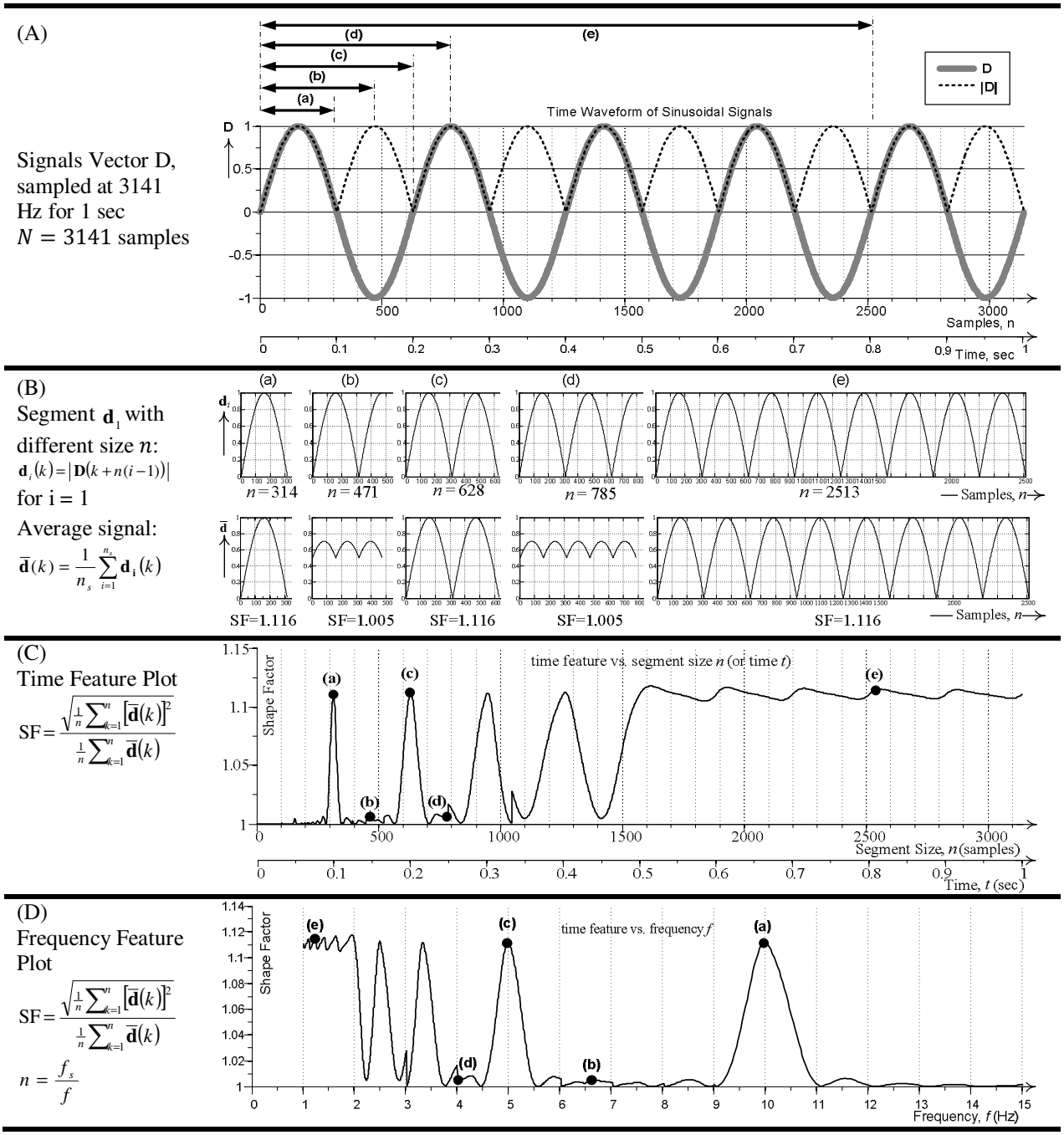


Figure 32 Feature Plot of a sinusoidal function. (A): waveform signal D and its absolute values $|\mathbf{D}|$, (B): segments $\mathbf{d}_i$ with different sizes and corresponding averaged signals $\bar{\mathbf{d}}$, (C): time feature plot, (D): frequency feature plot

## 4.3 DIAGNOSTICS ALGORITHM FOR ROLLING ELEMENT BEARINGS

Vibration signals of faulty bearings show impulses generated by surface element defects. Typical vibration signals for bearings with inner race faults (IRF), ball faults (BF), and outer race faults (ORF) are shown in Figure 33. Frequency and shape of vibration impulses are characteristics of type and severity of bearing faults. Vibration sensors are often mounted on machine frame. The outer race is usually stationary with respect to the frame, whereas balls and the inner race move with respect to the machine frame. Thus, vibration signals from ORF are stationary, whereas signals from BF and IRF are modulated as shown in Figure 33. Since IRF and BF pass through the load zone periodically, modulations corresponding to the shaft and cage frequencies appear in their measured vibration signals. Also, three dimensional rotations of balls can prevent engaging of BF with contacts, adding random modulations to vibration signals. Detection and classification of bearing faults often requires complicated signal processing techniques. Effectiveness is often overshadowed by this complexity, especially for IRF and BF with more complicated behavior.

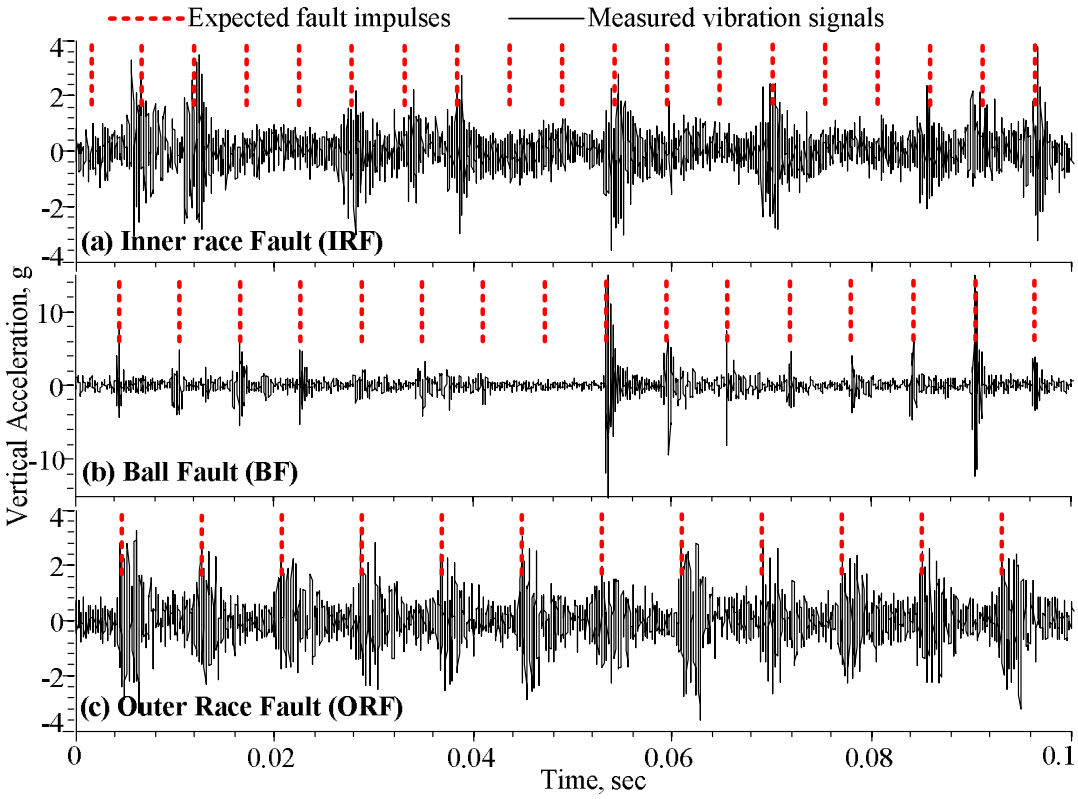


Figure 33 Raw vibration signals measured from a bearing (Table 1) with (a) inner race fault, (b) ball fault, and (c) outer race fault. Sampling frequency: 76800 Hz, and for experiment setup refer to section 4.

Here, the proposed signal processing technique, feature plot, is applied to rolling element bearings to detect and isolate bearing faults from vibration signals. The diagnostic algorithm is shown in Figure 34. Vibration signals (accelerations) and shaft rotating speed are measured, and the time feature plot representing shape factors is obtained. Feature plots for faulty and healthy bearings are compared; yielding the residual feature plot, which is transformed into the frequency residual feature plot. Fault regions on the frequency feature plot are defined based on the first harmonics of fault frequencies, and fault indicators are obtained from the power of peaks in the feature plot

within fault regions. Note that any time feature can be used in the algorithm. Here, shape factor represent the time feature and the feature function is shown as SF.

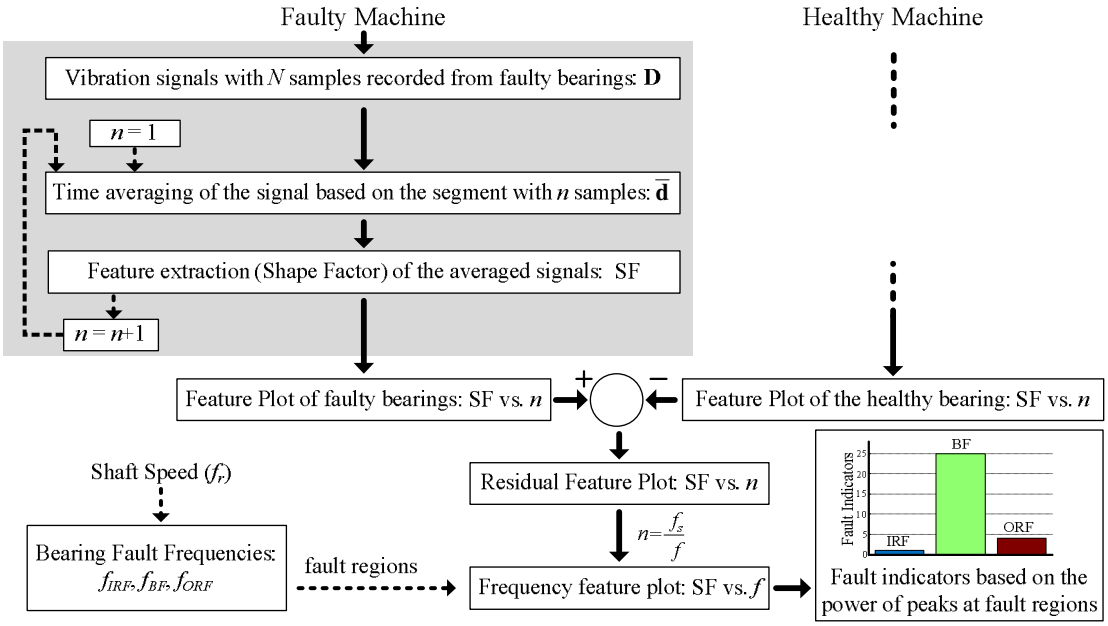


Figure 34 Process algorithm for detection and isolation of rolling element bearing faults using feature plot technique.

Bearings fault frequencies are functions of bearing specifications and rotor speed [28] as

Inner Race Fault Frequency:
$$f_{IRF} = \frac{n}{2} f_r \left(1 + \frac{d_b}{d_p} \cos\phi\right) \tag{8}$$

Outer Race Fault Frequency:
$$f_{ORF} = \frac{n}{2} f_r \left(1 - \frac{d_b}{d_p} \cos\phi\right) \tag{9}$$

Ball Fault Frequency:
$$f_{BF} = \frac{d_p}{d_b} f_r \left(1 - \frac{{d_b}^2}{{d_p}^2} \cos^2\phi\right) \tag{10}$$

where $n$ is the number of balls, $f_r$ is the rotor speed, $d_b$ is balls diameter, $d_p$ is bearing pitch diameter, and $\phi$ is the bearing contact angle. In frequency feature plots, fault regions center at fault frequencies, with deviation widths based on the accuracy of rotor

speed measurements. Fault indicators are defined as the ratio of the maximum peak value of the frequency feature plot within the predefined fault regions to the standard deviation of the frequency feature plot signals within a selected range. The selected range contains all fault frequencies. Here, three fault indicators for each bearing are summed and normalized, to show percent contributions of each fault (IRF, BF and ORF) for fault isolation. A dominant fault dominates the normalized fault indicator. Also, magnitudes of fault indicators can be used for fault assessment.

## 4.4 BEARINGS WITH LOCALIZED FAULTS: PITS AND DENTS

### 4.4.1 Experimental Setup

Experiments were conducted on a test rig (Figure 35) with a rotating shaft supported by two rolling element bearings (Table 1) with faults on inner race (IRF), balls (BF) and outer race (ORF). A 3-phase induction motor rotates the shaft through a beam coupling. Bearing loaders apply static radial loads on bearings. The magnetic loader applies adjustable rotational loads to the shaft through the gearbox and belts. Accelerometers measure vertical and horizontal vibrations. Localized faults were created on inner race, outer race and balls by spot grindings. Since excessive vibrations can invalidate results, waterfall plots and hammer tests found machine critical speeds and natural frequencies, which were avoided during tests.

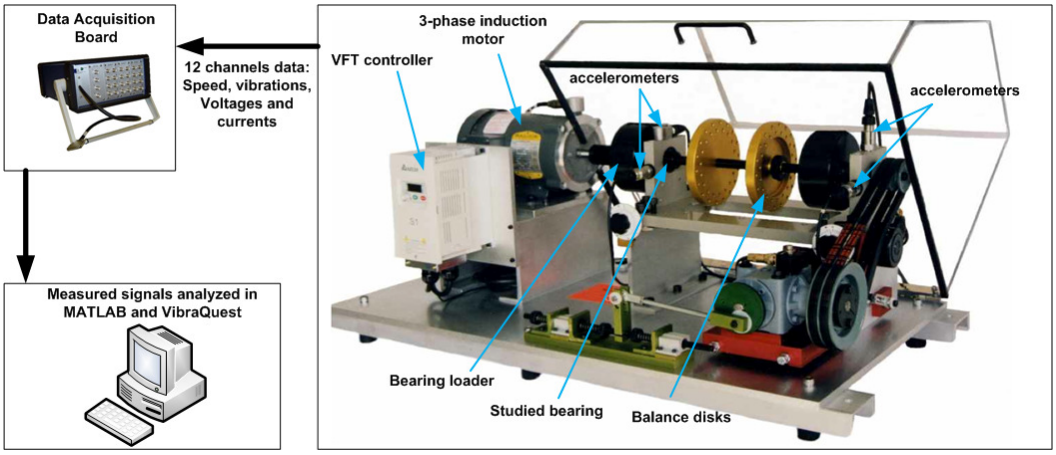


Figure 35 Test rig for rolling element bearing experiments.

Table 3 Bearing specifications and simulations parameters

| Parameter | Value |
|---|---|
| Bearing model No. | MB ER-16K |
| Number of balls | 9 |
| Ball/inner race/outer race diameter [mm] | 7.94 / 31.38 / 47.26 |
| Pitch diameter [mm] | 39.32 |
| Race groove radius [mm] | 4.1 |
| Vertical radial load on inner race [N] | 110 |
| Inner race rotational speed [Hz] | 35 |

At the shaft speed of 35 Hz, bearings with IRF, BF, ORF, and (combined fault) CF were tested. For each case, vertical and horizontal vibration signals and rotor speed were recorded simultaneously via data acquisition board at two different sampling frequencies: 15360 Hz (Low Sampling Frequency: LSF) and 76800 Hz (High Sampling Frequency: HSF). Since outer race is stationary, ORF do not move with respect to the load zone. Therefore, locations of ORF greatly influence the vibration signals. Experiments with ORF at different locations were conducted. Overall, 28 sets of measurements detailed in Table 3 were obtained.

Table 4 Experiments Design (28 cases)

| Type of Faults | Sampling Frequency [Hz] | Acceleration Directions | |
|---|---|---|---|
| | | Vertical | Horizontal |
| Healthy | 76800 | case# 1 | 2 |
| | 15360 | 3 | 4 |
| Inner Race Fault (IRF) | 76800 | 5 | 6 |
| | 15360 | 7 | 8 |
| Ball fault (BF) | 76800 | 9 | 10 |
| | 15360 | 11 | 12 |
| Outer Race Fault (ORF) located down | 76800 | 13 | 14 |
| | 15360 | 15 | 16 |
| ORF located up | 76800 | 17 | 18 |
| | 15360 | 19 | 20 |
| ORF located side | 76800 | 21 | 22 |
| | 15360 | 23 | 24 |
| Combined Faults (CF): IRF, ORF | 76800 | 25 | 26 |
| | 15360 | 27 | 28 |

### 4.4.2 Feature Plots

The diagnostic algorithm sown in Figure 34 was applied to all 28 measurements and performance of feature plot technique in detection and isolation of bearing faults was studied. For each measurement in Table 4, the signal vector D was selected from 0.1 second of measured vibration signals and feature plots were constructed. Results for healthy bearing, IRF, BF, ORF and combined faults (CF) corresponding to the cases 1, 5, 9, 13, and 25 are presented in Figure 36, Figure 37, Figure 38, Figure 39, Figure 40 respectively. Each figure shows (a) waveform vibration signals, (b) shape factor time feature plot, and (c) shape factor frequency feature plot. Fault regions corresponding to the first harmonics of fault frequencies are shaded on feature plots. Given the rotor speed $f_r = 35\text{Hz}$ for the bearing of Table 3, fault components in time and frequency are shown in Table 5.

Table 5 Bearing fault components defining fault regions in feature plots, ($f_r = 35$ Hz, f=76800 Hz)

| | IRF | BF | ORF |
|---|---|---|---|
| Fault Frequencies from Eqs. (6-8): $f$ (Hz) | 189.28 | 166.32 | 125.72 |
| Time equivalent segment size of fault frequencies: $t = 1/f$ (s) | $5.28 \times 10^{-3}$ | $6.01 \times 10^{-3}$ | $7.95 \times 10^{-3}$ |
| Samples equivalent segment size: $n = f_s/f$ (samples) | 406 | 462 | 611 |

Vibration waveform of the healthy bearing in Figure 36(a) shows background noise, low amplitude oscillations due to misalignments and imbalance, but no major signs of fault impulses. Time feature plot in Figure 36(b) shows shape factors vs. segment size $n$ and the frequency feature plot in Figure 36(c) shows shape factors vs. frequency $f$. At the frequency range containing fault regions (100-200 Hz) in Figure 36(c), the rotor speed harmonic at 140Hz is observed as a small raise. A small peak in the ORF region is explained by the location effect, i.e., balls passing across the accelerometer. But, no signs of bearing faults at fault regions are seen.

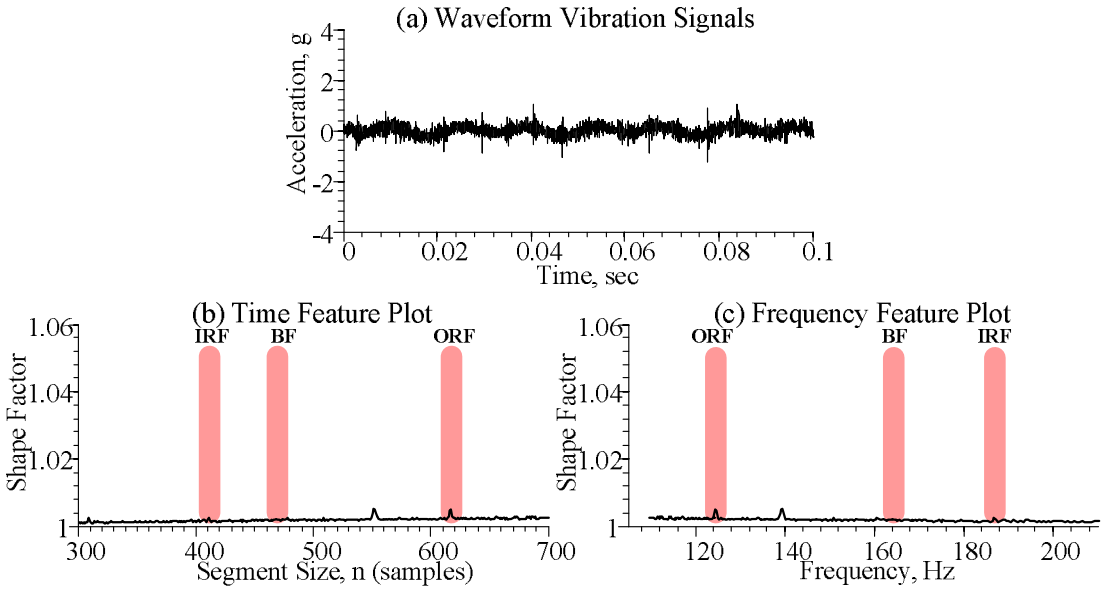


Figure 36 Results for the healthy bearing (case 1): (a) time waveform vibration signals, (b) shape factor time feature plot, (c) shape factor frequency feature plot. ($f_r = 35$ Hz, $f_s = 76800$ Hz )

For IRF, fault impulses appear in Figure 37(a). Inner race faults, fixed on the inner race, pass through the load zone at a frequency $f_r$, as the inner race rotates. Faults in the load zone generate strong impulses, but disappear or weaken outside the load zone. Shape factor feature plots clearly indicate inner race faults by peaks in the IRF region. In Figure 37(b), $n = 406$, equivalent to one period of IRF impulses (5.28 ms), represents the maximum shape factor when signals are averaged with this segment size and in Figure 37(d), the peak appear at the equivalent frequency 189.28 Hz. Since the vertical axis represents time features, faults severity is related to amplitudes of feature plot peaks in fault regions. Note that peaks in other regions of feature plots represent other periodic features of machine. However, first harmonics of fault components always appear in fault regions, if fault impulses are present in vibration signals.

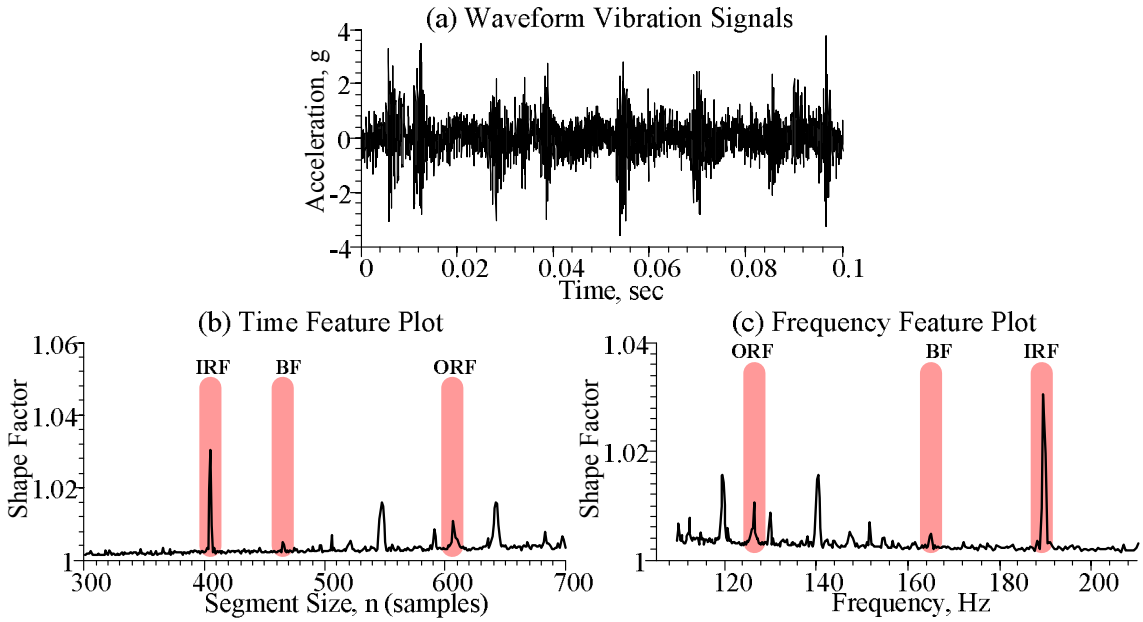


Figure 37 Results for the bearing with IRF (case 5): (a) time waveform vibration signals, (b) shape factor time feature plot, (c) shape factor frequency feature plot. ($f_r = 35$ Hz, $f_s = 76800$ Hz )

Figure 38(a) shows vibration waveform of the bearing with ball fault (BF). Fault signals spaced by the fault frequency timing ($1/f_{BF}$) are modulated by the cage frequency (about 14Hz), due to the load zone effect. Three dimensional rotations of balls can prevent engaging of ball faults with races, causing randomness in signals, making the diagnosis more complicated. Feature plots in Figure 38(b) and (c) clearly pinpoint the fault, and show the severity via the amplitude of the peak in BF regions. Signal averaging compensates any irregular characteristics of signal due to the load zone effect or due to three dimensional rotations of balls, making the feature plot technique effective for detection and isolation of bearing faults.

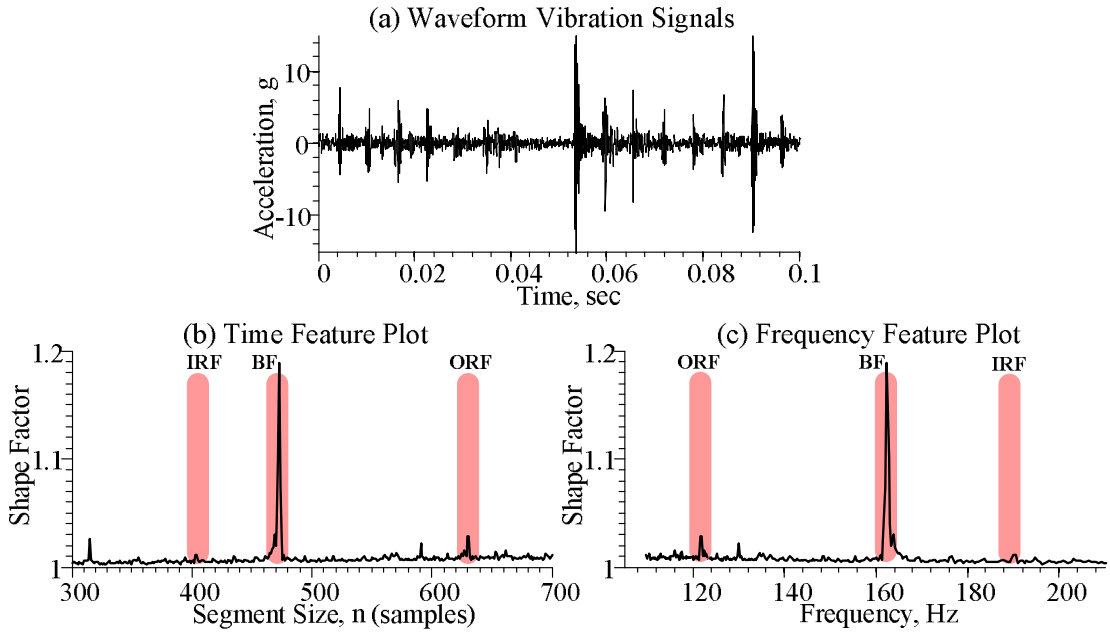


Figure 38 Results for the bearing with BF (case 9): (a) time waveform vibration signals, (b) shape factor time feature plot, (c) shape factor frequency feature plot. ($f_r = 35$ Hz, $f_s = 76800$ Hz )

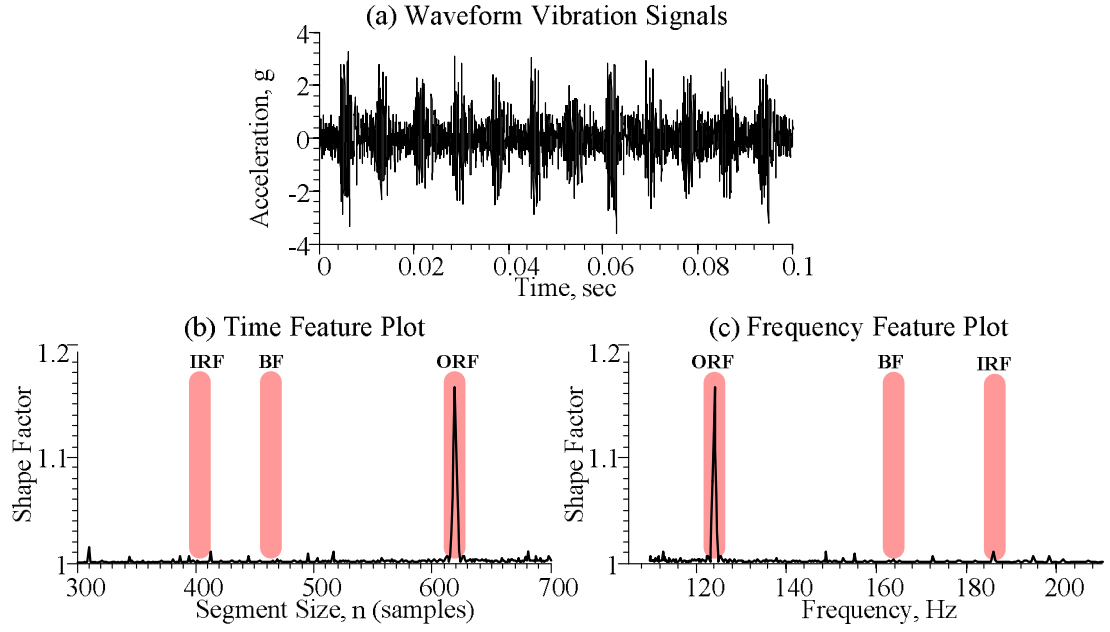


Figure 39 Results for the bearing with ORF (case 13): (a) time waveform vibration signals, (b) shape factor time feature plot, (c) shape factor frequency feature plot. ($f_r = 35$ Hz, $f_s = 76800$ Hz )

For ORF, regular impulse pattern appears in the vibration in Figure 39(a). Feature plots in Figure 39(b) and (c) exhibit strong peaks in ORF regions without other obfuscating frequencies. Note that the original vibration signals were used without filtering. Combined Faults (CF) with IRF and ORF in Figure 40(a) have vibration signals more contaminated by fault impulses, making fault detection more complicated. Feature plots clearly pinpoint the presence of IRF and ORF in Figure 40(b) and (c), via peaks in these fault regions, with amplitudes related to severity of the faults.

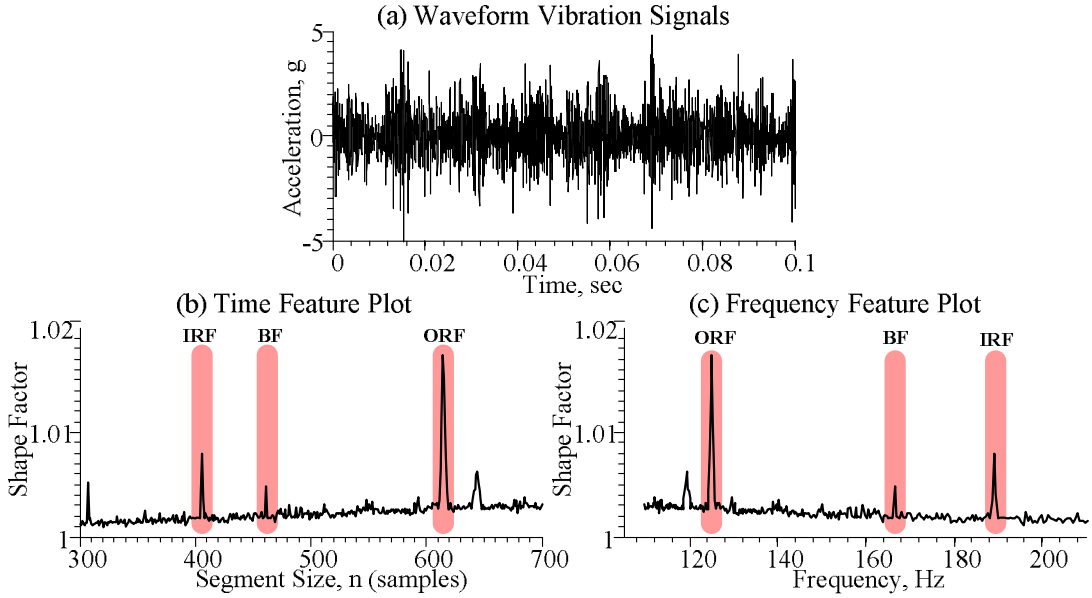


Figure 40 Results for the bearing with combined faults (CF), case 25: (a) time waveform vibration signals, (b) shape factor time feature plot, (c) shape factor frequency feature plot. ($f_r = 35$ Hz, $f_s = 76800$ Hz )

Shape factor frequency feature plots for all 28 sets of vibration measurements are summarized in Figure 41. Columns correspond to fault conditions and rows correspond to measurement directions (vertical and horizontal) and sampling frequencies (High Sampling Frequency: HSF, Low Sampling Frequency: LSF). Case numbers referring to measurement conditions in Table 4 are labeled on each plot.

Feature plots of healthy bearings in Figure 41 (cases 1-4) have no major peaks. For cases 5-16 corresponding to the IRF, BF, and ORF, feature plots clearly pinpoint faults via peaks in fault regions. For ORF with the fault outside the load zone (column 5), feature plots detect the fault for all sets of data, except case 20 where the horizontal vibration signals sampled at low frequency contain little fault information. Outer race faults located at the side (column 6, cases 21-24) are detected easily with feature plots for all sets of data, especially with horizontal vibration signals (cases 22,24). For, the case with combination of IRF and ORF, vertical measurements with high sampling frequency (case 25) detect both IRF and ORF, horizontal measurements with high sampling frequency (case 26) detect IRF but have little information on ORF, vertical measurement with low sampling frequency (case 27) detect both faults, and horizontal measurements with low sampling frequency (case 28) detect IRF with little information on ORF faults. Comparing feature plots of low sampled to high sampled data, peaks indicating faults in feature plots from HSF measurements are stronger than from LSF measurements. Comparing plots from vertical measurements with ones from horizontal measurements, detection of IRF and BF is insensitive to sensor direction. However, for ORF with faults located down or up, vertical measurements provide more information. When faults are located at sides, horizontal measurements are much more effective.

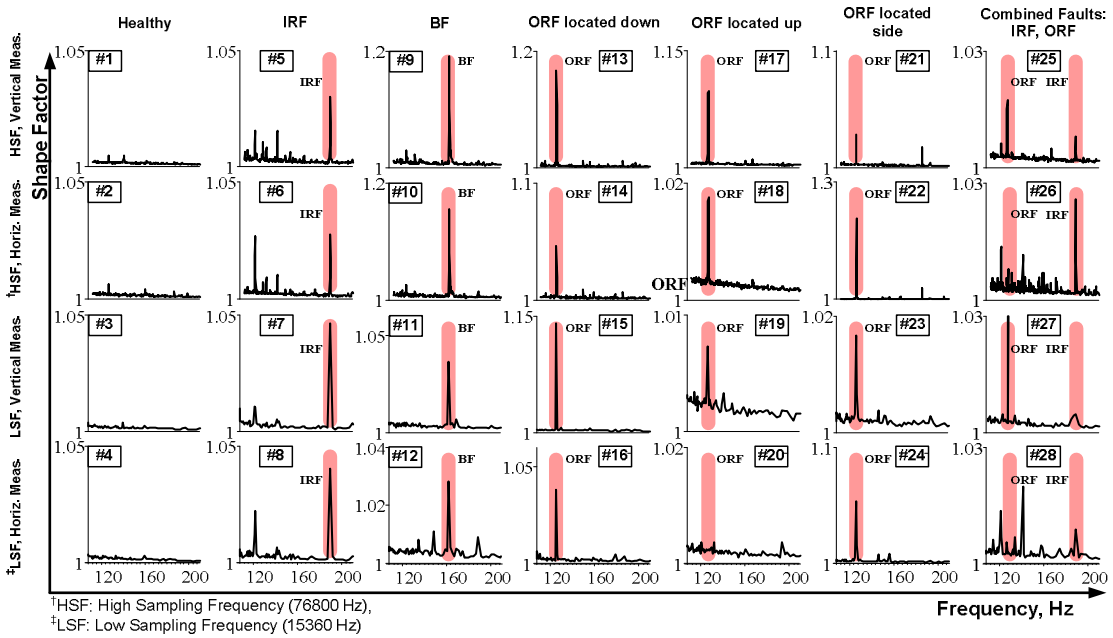


Figure 41 Frequency feature plots for 28 cases of vibration measurements (Table 4) from bearings with different faults.

### 4.4.3 Fault Indicators

Fault indicators for all 28 measurements of Table 4, processed by the algorithm in Figure 34, are displayed as bar plots in Figure 42(a) and normalized in Figure 42(b). Absolute fault indicators in Figure 42 (a) detect faults and assess severity. The height of each bar contains information on severity of faults. Normalized fault indicators in Figure 42(b) show the contribution of each fault and can be used for fault isolation.

Feature plots can detect, isolate and assess rolling element bearing faults from vibration signals with different measurement and fault conditions. The effectiveness of the proposed fault detection technique with both horizontal and vertical vibration signals measured with either high or low sampling frequencies is a big advantage. Note that results were based on 1 second of vibration measurements. Figure 42(a) shows that the

best results are from high sampling rate signals measured along vertical directions (cases 5, 9, 13, 17, 21, 25), because bearing housings are stiffer along vertical than horizontal directions, and horizontal measurements are more prone to imbalance and misalignment contamination signals.

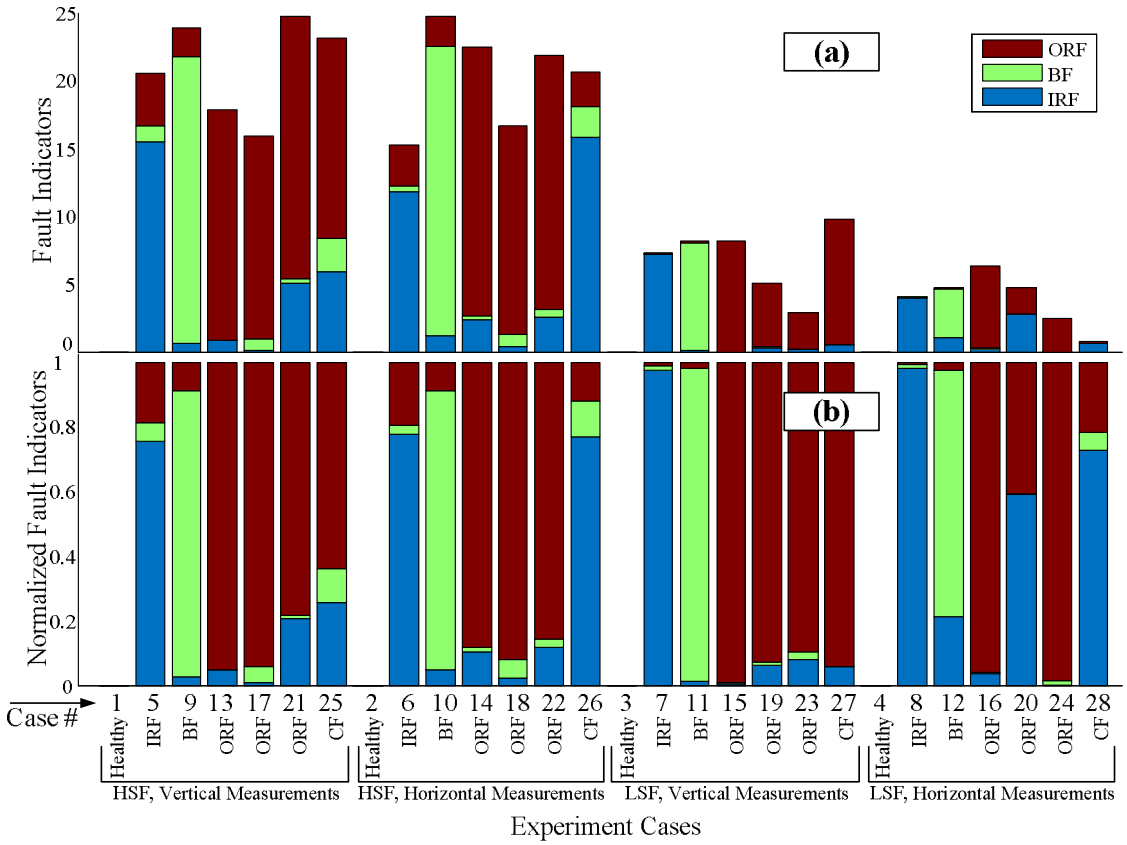


Figure 42 Fault indicators obtained from feature plots for 28 cases of vibration measurements (Table 4) for different fault conditions. (a) Fault indicators, (b) Normalized fault indicators

Feature plots present time domain features of signals versus time or frequency. Here, shape factor was used in feature plots for diagnostics or rolling element bearings. For machine diagnostics, based on physics of the fault, various features can be used in feature plots for fault detection. Since localized faults in bearings generate impacts, any

time feature with characteristics of impulsiveness can be used in feature plots to detect bearings faults. Some of these time features are given in Eqs. (11-18) [85].

Skewness: $$SK = \frac{\frac{1}{N}\sum_{i=1}^{N}(X_i - \bar{X})^3}{\sigma^3} \quad (11)$$

Kurtosis: $$K = \frac{\frac{1}{N}\sum_{i=1}^{N}(X_i - \bar{X})^4}{\sigma^4} \quad (12)$$

RMS: $$RMS = \sqrt{\frac{1}{N}\sum_{i=1}^{N}(X_i - \bar{X})^2} \quad (13)$$

Peak Value: $$X_p = \frac{1}{2}[\max(X_i) - \min(X_i)] \quad (14)$$

Crest Factor: $$CF = \frac{X_p}{RMS} \quad (15)$$

Shape Factor: $$SF = \frac{RMS}{\bar{X}} \quad (16)$$

Impulse Factor: $$IF = \frac{X_p}{\bar{X}} \quad (17)$$

Mean Absolute Deviation: $$X_{MAD} = \frac{1}{N}\sum_{i=1}^{N}|X_i - \bar{X}| \quad (18)$$

where **X** is the signal vector with $N$ samples, mean value $\bar{X}$ and standard deviation $\sigma$.

The proposed diagnostics technique with different time features given in Eqs. (11)-(18) was applied to bearings with IRF (case 5), BF (case 9), and ORF (case 13), and fault indicators were shown in Figure 43. Feature plots successfully detect and isolate bearing faults (IRF, BF, ORF) with almost all time-based features given above. To increase the reliability and accuracy of diagnostics, multi features can be monitored at the same time and the final decision on the health of machine can be made based on a probability analysis of fault indicators.

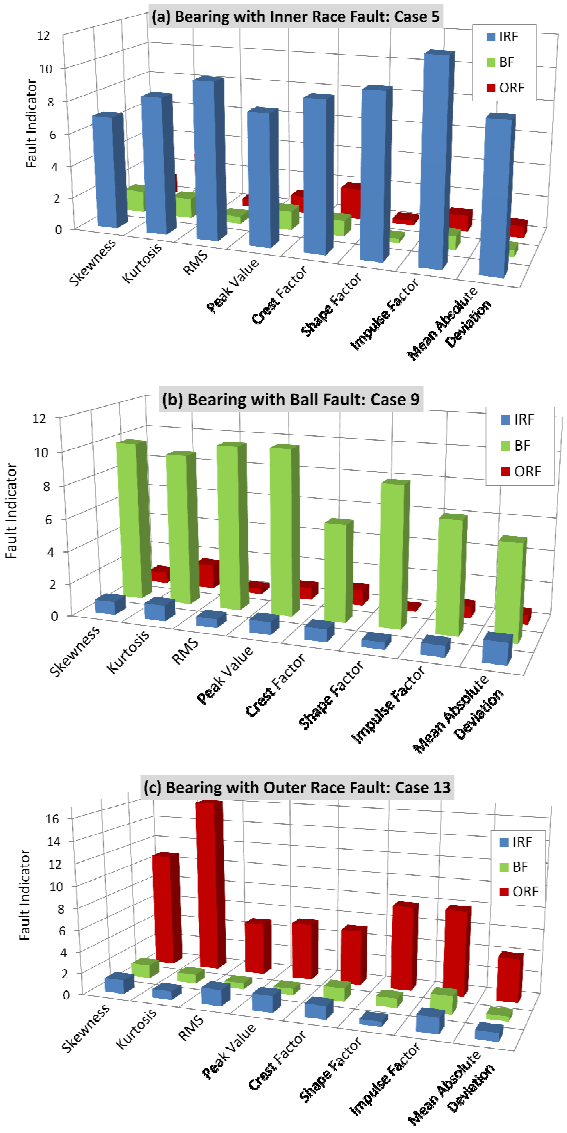


Figure 43 Fault indicators obtained from feature plots using different time features detect (a) inner race fault, (b) ball fault, and (c) outer race fault from vibration measurements.

### 4.4.4 Bearing Diagnostics with Short Set of Data

The horizontal axis in the time feature plot has the same number of data points, and the same resolution as the original time signals. However, the nonlinear transform generates a horizontal axis for frequency feature plots with the same number of

samples but variable resolution. High resolutions at low frequencies and low resolutions at high frequencies are obtained. This characteristic of frequency feature plots brings an advantage to diagnostics of rotating machinery with low range fault frequencies. To demonstrate this performance, sets of vibration measurements for 0.1 seconds with 7680 samples were obtained from bearings with IRF, BF, and ORF. Frequency feature plots were obtained and compared with power spectra of the signal in Figure 44. Due to finite numbers of samples, power spectral plots have insufficient resolution in the range of first harmonics of fault frequencies and fault components should be searched at higher frequencies. However, feature plots clearly pinpoint faults in all three cases. This is advantageous when the number of measured samples is limited.

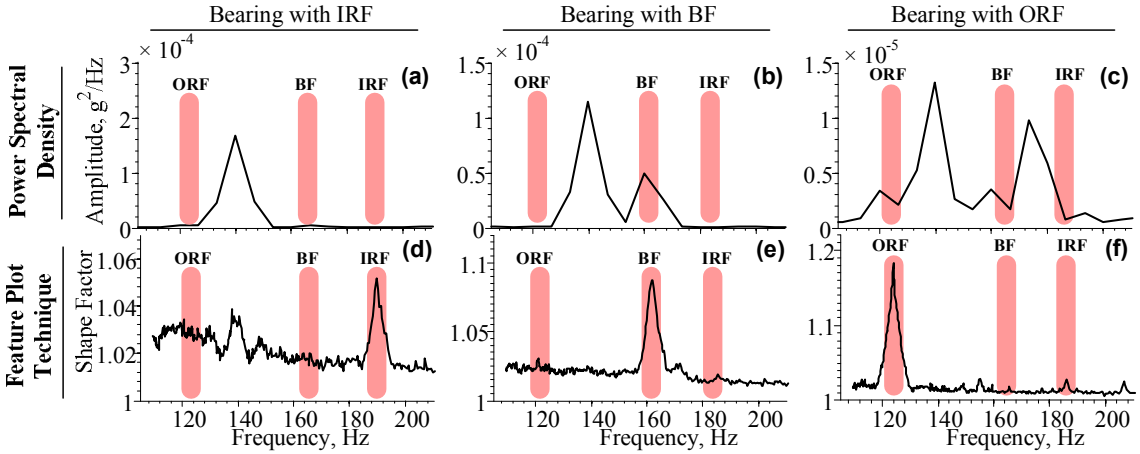


Figure 44 Feature plot technique compared to frequency-based methods (PSD) in finding bearing fault frequencies in low frequency range when data samples are limited. (T = 0.1 sec, 7680 samples, $f_r = 35$ Hz, $f_s = 76800$ Hz)

## 4.5 BEARINGS WITH MILD LOCALIZED FAULTS: ROUGH SURFACE

Severe localized faults in bearings such as dents, pits and spalls generate visible fault impulses in vibration signals which can be easily detected using feature plots. However, mild bearing faults such as rough surfaces or localized faults at their early stages generate insignificant signals and cannot be easily detected using time features. Also, other faults such as misalignment and imbalance may contaminate original signals and mask the bearing fault signals. Feature plot technique, in conjunction with higher derivations of vibration signals detect minor faults such as rough surface. Experiments data from bearings with rough surface faults were used to show the performance of the technique.

### 4.5.1 Experiments Setup

Experiments (Table 7) were conducted on a test rig with rolling element bearings (Table 6). Rough surface faults were created by spot grinding on inner race (IRF), ball (BF) and outer race (ORF). Outer race was stationary, and inner race was rotating. Bearings were under radial load 110 N and ORF was located in the load zone. At the shaft speed of 6.04 Hz, bearing vibration signals and rotor speed were recorded at sampling frequency: of 48000 Hz in the presence of imbalance and misalignment faults.

Table 6 Bearing and experiment specifications

| Parameter | Value |
|---|---|
| Number of balls | 12 |
| Ball diameter [mm] | 7.12 |
| Pitch diameter [mm] | 38.5 |
| Vertical radial load on inner race [N] | 110 |
| Inner race rotational speed [Hz] | 6.04 |
| Sampling frequency [Hz] | 48000 |

Faults are created as distributed rough surfaces with irregular geometry. Width and maximum depth of rough surfaces in Table 7 represent size and severity of faults. IRF and BF are more severe than ORF since the maximum depths are higher.

Table 7 Experiments and bearing fault specifications

| Experiment Case | Fault Conditions | Size of rough surface faults | |
|---|---|---|---|
| | | Width [mm] | Max Depth [mm] |
| 1 | Healthy | - | - |
| 2 | Inner Race Fault (IRF) | 12 | 0.15 |
| 3 | Ball fault (BF) | 3 | 0.13 |
| 4 | Outer Race Fault (ORF) located down | 10 | 0.07 |

### 4.5.2 Higher Derivatives of Displacements for Rough Surface Faults

Measured acceleration signals for IRF, BF and ORF are shown in Figure 45. Misalignment and imbalance of the shaft generate high amplitude dominant periodic signals observed in waveforms, Figure 45(a-c). Since bearing fault are small, corresponding fault are not easily visible in the waveform. Figure 45(d-f) magnify and indicate bearing fault signals carried by the main oscillation signals.

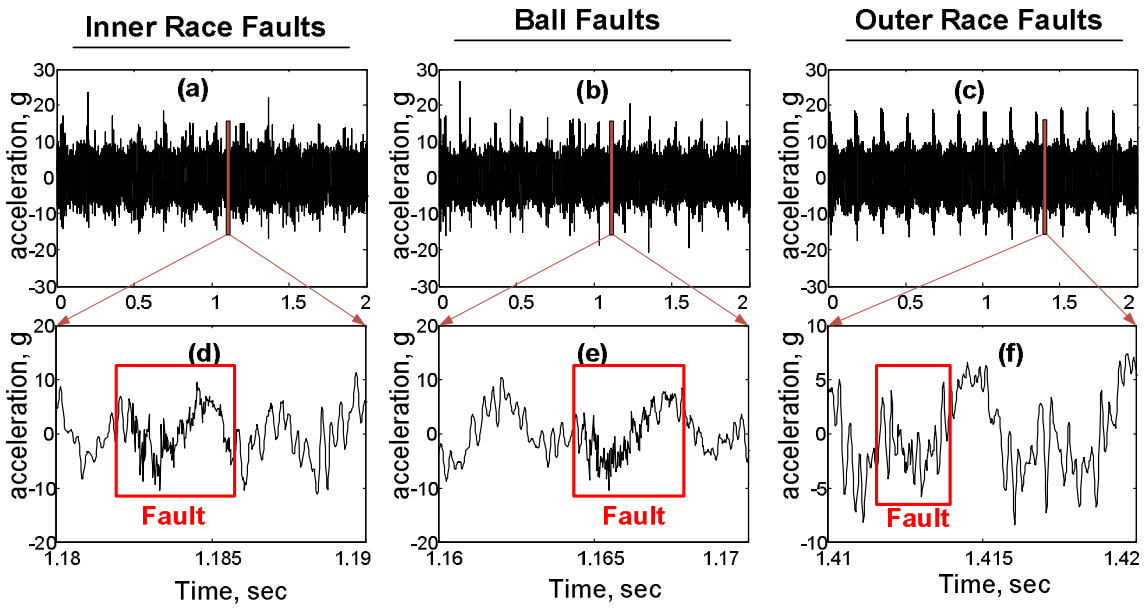


Figure 45 Waveform vibration signals of bearings with IRF (left column), BF (middle column), and ORF (right column). Accelerations are shown in the 1st row and magnified in the 2nd row.

Vibration signals measured by accelerometers represent second derivatives of displacement or acceleration. Severe faults such as dents and spalls generate impacts detectable in 2nd derivatives of displacements. A rough surface fault in rolling contacts generates high-frequency low-amplitude vibrations, in contrast with misalignment and imbalance faults that generate low-frequency high-amplitude vibration signals (around 1-10X). i.e., rough surface signals appear as rapid changes of acceleration signals, which can be detected by derivatives of acceleration. Here, first and second derivatives of acceleration signals isolate and magnify rough surface bearing faults. Figure 46 15 shows accelerations signals and derivatives of accelerations. First derivative of accelerations clearly isolate and magnify signals due to IRF and BF. However, ORF is much less severe with no signs in acceleration signals. In This case, the second derivative of acceleration detects fault signals as shown in Figure 46 (f). Higher derivatives of

accelerations can be easily implemented in discrete form in digital machines since measurements are discrete. Then, sampling frequency determines the minimum time step and can affect the performance of the technique.

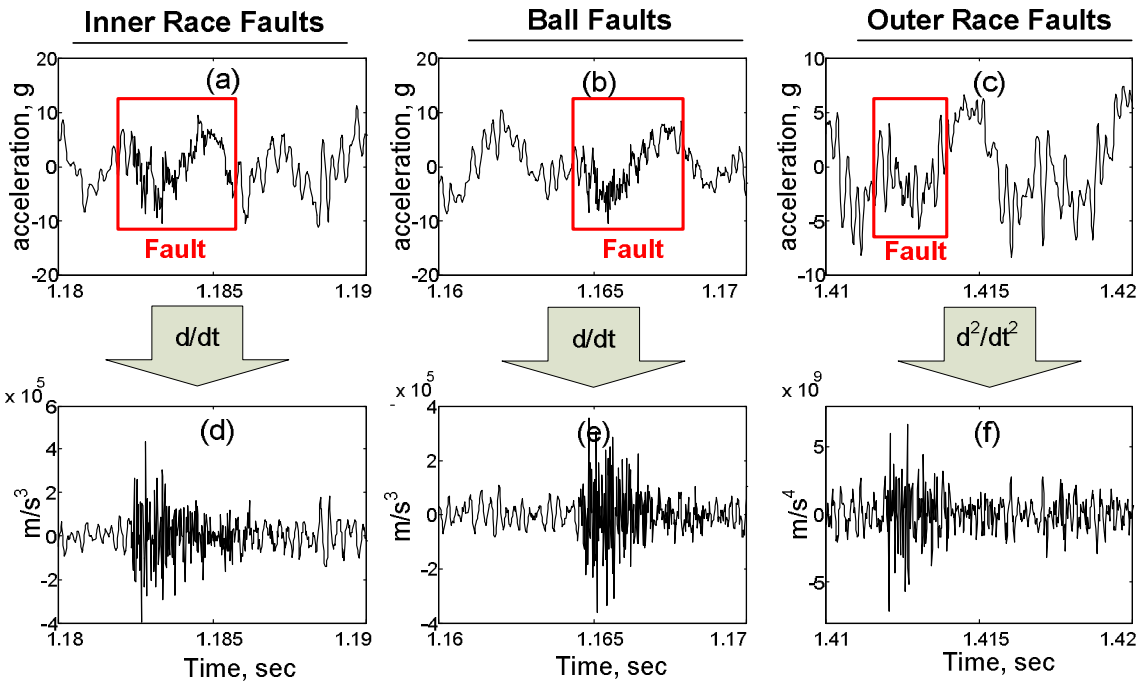


Figure 46 Higher derivatives of acceleration signals amplify fault components. Left column: IRF, middle column: BF, right column: ORF. Top row: acceleration signals, bottom row: higher derivatives of accelerations

Higher derivatives of displacement may amplify the background noise of the signal. Sensor noise, or noise due high frequency structural vibrations of the machine can be extensively increased in higher derivatives and mask bearing fault signals. However, bearing fault signals are periodic with known frequencies and can be distinguished from the background noise. The proposed higher derivative technique is applicable for bearing surface faults generating signals with frequencies higher than the frequency of the background noise. Then, fault signals can be detected in higher derivatives of

accelerations. This technique can be used for more investigation of bearing faults when accelerations signals do not detect bearing faults.

### 4.5.3 Feature Plots and Fault Indicators

Feature plot technique with the algorithm in Figure 34 was applied to higher derivatives of acceleration signals measured from bearings with rough surface faults. Acceleration signals of the healthy bearing, first derivative of acceleration signals of bearings with IRF and BF and second derivates of accelerations for the bearing with ORF faults were used to construct feature plots and to obtain fault indicators. Figure 47, Figure 48, Figure 49 respectively show the results for IRF, BF and ORF based on the shape factor feature.

Vibration signals in Figure 47(a) show periodic signals due to misalignments and rotor imbalance with no visible signs of bearing faults. The first derivative of acceleration signals in Figure 47(b) visibly shows bearing fault signals. The frequency feature plot based on the shape factor clearly shows a peak in the IRF region. The power of the peak for each fault in the selected frequency region (28-45 Hz) defines fault indicators shown in Figure 47(d).

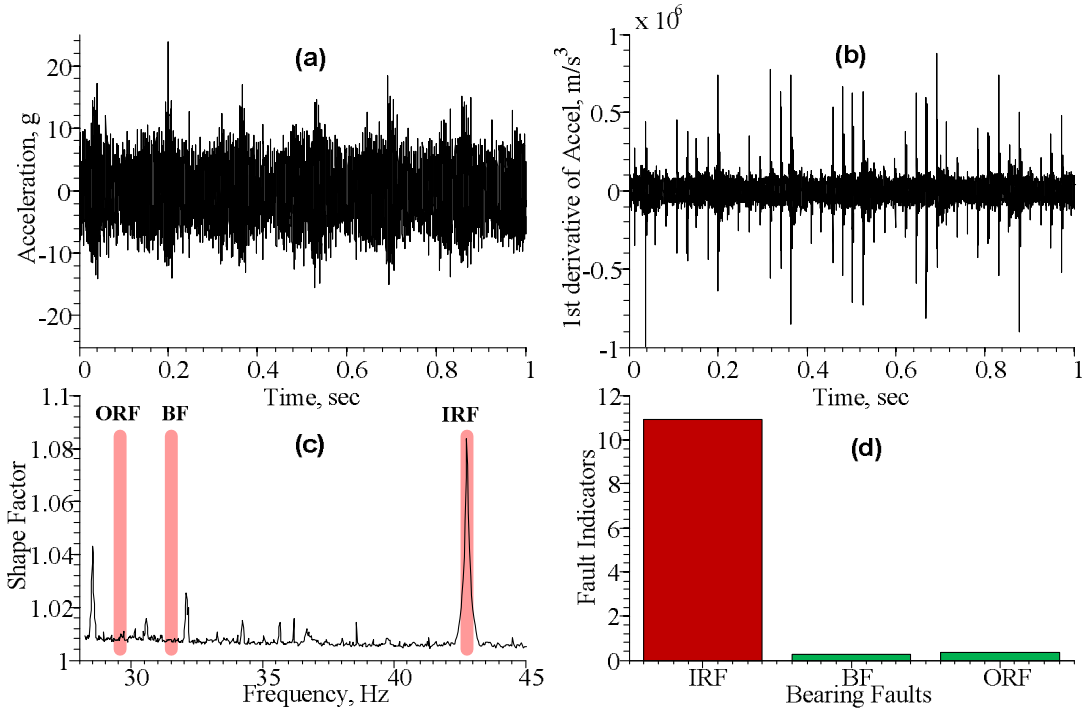


Figure 47 Detection of IRF with Feature Plot technique: a) time waveform vibration signals, b) 1st derivative of vibration signals unmasked fault components as peaks indicating rough surface faults, c) shape factor feature plots of 1st derivative of vibration signals, d) fault indicators showing IRF

For the BF in Figure 48, original vibrations signals contain dominant signals due to misalignment and imbalance with few peaks due to bearing faults. However, bearing fault impulses are highly masked by other signals. The first derivative of vibration signal magnifies and unmasks signals from rough surfaces faults. Feature plot and fault indicators effectively detect and isolate the fault. For ORF, no evidence of bearing faults are seen in the waveform in Figure 49(a). The first derivative also did not provide much information on the fault. However, the second derivative of acceleration signals detect fault signals as shown in Figure 18(b). Note that background noise signals are also magnified and observed. However, bearing fault signals are clearly distinguishable based on their periodic characteristics. The frequency feature plot shows a small peak in ORF

region, indicating the fault. Fault indicators based on the feature plot peaks in fault regions clearly detect and isolate the rough surface fault.

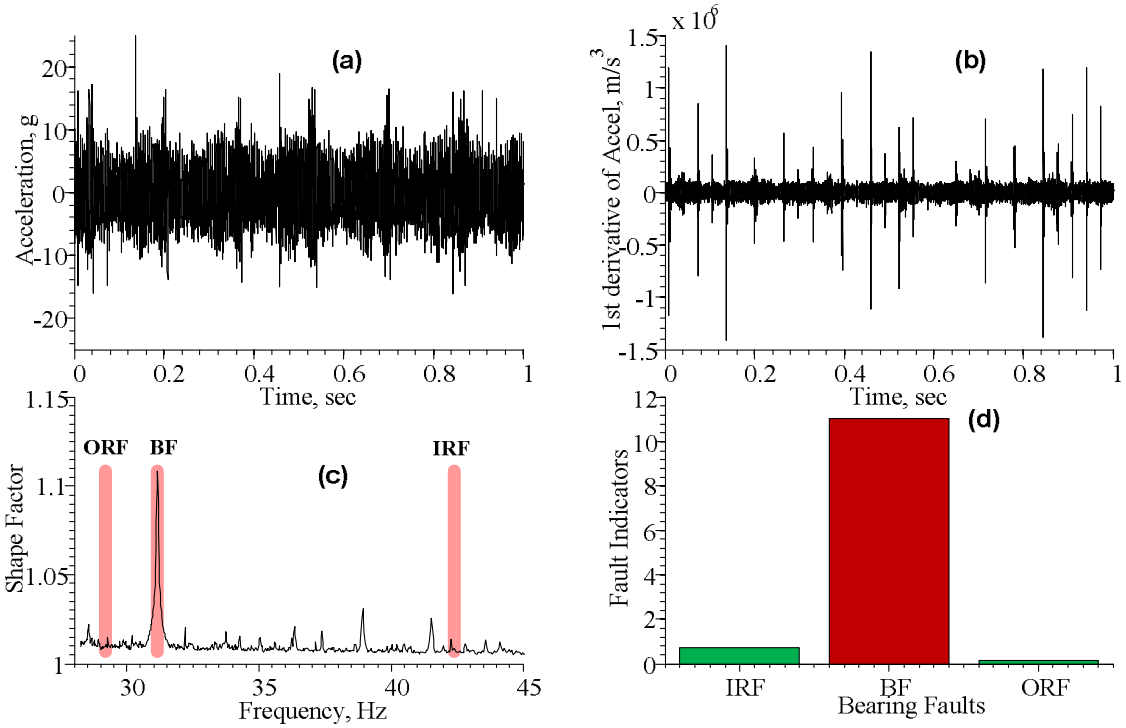


Figure 48 Detection of BF with Feature Plot technique: a) time waveform vibration signals, b) 1st derivative of vibration signals unmasked fault components as peaks indicating rough surface faults, c) shape factor feature plots of 1st derivative of vibration signals, d) fault indicators showing BF

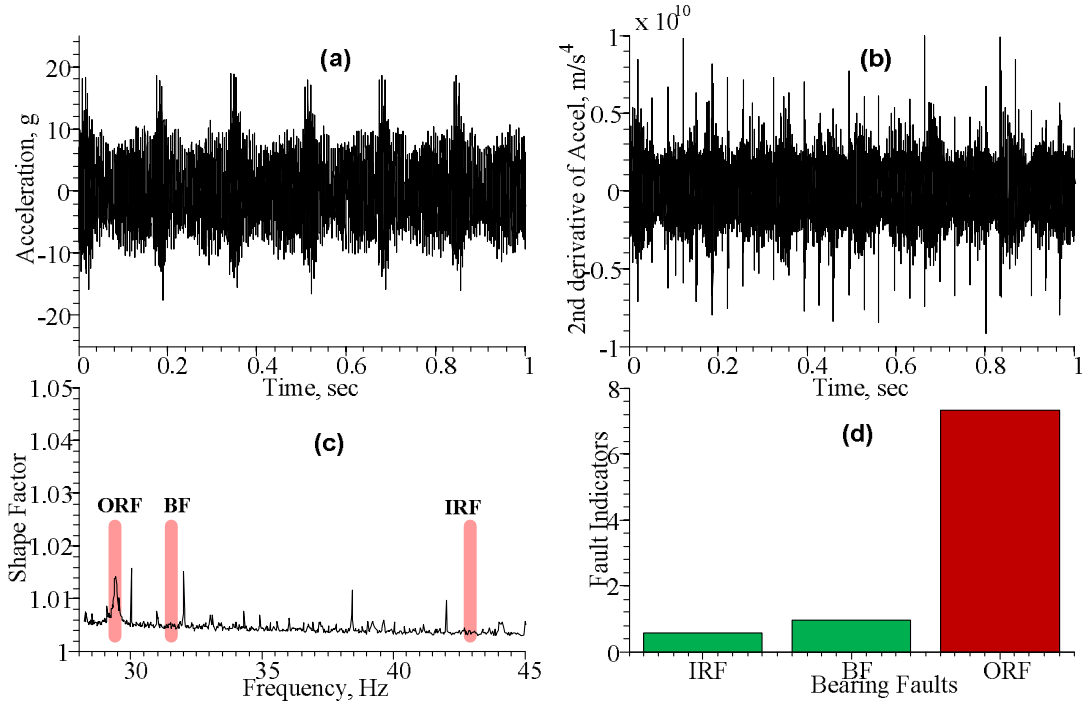


Figure 49 Detection of ORF with Feature Plot technique: a) time waveform vibration signals, b) 2nd derivative of vibration signals unmasked fault components as peaks indicating rough surface faults, c) shape factor feature plots of 2nd derivative of vibration signals, d) fault indicators indicating ORF

The performance of the feature plot technique with other time features such as skewness, Kurtosis, RMS, peak value, crest factor, impulse factor, and absolute mean deviation was also investigated. Fault indicators for each case were obtained and shown in Figure 50(a-c). For all cases, feature plot technique successfully detects and isolates bearing rough surface faults on inner race, balls, and outer race. Note that the first derivative of acceleration signals was used for IRF and BF and the second derivative of the acceleration was used for ORF.

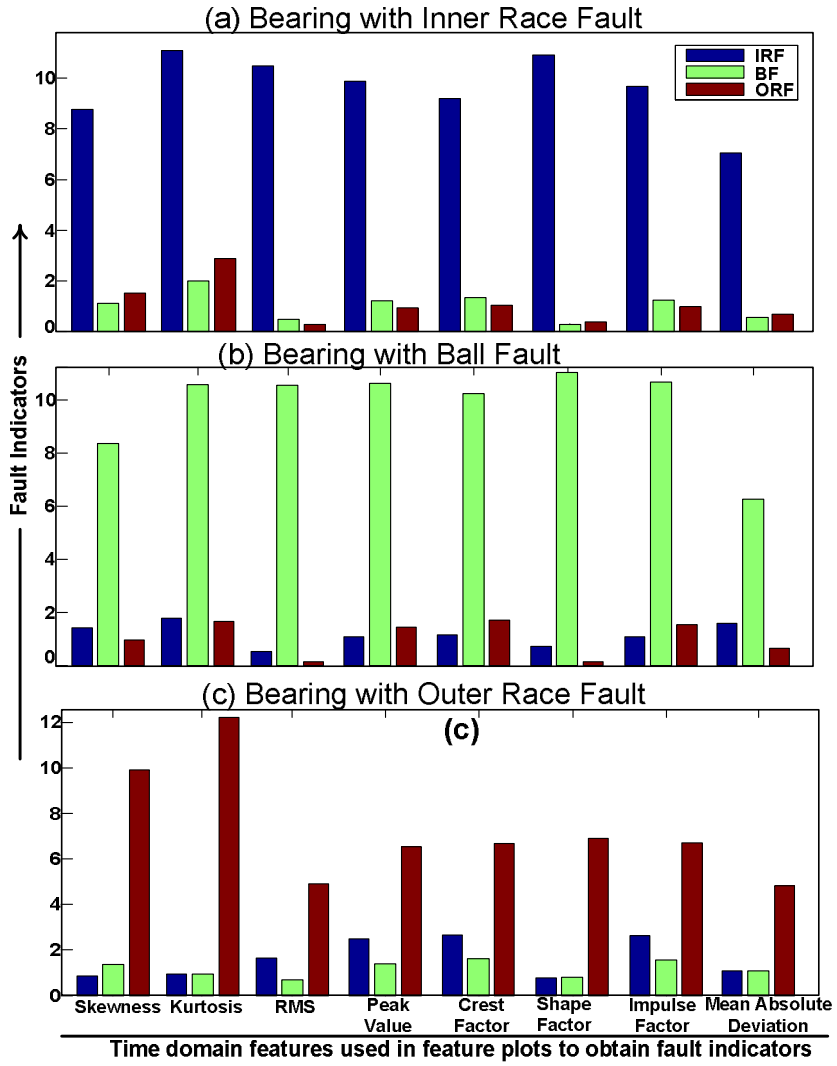


Figure 50 Fault indicators obtained from feature plots using different time domain features detect (a) inner race fault, (b) ball fault and (c) outer race fault from vibration measurements. Here, faults are rough surfaces on elements that are not severe damages.

## 4.6 SUMMARY AND CONCLUSIONS

A new signal processing technique, called feature plot, based on time feature extraction of variable window averaging, was developed for machine diagnostics. The

signal processing algorithm was formulated and illustrated with a simple example using sinusoidal functions. Time feature plots and frequency feature were constructed. Fault indicators were obtained from peaks of feature plots in fault regions. Feature plot technique was applied to rolling element bearings with localized faults and with rough surface faults. Time and frequency feature plots were constructed from vibration signals of healthy and faulty bearings, and fault indicators representing type and severity of the faults were obtained from residual feature plots. 28 sets of bearing vibration measurements with localized faults: Inner Race Faults (IRF), Ball Faults (BF), Outer Race Faults (ORF), and Combined Faults (CF) were tested. Experiments included vibration signals measured in both vertical and horizontal directions with high and low sampling frequencies. For each case, fault indicators were obtained and the ability of the developed diagnostic technique to detect and isolate bearing faults was demonstrated. Also, rough surface faults that generate minimum noise carried by the other signals in the machine were tested experimentally. First and second derivatives of acceleration were used to amplify and isolate fault signals from other signals in the case of rough surface faults. Faults were detected and isolated using the feature plot technique. The performance of feature plot technique with several time features such as skewness, kurtosis, RMS, peak value, crest factor, impulse factor and mean absolute deviation in diagnostics of rolling element bearings were investigates. Furthermore, the effectiveness of feature plots when only a short segment of data is available was presented, and results were compared with power spectrum density technique.

Results show the effectiveness of feature plots in diagnostics of rolling element bearings. The proposed diagnostic algorithm has the potential to be applicable to other dynamic systems such as gearbox. Fault regions at the first harmonics of fault components in feature plots provide rich search range to retrieve faults information and to

obtain fault indicators. Vertical axis in a feature plot has time information of the signal and the horizontal axis provide frequency information. Feature plots can be used for fault severity analysis since time features are directly related to the fault signals. Signal averaging makes the feature plot technique useful for faults with complicated behavior such as IRF and BF. Frequency feature plots contain high resolution in low frequencies, providing a useful diagnostic tool when signal samples are limited. Having multiple faults in bearings, vibration signals contain more sets of periodic impulses generating peaks in feature plots. Therefore, feature plots can also detect multiple bearings defects.

# Chapter 5

# Modeling and Observability Analysis of Induction Motors

## 5.1 INTRODUCTION

Implementing a practical model-based diagnostic system is challenging. Tasks such as detailed physics-based modeling, designing a proper sensor configuration to get enough information from the system, parameter tuning in highly nonlinear systems with efficient computational performance, and a reliable validation technique to evaluate the accuracy of the diagnosis are still much in demand. Bond graph modeling, an energy-based approach, with modularity that permits integrating additional modules to the system model [2], is a good modeling solution for model-based diagnostics.

Observability analysis is a major and crucial task in model-based diagnostics. If sensors do not provide enough information to track and distinguish states or parameters, the system is unobservable. In model-based diagnostics of unobservable systems, diagnosis may fail or the parameter tuning may converge to incorrect values, misleading the decision making unit. Therefore, observability analysis to determine the presence of sufficient information in measured signals for estimation of states and parameters is needed. Results will find effective combinations of sensors and parameters for model-based diagnostics, and provide a systematic procedure to select proper sensors and parameters. For sensor fault detection, an observability analysis can detect redundant sensors and evaluate levels of redundancy.

This chapter presents bond graph modeling, and nonlinear observability analysis for a 3-phase induction motor. The proposed techniques can be used for observability

analysis of any nonlinear system. First, a physics-based bond graph model of a three-phase induction motor is obtained and presented in vector bond graph forms. The model is simulated and validated with experiments. Then, nonlinear observability analysis based on Lie derivatives is introduced for state and parameter estimations. An observability index based on a singular value decomposition of the observability matrix determines the most and least observable configurations of measurements and parameters. A complex step Jacobian technique is introduced to improve computational speed of the observability analysis. Finally, the performance of the proposed observability analysis for the induction motor is studied through simulations.

## 5.2 SYSTEM MODELING

Ghosh's bond graph model of induction machines [86] employed a mutually perpendicular $\alpha$-$\beta$ model in a stationary reference frame [87] linked with a three phase current source inverter. Kim and Bryant [46] later partitioned the electrical, magnetic and mechanical domains of Ghosh and Bhadra's bond graph model of an induction motor.

Here, Kim's model is generalized for an induction motor with $n$ bars, and is posed in vector bond graphs as Figure 51 . The model consists of stator coil model (left) and rotor model (right), connected through a multiport C that represents the magnetic energy stored in the motor's air gap. The gyrator $\mathbf{GY:n}_{s\,(3\times3)}$ to the left transforms stator electrical fields into magnetic fields, inducing currents into rotor bars. Gyrator $\mathbf{GY:n}_{r\,(2\times2)}$ to the right transforms rotor electric fields into magnetic fields that interact with the stator magnetic fields through the two port **C** element with constitutive law:

$$\begin{bmatrix} \mathrm{M}_{s\alpha} \\ \mathrm{M}_{s\beta} \\ \mathrm{M}_{r\alpha} \\ \mathrm{M}_{r\beta} \end{bmatrix} = \left[\begin{array}{cc:cc} a & 0 & b & 0 \\ 0 & a & 0 & b \\ \hdashline b & 0 & c & 0 \\ 0 & b & 0 & c \end{array}\right] \begin{bmatrix} \varphi_{s\alpha} \\ \varphi_{s\beta} \\ \varphi_{r\alpha} \\ \varphi_{r\beta} \end{bmatrix}. \tag{1}$$

Equation (1) can be rewritten as

$$\begin{bmatrix} \mathbf{M}_{\mathbf{s}(2\times1)} \\ \mathbf{M}_{\mathbf{r}(2\times1)} \end{bmatrix}_{(4\times1)} = \begin{bmatrix} \mathbf{C}_{\mathbf{a}(2\times2)} & \mathbf{C}_{\mathbf{b}(2\times2)} \\ \mathbf{C}_{\mathbf{b}(2\times2)} & \mathbf{C}_{\mathbf{c}(2\times2)} \end{bmatrix}_{(4\times4)} \begin{bmatrix} \varphi_{\mathbf{s}(2\times1)} \\ \varphi_{\mathbf{r}(2\times1)} \end{bmatrix}_{(4\times1)}. \tag{2}$$

The notation $(i \times j)$ in the subscript indicates that the matrix has $i$ row and $j$ columns. Equation (2) relates magneto motive force **M** to flux **φ** via the reluctance matrix **C** with elements

$$\begin{aligned} a &= \frac{n_s^2\, L_r}{L_s L_r - L_m^2} \\ b &= \frac{-n_s n_r L_m}{L_s L_r - L_m^2} \\ c &= \frac{n_r^2 L_s}{L_s L_r - L_m^2} \end{aligned} \tag{3}$$

that depend on rotor and stator turns $n_r$ and $n_s$, self inductances $L_r$ and $L_s$ for rotor and stator, and mutual inductance $L_m$ between rotor and stator.

Numbers on bonds in the bond graph of Figure 51 indicate the vector dimension of bonds and associated elements. Transformer's and gyrator's moduli are matrices connecting bonds with different dimensions. Diagonal matrices $\mathbf{R}_{\mathrm{s}(3\times3)}$ and $\mathbf{R}_{\mathrm{m}(3\times3)}$ represent stator electrical and magnetic resistances, with diagonal terms corresponding to each of three phases. Diagonal matrix $\mathbf{R}_{\mathrm{r}(\mathrm{n}\times\mathrm{n})}$ contains rotor resistance information.

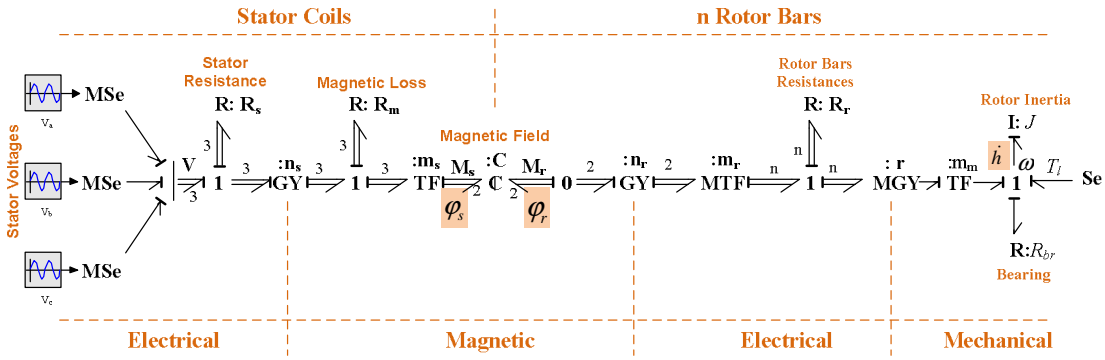


Figure 51 Vector bond graph model of squirrel cage induction motor

The dynamic states for this motor model include two stator magnetic fluxes $\varphi_{s(2\times1)}$, two rotor magnetic fluxes $\varphi_{r(2\times1)}$ and rotor angular momentum $h$. State equations extracted explicitly from the vector bond graph are

$$\dot{\boldsymbol{\varphi}}_{s(2\times1)} = \mathbf{m}_s^{T}\mathbf{n}_s^{-1}\left[\mathbf{V}-\mathbf{R}_s\mathbf{n}_s^{-1}\mathbf{m}_s\left(\mathbf{C}_a\boldsymbol{\varphi}_s+\mathbf{C}_b\boldsymbol{\varphi}_r\right)-\mathbf{R}_m^{-1}\mathbf{n}_s\mathbf{R}_s^{-1}\mathbf{V}+\mathbf{R}_m^{-1}\mathbf{m}_s\left(\mathbf{C}_a\boldsymbol{\varphi}_s+\mathbf{C}_b\boldsymbol{\varphi}_r\right)\right] \tag{4}$$

$$\dot{\boldsymbol{\varphi}}_{r(2\times1)} = \mathbf{n}_r^{-1}\mathbf{m}_r\mathbf{R}_r\mathbf{m}_r^{T}\left(\mathbf{C}_b\boldsymbol{\varphi}_s+\mathbf{C}_c\boldsymbol{\varphi}_r\right)-\mathbf{n}_r^{-1}\mathbf{m}_r\frac{h}{J\,m_m} \tag{5}$$

$$\dot{h} = -R_{br}\frac{h}{J}-\mathbf{r}^{T}\mathbf{m}_r^{T}\mathbf{n}_r^{-1}\left(\mathbf{C}_b\boldsymbol{\varphi}_s+\mathbf{C}_c\boldsymbol{\varphi}_r\right) \tag{6}$$

Vector $\mathbf{V_{3\times1}}$ represents the 3-phase input voltages, diagonal matrix $\mathbf{n}_{s(3\times3)}$ contains number of winding turns for each phase, $\mathbf{n}_{r(2\times2)}$ is an identity matrix, $m_m = p/2$ where $p$ is the number of poles, $R_{br}$ is bearing friction, $T_l$ is the mechanical load on the motor from the rest of the system, and

$$\mathbf{m}_{s\,(2\times3)} = \sqrt{\frac{2}{3}}\begin{bmatrix}\cos 0 & \cos 2\pi/3 & \cos 4\pi/3\\ \sin 0 & \sin 2\pi/3 & \sin 4\pi/3\end{bmatrix} \tag{7}$$

$$\mathbf{m}_{\mathbf{r}\,(2\times n)} = \sqrt{\frac{2}{n}}\begin{bmatrix} \cos\theta & \cos(\theta + 2\pi/n) & \dots & \cos[\theta + 2(k-1)\pi/n] \\ \sin\theta & \sin(\theta + 2\pi/n) & \dots & \sin[\theta + 2(k-1)\pi/n] \end{bmatrix} \quad ; \qquad (8)$$

$$k = 1,2,\dots,n$$

$$\mathbf{r}_{(1\times n)} = \sqrt{\frac{2}{n}}\begin{bmatrix} \varphi_{r\alpha} & -\varphi_{r\beta} \end{bmatrix}\begin{bmatrix} \cos\theta & \cos(\theta + 2\pi/n) & \dots & \cos[\theta + 2(k-1)\pi/n] \\ \sin\theta & \sin(\theta + 2\pi/n) & \dots & \sin[\theta + 2(k-1)\pi/n] \end{bmatrix} ; \qquad (9)$$

$$k = 1,\dots,n$$

Shaft angular position $\theta$ is another state with state equation $\dot{\theta} = h/(J\, m_m)$. Motor speed is $\omega = h/J$. The system of nonlinear state equations that describe the motor and measurements is

$$S_1: \begin{cases} \dot{\mathbf{X}}_{(6\times1)} = \mathbf{f}_{(6\times1)}(\mathbf{X}, \mathbf{u}, t) \\ \mathbf{Y}_{(m\times1)} = \mathbf{h}_{(m\times1)}(\mathbf{X}, \mathbf{u}, t) \end{cases} \qquad (10)$$

Here, state vector $\mathbf{X} = [\varphi_{s\alpha} \quad \varphi_{s\beta} \quad \varphi_{r\alpha} \quad \varphi_{r\beta} \quad h \quad \theta]$, the state function $\mathbf{f}$ is defined via Eqs. (4-6), and the input vector $\mathbf{u}_{(3\times1)} = \mathbf{V}$. Vector $\mathbf{Y}$ can have any of $i_1, i_2, i_3, \omega$ and $\theta$ as outputs, defined by observation function $\mathbf{h}$.

The vector bond graph model of Figure 51 clearly shows interactions between electrical, mechanical and magnetic domains. Bond graph elements represent physical components of the motor: **MSe** as voltage source, $\mathbf{R_s}$ and $\mathbf{R_m}$ as electrical and magnetic resistances of stator winding, multiport **C** as the magnetic energy stored in motor's air gap, $\mathbf{R_r}$ as rotor bar resistance, **I**: $J$ for rotor inertia, $R_{br}$ as bearing frictions, and **Se** as mechanical loads on the motor.

### 5.3 EXPERIMENTS AND SIMULATIONS OF THE INDUCTION MOTOR

The bond graph model of the induction motor (Table 8) with five states $\varphi_{s\alpha}, \varphi_{s\beta}, \varphi_{r\alpha}, \varphi_{r\beta}, h$ and with state equations (4-6) was simulated. Tests on a 3-phase induction motor (Marathon, 0.5 HP, 2 poles, 34 rotor bars) with no load were conducted. Currents were measured by Hall effect sensors and shaft speed was measured with an

encoder at sampling frequency of 76800 Hz. Figure 52 (a) compares simulated motor phase current $I_1$ and motor speed $\omega$ to measured experimental counterparts.

Table 8 Induction Motor specifications

| Parameter | Value |
|---|---|
| Number of rotor coil turns, $n_r$ | 1 |
| Number of stator winding turns, $n_s$ | 111 |
| Number of rotor bars, $n$ | 34 |
| Number of poles, $p$ | 2 |
| Stator coil resistance, $R_{s1}, \dots, R_{s3}$ [Ω] | 2.1 |
| Stator magnetic losses, $R_{m1}, \dots, R_{m3}$ [1/Ω] | 0.03539 |
| Rotor bar resistance, $R_{r1}, \dots, R_{r34}$ [Ω] | 0.8663 |
| Stator inductance, $L_s$, [H] | 1.02938 |
| Rotor inductance, $L_r$, [H] | 0.9834 |
| Mutual inductance, $L_m$, [H] | 1.00130 |
| Bearing friction, $R_{br}$, [N.s/m] | 0.0085 |
| Moment of inertia, $J$, [N. m$^2$] | 0.0115 |

The three phase voltage input $\mathbf{V}(t)$ has components

$v_i = 167\sin(2\pi ft + i2\pi/3)$ ; $i = 1,2,3$ & $f = 60$Hz

The motor started with initial values of zero for all states. The AC input current of frequency 60 Hz had amplitude that increased during start up, but diminished at steady state while the motor speed reached synchronous speed of 3501 RPM. Since the encoder was connected to the motor through a long shaft with a helical beam coupling, high frequency rotational vibrations of the coupling were observed in the motor speed signals in Figure 52 (a).

Free acceleration torque-speed curve in Figure 52 (b) shows the electromagnetic torque of the motor with no load. The motor was subjected to pulsating torques during startup. At synchronous speed the motor had zero magnetic torque.

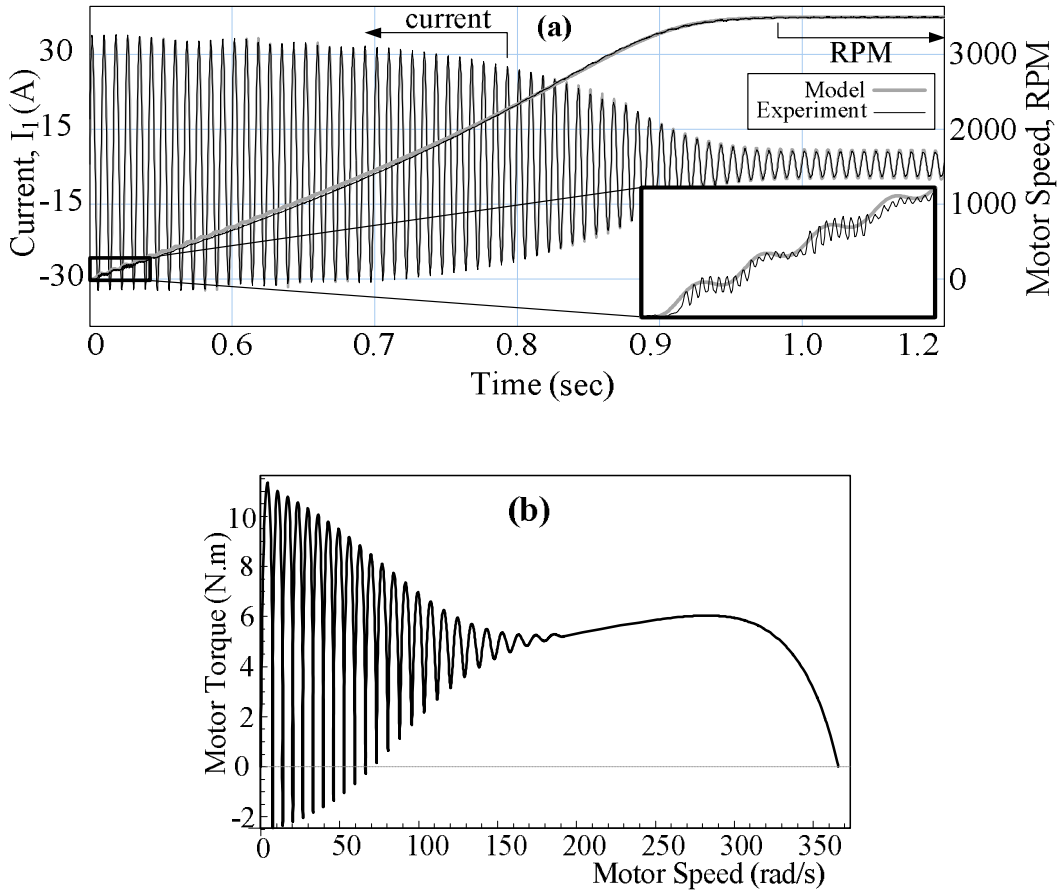


Figure 52 Simulations and measurements of the 3-phase induction motor: (a) simulated motor speed $\omega$ and current $I_1$ compared with measurements, (b) simulated free acceleration torque-speed curve.

## 5.4 OBSERVABILITY ANALYSIS

A system is observable if all states can be uniquely estimated, given a finite set of observations. There are two types of observability problems:

Type 1: Observation data has (a) no information (unobservable) or (b) very little information (nearly unobservable) of a state being estimated.

Type 2: Two or more states can change with (a) no effect or (b) very little effect on observations

In type 1, observability issues arise from lack of information, and in type 2, from inseparable information when states are dependent and cannot be distinguished using the observation data.

Observability of a linear system,

$$S_2: \begin{cases} \dot{\mathbf{X}}_{(n\times 1)} = \mathbf{AX} + \mathbf{Bu} \\ \mathbf{Y}_{(m\times 1)} = \mathbf{CX} + \mathbf{Du} \end{cases} \tag{11}$$

is determined via the rank of the observability matrix

$$\mathbf{O}_{(mn\times n)} = \begin{pmatrix} \mathbf{C} \\ \mathbf{CA} \\ \vdots \\ \mathbf{CA}^{n-1} \end{pmatrix} \tag{12}$$

with $mn$ rows and $n$ columns. A system is observable if matrix $\mathbf{O}$ has full rank [88]. Observability issue type 1 occurs when a column of matrix $\mathbf{O}$ in Eq. (12) is zero or nearly zero. Observability issue type 2 occurs when two or more columns of the observability matrix Eq. (12) are linearly dependent or nearly dependent.

For nonlinear systems, a local observability approach based on the Lie derivative [89] is defined. Given the non-linear system $S_3$ with $n$ states, $m$ outputs and $r$ inputs,

$$S_3: \begin{cases} \dot{\mathbf{X}}_{(\mathrm{n}\times 1)} = \mathbf{f}\left(\mathbf{X}, \mathbf{u}_{(r\times 1)}, t\right) \\ \mathbf{Y}_{(\mathrm{m}\times 1)} = \mathbf{h}\left(\mathbf{X}, \mathbf{u}_{(r\times 1)}, t\right) \end{cases}, \tag{13}$$

the Lie derivative of $\mathbf{h}_{(m\times 1)}$ with respect to $\mathbf{f}_{(n\times 1)}$, which is a $m \times 1$ vector, is defined as

$$L_{\mathrm{f}}\mathbf{h} = \frac{\partial \mathbf{h}}{\partial \mathbf{x}} \bullet \mathbf{f} \tag{14}$$

where • denotes the dot product operation. By definition, $L_{\mathbf{f}}^{0}\mathbf{h} = \mathbf{h}$. Higher order Lie derivatives are given by

$$L_{\mathbf{f}}^{n}\mathbf{h} = L_{\mathbf{f}}\left(L_{\mathbf{f}}^{n-1}\mathbf{h}\right) = L_{\mathbf{f}}\left(L_{\mathbf{f}}\left(L_{\mathbf{f}}^{n-2}\mathbf{h}\right)\right). \tag{15}$$

The observability matrix $\mathbf{O}_{(mn\times n)}$ is defined as the Jacobian of the Lie derivative vector $\mathbf{G}$ as

$$\mathbf{O}_{(mn\times n)} = \frac{\partial \mathbf{G}}{\partial \mathbf{X}} = \begin{bmatrix} \frac{\partial L_{\mathbf{f}}^{0}\mathbf{h}}{\partial x_1} & \cdots & \frac{\partial L_{\mathbf{f}}^{0}\mathbf{h}}{\partial x_n} \\ \vdots & \ddots & \vdots \\ \frac{\partial L_{\mathbf{f}}^{n-1}\mathbf{h}}{\partial x_1} & \cdots & \frac{\partial L_{\mathbf{f}}^{n-1}\mathbf{h}}{\partial x_n} \end{bmatrix}; \text{ where } \mathbf{G}_{(mn\times 1)} = \begin{bmatrix} L_{\mathbf{f}}^{0}\mathbf{h} \\ \vdots \\ L_{\mathbf{f}}^{n-1}\mathbf{h} \end{bmatrix} \tag{16}$$

If the system (13) is linear and can be expressed by (11), then Eq. (16) simplifies to Eq. (12). The nonlinear system $S_3$ locally at $(\mathbf{X}_0, \mathbf{u}_0, t_0)$ is observable if the rank of the observability matrix $\mathbf{O}$ is $n$. The rank test of the observability matrix investigates type 1a and 2a observability issues. However, in highly nonlinear complex systems, the system might be theoretically observable with little information of states (type 1b) or with nearly inseparable states (type 2b). In this case, parameter estimation might fail in practice. Therefore, an index should be defined to evaluate the level of observability.

## 5.5 OBSERVABILITY INDEX

Singular value decomposition (SVD) operation produces a basis for the row and column space of the matrix and an indication of the rank of the matrix. Given an $m \times n$ matrix $\mathbf{A}$, the singular value decomposition of $\mathbf{A}$ is

$$\mathbf{A} = \mathbf{USV}^{\mathbf{T}}$$

where $\mathbf{U}$ is a unitary matrix of size $m \times m$, $\mathbf{S}$ is an rectangular diagonal $m \times n$ matrix, in which the real non-negative diagonal entries are sorted in descending order, and $\mathbf{V}$ is an $n \times n$ unitary matrix. The columns of $\mathbf{U}$ and $\mathbf{V}$ are called the left and right singular vectors, respectively, and the diagonal elements of $\mathbf{S}$ are called singular values. The term "singular value" relates to the distance between a matrix and the set of singular matrices. SVD can be used for rank determination. The rank of a matrix is equal to the number of non-zero singular values.

A singular value decomposition [90] on the observability matrix $\mathbf{O}_{(mn\times n)}$ gives

$$\mathbf{O} = \mathbf{USV^T} \tag{17}$$

where the rectangular diagonal matrix $\mathbf{S} \in \Re^{mn\times n}$ contains $n$ singular values $\sigma_i$ as diagonal entries, and $\mathbf{U} \in \Re^{mn\times mn}$ and $\mathbf{V} \in \Re^{n\times n}$ are unitary matrices. The rank of matrix $\mathbf{S}$ can be used for an observability test instead of the rank of matrix $\mathbf{O}$. Any zero diagonal element in $\mathbf{S}$ indicates a source of unobservability. Furthermore, the magnitude of each singular value indicates observability. If the system is observable, the matrix $\mathbf{S}$ contains $n$ nonzero elements. In a nearly unobservable system, the matrix $\mathbf{S}$ contains relatively very small diagonal elements. The condition number,

$$C = \frac{\sigma_{max}}{\sigma_{min}} \tag{18}$$

defined as the ratio of the largest to smallest singular value of the diagonal matrix $\mathbf{S}$ can be the observability index for the system.

Larger condition numbers correspond to less observable systems. Each state corresponding to each singular value can be found from the companion matrix $\mathbf{V}^{\mathrm{T}}$. The column of $\mathbf{V}$ that corresponds to the largest singular value $\sigma_{max}$ provides the most

observable linear combination of states. The state that corresponds to the largest number in each column is the most observable state.

## 5.6 IDENTIFIABILITY

Parameter tuning in model-based diagnostics involves identification of parameters. Similar to observability, there are two types of identifiability issues: Type 1) no information or very little information of a parameter in observation data, Type 2) inseparable or hardly separable information. Here, parameter augmentation technique investigates the identifiability of the system. Investigated parameters $p_1, p_2, \dots, p_k$ are grouped as a vector $[p_1 \quad p_2 \quad \cdots \quad p_k]^{\mathrm{T}}$ and augmented onto the state vector. The dynamic equations are rewritten as

$$\mathrm{S}_4: \begin{cases} \dot{\mathbf{X}}_{((n+k)\times 1)} = \tilde{\mathbf{f}}\left(\mathbf{X}, \mathbf{u}_{(r\times 1)}, t\right) \\ \mathbf{Y}_{(m\times 1)} = \mathbf{h}\left(\mathbf{X}, \mathbf{u}_{(r\times 1)}, t\right) \end{cases}; \tag{19}$$

where $\mathbf{X}_{((n+k)\times 1)} = \begin{pmatrix} \mathbf{X} \\ p_1 \\ \vdots \\ p_k \end{pmatrix}$ and $\tilde{\mathbf{f}}_{((\mathrm{n}+\mathrm{k})\times 1)} = \begin{pmatrix} \mathbf{f} \\ 0 \\ \vdots \\ 0 \end{pmatrix}$.

In the nonlinear state equation $\tilde{\mathbf{f}}$ in Eq. (2), entries $\tilde{f}_{n+1}: \tilde{f}_{n+k}$ corresponding to the time derivatives of the parameters are zero, making $p_1, p_2, \dots, p_k$ constant. The nonlinear identifiability of system $\mathrm{S}_4$ for the augmented parameters is processed similar to the nonlinear observability of system $\mathbf{S_3}$ in Eq. (13). In this case, the observability refers to the ability to gather information about all states and parameters of the system from measurements $\mathbf{Y}_{(m\times 1)}$ and inputs $\mathbf{u}_{(r\times 1)}$.

Here, a general procedure for observability analysis of any nonlinear system is proposed:

1) Formulate the nonlinear dynamic equations (13) of the system, with measurements **Y**.
2) Augment into the dynamic equations the parameters corresponding to the faults.
3) Construct the observability matrix **O** from augmented nonlinear dynamic equations (19).
4) Perform a singular value decomposition on **O,** determine the condition number (18) through the trajectory to indicate the observability index of the system.
5) The companion matrix **V** indicates the most and the least observable states
6) The source of the observability issue is found from the least observable term.
7) Modify the configuration of sensors/parameters to improve the system observability and repeat steps 2 to 7.

## 5.7 COMPLEX STEP JACOBIAN (CSJ)

Nonlinear observability analysis based on the analytical model requires calculation of the Jacobian matrix along the trajectory, e.g., Eq. (16). For a highly nonlinear system with $n$ states, $k$ parameters and $m$ observations, the Lie derivative vector **G** contains $m(n+k)$ highly nonlinear functions. For most systems of practical interest to diagnostics, $n$ and $k$ are large and the analytical Jacobian cannot be obtained easily. Also, in extended Kalman filters, the Jacobian matrices **A** and **H** need to be calculated during the estimation. Numerical techniques to calculate Jacobian of a matrix require numerical differentiation. To differentiate a real function $\mathrm{f}(x)$, change of the function $\Delta\mathrm{f}$ for a small change in the variable $\Delta x$ is obtained. In practice, $\Delta x$ can be different based on the scale of the variable $x$. In order to find a differentiation technique independent of the scale of $x$, differentiation can be operated in complex domain. Here,

the complex step Jacobian technique, which can be efficiently implemented in any computational program, is introduced based on complex step derivatives.

Given a real function f(x), which is continuous, analytic, and differentiable, a derivative approximation can be obtained by complex perturbation of the variable in the complex domain as [91]

$$\frac{\partial \mathrm{f}}{\partial x} \approx \frac{\mathrm{Im}[\mathrm{f}(x + \mathrm{i}h)]}{h}. \tag{20}$$

Here, i is the imaginary unit ($\mathrm{i} = \sqrt{-1}$), and small step size $h$ can be selected as the smallest distinguishable machine-precision number ($\approx 10^{-16}$). For a vector function $\mathbf{f}(\mathbf{X})$, with variables vector $\mathbf{X}$, the Jacobian matrix $\mathbf{J}$ can be approximated as

$$\mathbf{J}_{ij} = \frac{\partial \mathbf{f}_i}{\partial \mathbf{X}_j} \approx \frac{\mathrm{Im}\left[\mathbf{f}_i\left(\widetilde{\mathbf{X}}^j\right)\right]}{h} \tag{21}$$

where $[\widetilde{\mathbf{X}}^1 \quad ... \quad \widetilde{\mathbf{X}}^n] = [\mathbf{X} \quad ... \quad \mathbf{X}] + \mathrm{i}h\mathbf{I}$ ; $\mathbf{I}$: is the identity matrix

Therefore, the observability matrix $\mathbf{O}$ is approximated locally at $\mathrm{t}_0$ using the complex step Jacobian as

$$\mathbf{O}_{ij} \approx \frac{\mathrm{Im}\left[\mathbf{G}_i\left(\widetilde{\mathbf{X}}_0^j, \mathbf{u}_0, t_0\right)\right]}{h} \tag{22}$$

with $[\widetilde{\mathbf{X}}_0^1 \quad ... \quad \widetilde{\mathbf{X}}_0^n] = \left[\mathbf{X}_0 \quad ... \quad \mathbf{X}_0\right] + \mathrm{i}h\mathbf{I}$. The same technique will be used in the extended Kalman filter algorithm to obtain Jacobian matrices **A** and **H**.

## 5.8 RESULTS AND DISCUSSIONS

### 5.8.1 Complex Step Jacobian (CSJ)

The performance of the Complex Step Jacobian (CSJ) in observability analysis of the induction motor for state estimation from observations $I_1, I_2, I_3$ is studied.

Observability matrix was constructed using both analytical Jacobian and Complex Step Jacobian techniques and singular values of the observability matrix associated with states $\varphi_{s\alpha}, \varphi_{s\beta}, \varphi_{r\alpha}, \varphi_{r\beta}$ along the trajectory for 1.2 seconds with increments of 0.01 seconds are shown in Figure 53(a-d) for each state with the corresponding error signals. The 18.8 hours computational time for the analytical Jacobian was reduced to 3.1 hours using the complex step Jacobian technique. As seen in all four cases of Figure 53, errors are less than $10^{-7}\%$ . This article uses the complex step Jacobian technique in observability analysis and in extended Kalman filters to improve computational performance without losing much accuracy.

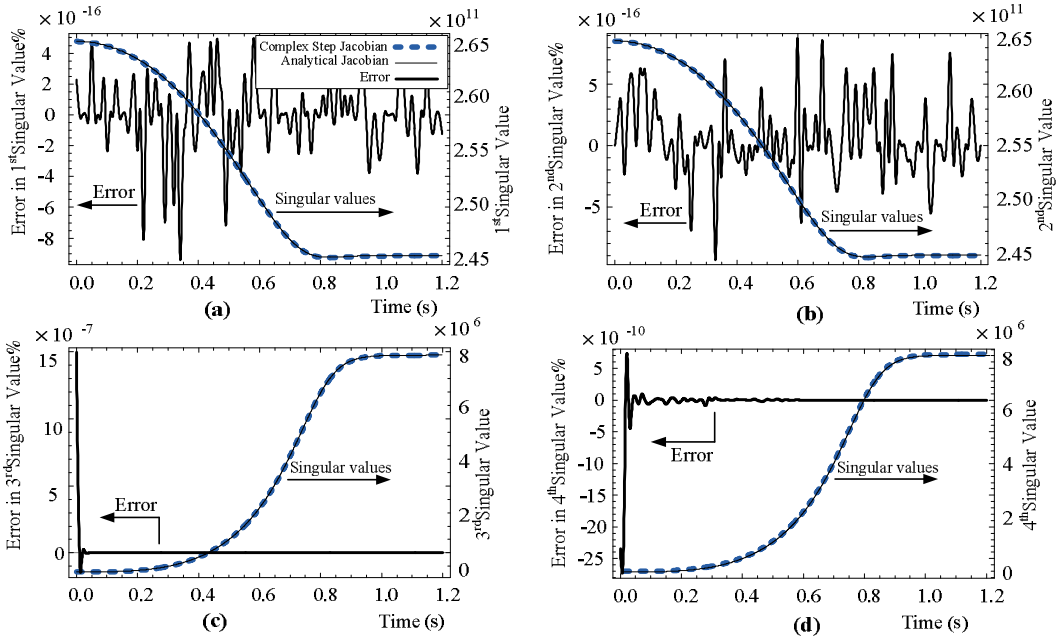


Figure 53 Performance of Complex Step Jacobian (CSJ) in observability analysis for state estimation of the induction motor. Computational time: 18.8 hours using analytical Jacobian, 3.1 hours using CSJ.

### 5.8.2 Observability Analysis

For an induction motors, measurements can be currents $I_1, I_2, I_3$ from Hall effect sensors, rotor angular positions $\theta$ and speed $\omega$ from encoders. For the induction motor model (Table 8) with six states $(\varphi_{s\alpha}, \varphi_{s\beta}, \varphi_{r\alpha}, \varphi_{r\beta}, h, \theta)$, an observability analysis for state estimation with different measurement configurations (Table 9) wherein type and number of measurements were varied, was conducted in the computational software Mathematica 6.0 . For each case, the Lie derivative vector $\mathbf{G}$ was obtained analytically. The model was numerically simulated for 1.2 seconds, with zero initial values for states. For the whole trajectory, the observability matrix $\mathbf{O}$ was estimated numerically using the Complex Step Jacobian. Singular values of the matrix $\mathbf{O}$ were found, and the observability index $C$ was determined via (18).

Table 9 Different combinations of measurements for observability analysis

| Case | Measurements |
|---|---|
| 1 | $I_1, \omega$ |
| 2 | $I_1, \theta$ |
| 3 | $I_1, I_2, I_3$ |
| 4 | $I_1, I_2, I_3, \omega$ |
| 5 | $I_1, \theta, \omega$ |
| 6 | $I_1, I_2, I_3, \theta$ |
| 7 | $I_1, I_2, \theta, \omega$ |
| 8 | $I_1, I_2, I_3, \theta, \omega$ |

In the transient operating range, when the motor speeds up as Figure 54(a), the rank of the observability matrix $\mathbf{O}$ is plotted versus time in Figure 54(b), for each case of motor observations. In the fully observable cases (4, 5, 6, 7, 8), the observability matrix $\mathbf{O}$ keeps full rank (6) during the entire trajectory. Case 1 with observations $I_1, \theta$ always has rank 5, and is not observable. Cases 2 and 3 with observations $I_1, \theta$ and $I_1, I_2, I_3$ are

unstable (rank fluctuates between 6 and 5), and consequently for $t < 0.2\,sec$ the rank oscillates. At steady state, cases 2 and 3 have full rank and are observable, i.e., in theory, states can be estimated and observed from measurements. However, in practice measurement noise, information loss during measurements, modeling error and uncertainties can make an observable system unobservable, if the system is very close to an unobservable zone (nearly observable). Singular values of the observability matrix with observability index provide more information on this issue.

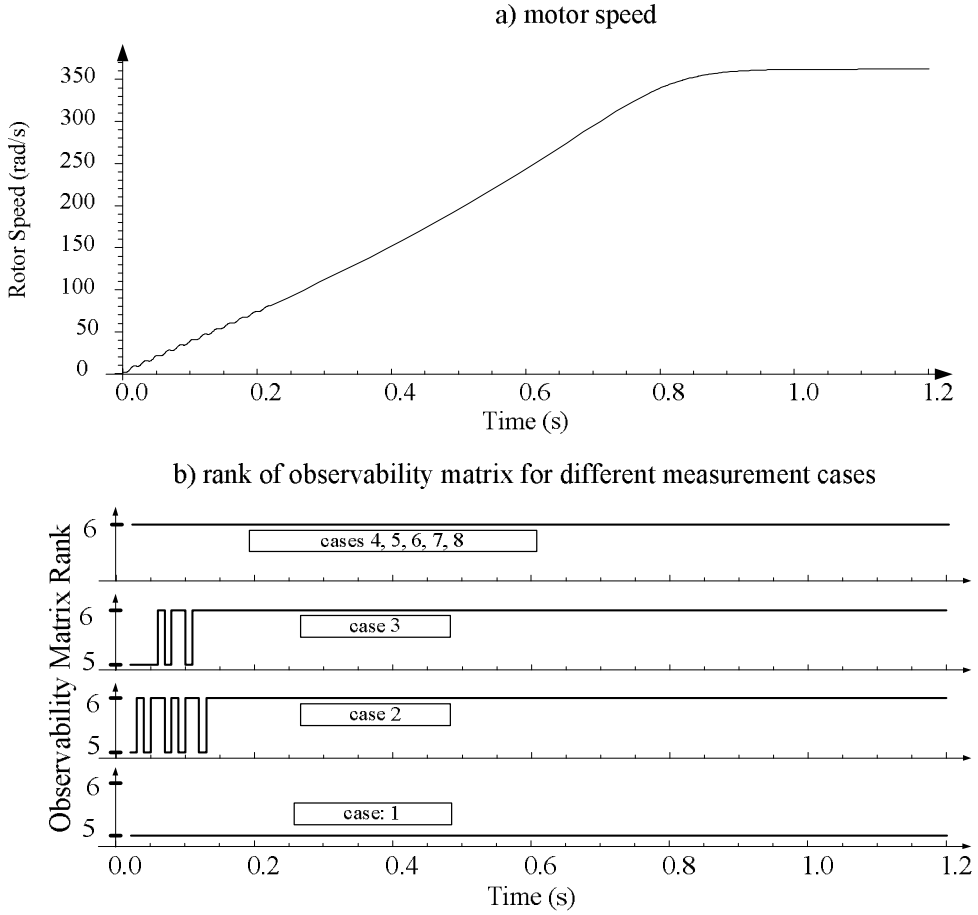


Figure 54 Rank of observability matrix in state estimation of the induction motor with different measurements during motor start-up

Observability indexes $C$ are plotted in Figure 55 for each case of measurements. For the unobservable case 1 with $\text{rank}(\mathbf{O}) = \mathbf{5}$, the observability index goes to $\infty$, since one of the singular values $\sigma_i$ is zero. For each system, a limit can be set for $C$ to define a fully observable system. However, a comparative analysis of observability indexes, more pertinent to model-based diagnostics, provides useful information for the sensor arrangement design, parameter selection, and sensor redundancy analysis. Proceeding from case 2 to 3, in Figure 55(a) the observability index $C$ drops significantly, suggesting that state estimation from three current sensors (case 3) is more effective than one current sensor and an encoder. Including a speed measurement with the current measurements (case 4) does not change much the observability index. But, measurements of $\theta$ and three currents (case 6) improves the observability of the system significantly, see Figure 55(b). Cases 7 and 8 have similar observability indices, suggesting the current sensor redundancy for the state estimation. In diagnostics of induction motors for stator faults, this redundancy is required to isolate faults in specific phases.

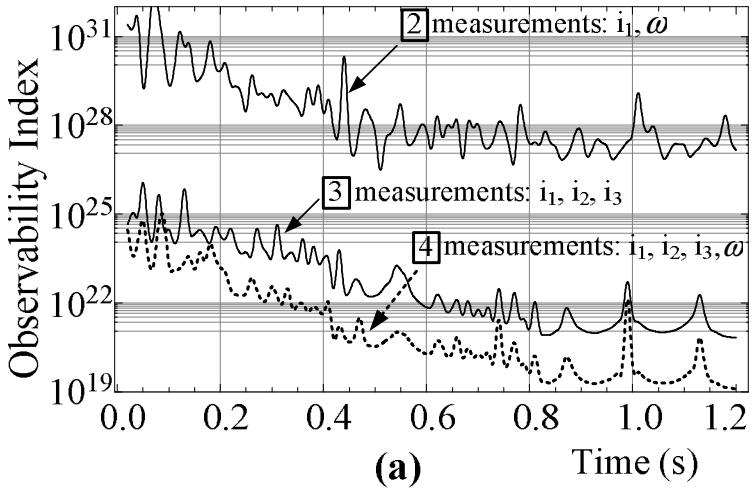

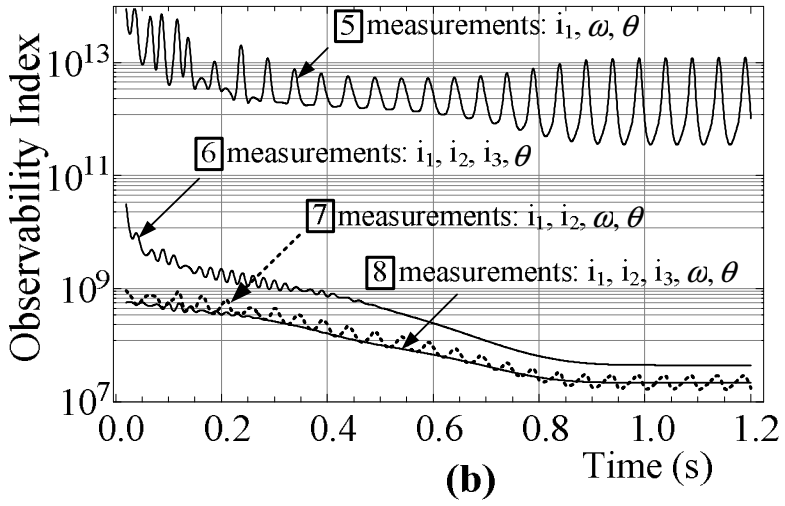


Figure 55 Observability indexes in full state estimation of the induction motor with different measurements

Observability indexes for parameter tuning of the induction motor from observations $I_1, I_2, I_3, \omega, \theta$ (case 8) are shown in Figure 56 for different parameters. For each case, the parameter was augmented to the state vector and the observability index estimated. The most observable case (smallest index) estimates states only. The observability index increases as parameters are included with the states. The system is less observable during the time of transient response and more observable at steady state ($t > 0.9$). However, lack of observability during the time of system transient may not be a major issue, since the model-based diagnostic system is designed for steady running of machines. Figure 56 shows the system observable for each case, and most observable for tuning $R_m$ and $R_s$. This technique of observability index with singular values can investigate observability of any nonlinear system, whether for tuning parameters individually or together. Different combinations of measurements and parameters might have different observability indices. The goal is to find an optimum design for model-

based diagnostics, via selections of different measurements, inputs and parameters, with enough sensor redundancy.

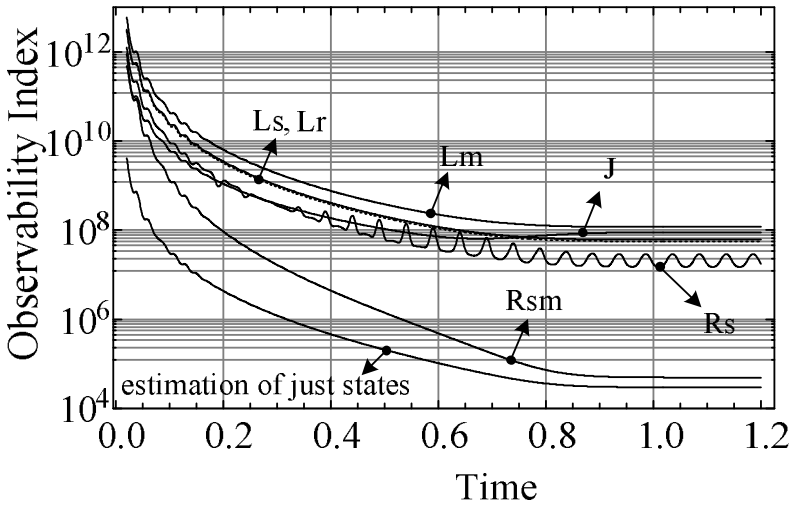


Figure 56 Observability indices of the induction motor, for estimation of different parameters

Singular values determine the observability index. Singular vectors in the companion matrix **V** obtained from singular value decomposition of the observability matrix **O**, determine the observability of each state and parameter. The column of **V** corresponding to the largest singular value provides the most observable linear combination of states, and the state corresponding to the largest number in each column of **V** is the most observable state. Here, for estimation of five states $\mathbf{X} = \left(\varphi_{s\alpha},\ \varphi_{s\beta},\ \varphi_{r\alpha},\ \varphi_{r\beta}, h\right)^{\mathrm{T}}$ of the induction motor using three current measurements (case 3), singular vectors at $t = 1.2$ (sec ) are shown in Eq. (23) with the element largest in absolute value in each column in bold font.

$$\mathbf{X} = \begin{pmatrix} \varphi_{s\alpha} \\ \varphi_{s\beta} \\ \varphi_{r\alpha} \\ \varphi_{r\beta} \\ h \end{pmatrix}; \quad \mathbf{V} = \begin{pmatrix} \mathbf{-0.86} & -0.51 & 0.015 & -0.02 & -0.0043 \\ 0.51 & \mathbf{-0.86} & 0.043 & 0.000085 & -0.0055 \\ -0.011 & -0.025 & -0.3 & \mathbf{0.75} & 0.6 \\ 0.0096 & -0.038 & \mathbf{-0.92} & -0.064 & -0.38 \\ 0.013 & -0.0091 & -0.25 & -0.66 & \mathbf{0.71} \end{pmatrix} \tag{23}$$

Columns are in descending order of corresponding singular values from left to right. This largest element in each column is associated with the most observable state. Therefore, the order of states from the most observable to the least observable is $\varphi_{s\alpha} > \varphi_{s\beta} > \varphi_{r\beta} > \varphi_{r\alpha} > h$.

## 5.9 SUMMARY AND CONCLUSIONS

A detailed bond graph model of a three-phase induction motor was obtained and presented in vector form. The model was validated with experiments. A nonlinear observability analysis using Lie derivatives for the application of model-based diagnostics was introduced. Singular value decompositions were performed on the observability matrix and an observability index were defined. Using the proposed observability index, the observability of the induction motor for several configurations of measurements and parameters were studied. Results of the observability analysis on the induction motor can be used to design a sensor configuration with enough redundancy for detection of system faults or sensor faults. Also, a computational algorithm for Jacobian matrix calculation in observability analysis using the complex step derivatives was introduced. Simulations suggest that complex step Jacobian (CSJ) technique highly improves computational performance of observability analysis.

# Chapter 6

# Parameter Tuning and Model-Based Diagnostics of Induction Motor

## 6.1 INTRODUCTION

Faults and degradation in machines are related to change of states and/or parameters. A model-based diagnostic system consisting of physics-based model, parameter tuning module, and decision making unit shown in Figure 57 tracks states and parameters of the system to detect degradation or to predict the failure of components [44]. Observations **Y** measured by sensors are compared to the corresponding outputs $\hat{\mathbf{Y}}$ of the model. The difference generates the residual **r**. The parameter tuning module minimizes the residuals by tuning the states **X** and parameters **P** of the model. The decision making and fault assessment units detect or predict the occurrence of faults by interpreting changes of parameters.

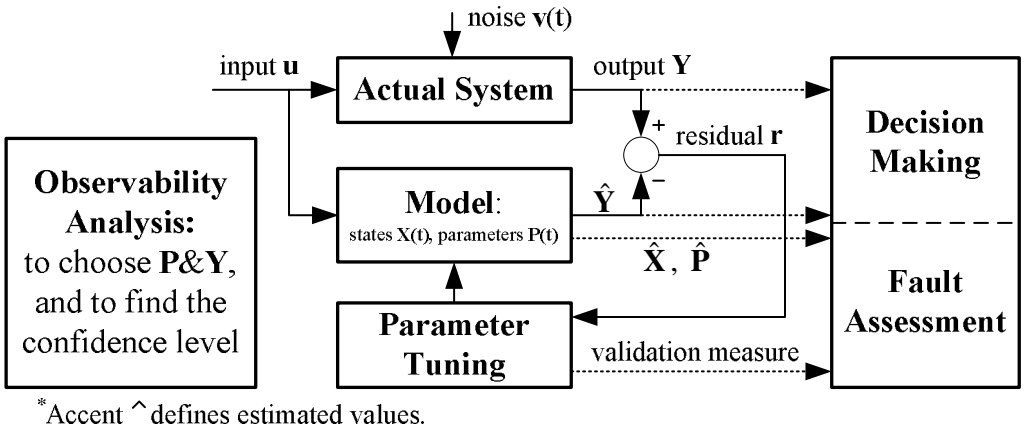


Figure 57 General Structure of the Model-Based Diagnostics

Parameter tuning in model-based diagnostics monitors and tracks the model's parameters by minimizing measurement residuals. For a healthy system, values of some parameters can be derived analytically or directly measured. Other parameters which cannot be measured physically or estimated analytically require parameter estimation to determine initial values of parameters. Parameter tuning can be implemented in batch or sequential algorithms. Batch estimation techniques process all observations at the same time, to solve for parameters. Sequential techniques suitable for on-time applications process one observation at each time. Here, extended Kalman filter (EKF) as a sequential estimation technique will be used for parameter tuning.

A continuous-discrete extended Kalman filter with dynamic process noise was developed for parameter tuning. The proposed complex step Jacobian technique improved the computational performance of the EKF. The model-based diagnostics framework was applied to the induction motor, for parameter tuning and fault detection. The EKF also estimated bearing friction and motor mechanical loads. Simulation results will be presented for diagnostics of the motor with stator and rotor faults, from measurements of currents, voltages and speed. Finally, simulations of the performance of the dynamic process noise in EKF for detection of stator faults in the induction motor will be presented.

## 6.2 CONTINUOUS-DISCRETE EXTENDED KALMAN FILTER

Extended Kalman Filter (EKF), a minimum mean-square error estimation technique for nonlinear systems, processes sensor observations with sensor noise to estimate states, using a model of the system. EKF can be implemented in discrete or continuous forms. Most physical systems are formulated as continuous time models,

whereas discrete-time measurements are collected from a real machine. A continuous-discrete extended Kalman filter was designed here for parameter estimation of the induction motor.

A nonlinear system with continuous time dynamic equations and discrete measurement equations is given by

$$S_3: \begin{cases} \dot{\mathbf{X}} = \mathbf{f}(\mathbf{X}(t), \mathbf{u}(t), t) + \mathbf{w}(t) & ; \quad \mathbf{w}(t) \sim N(0, \mathbf{Q}) \\ \mathbf{Y}_k = \mathbf{h}(\mathbf{X}_k, \mathbf{u}_k, \mathrm{t}_k) + \mathbf{v}_k & ; \quad \mathbf{v}_k \sim N(0, \mathbf{R}) \end{cases}. \tag{1}$$

Here $\mathbf{X} \in \Re^{n\times 1}$ is the $n \times 1$ dimension state vector, $\mathbf{u} \in \Re^{r\times 1}$ is the input vector, $\mathbf{Y}_k \in \Re^{m\times 1}$ is the $k^{th}$ observation vector, and $\mathbf{w}(t) \in \Re^{n\times 1}$ and $\mathbf{v}_k \in \Re^{m\times 1}$ are uncorrelated process noise and measurement noise vectors respectively, with zero means and covariance matrices $\mathbf{Q}$ and $\mathbf{R}$. The EKF estimation algorithm summarized in Eqs. (2-6), starts with initial estimate of states $\mathbf{X}_0$ with covariance of $\mathbf{P}_0$, followed by a recursive process of state prediction and state updates for each observation.

For the initialization,

$$\mathbf{X}_{0|0} = E[\mathbf{X}(t_0)] \; ; \mathbf{P}_{0|0} = \text{covariance}[\,\mathbf{X}(\mathrm{t}_0)] = E[\mathbf{X}(t_0)\mathbf{X}(t_0)^{\mathrm{T}}] \tag{2}$$

After obtaining values, use the model of Eq. (1) to predict the state and covariance at the next time step. Given $\mathbf{X}_{k-1}$, integrate the system and covariance matrices from $t_{k-1}$ to $t_k$

$$\begin{cases} \dot{\mathbf{X}}(t) = \mathbf{f}(\mathbf{X}(t), \mathbf{u}(t), t) \\ \dot{\mathbf{P}}(t) = \mathbf{A}(t)\mathbf{P}(t) + \mathbf{P}(t)\mathbf{A}(t)^{\mathbf{T}} + \mathbf{Q}(t) \end{cases} \Rightarrow \begin{cases} \widehat{\mathbf{X}}_{k|k-1} = \mathbf{X}(t) \\ \mathbf{P}_{k|k-1} = \mathbf{P}(t) \end{cases} ; \quad \mathbf{A}(t) = \frac{\partial \mathbf{f}}{\partial \mathbf{X}}\Big|_{\mathbf{x}_{k|k-1}} \tag{3}$$

The notation $\widehat{\ }$ indicates an estimate, and $k|k-1$ denotes the value estimated or obtained at time step $k$, given the observations at time step $k-1$.

The update step calculates a posteriori values:

$$\mathbf{K}_k = \mathbf{P}_{k|k-1}\mathbf{H}_k^{\mathrm{T}}\left(\mathbf{H}_k\mathbf{P}_{k|k-1}\mathbf{H}_k^{\mathrm{T}} + \mathbf{R}\right)^{-1} \tag{4}$$

$$\widehat{\mathbf{X}}_{k|k} = \widehat{\mathbf{X}}_{k|k-1} + \mathbf{K}_k\left(\mathbf{Y}_k - \mathbf{h}\left(\widehat{\mathbf{X}}_{k|k-1}, t_k\right)\right) \tag{5}$$

$$\widehat{\mathbf{P}}_{k|k} = (\mathbf{I} - \mathbf{K}_k\mathbf{H}_k)\mathbf{P}_{k|k-1}. \tag{6}$$

Here $\mathbf{H}_k = \frac{\partial \mathbf{h}}{\partial \mathbf{X}}|_{\mathbf{x}_{k|k-1}}$ and $\widehat{\mathbf{X}}_{k|k}$ is the estimated state vector with the estimation covariance $\widehat{\mathbf{P}}_{k|k}$. Jacobian matrices $\mathbf{A}$ and $\mathbf{H}$ linearize the system and the observation models locally about estimation points.

Parameters can be estimated with EKF by augmenting the state vector with the set of parameters. Then, EKF estimates states and parameters together from observations. To estimate $k$ parameters $p_1, \ldots, p_k$, the augmented state vector $\mathbf{X} \in \Re^{(n+k)\times 1}$ has $n+k$ elements. Augmented function $\mathbf{f} \in \Re^{(n+k)\times 1}$ has $k$ zero elements appended to the end of the vector. Process noise vector $\mathbf{w} \in \Re^{(n+k)\times 1}$ corresponds to states and parameters. Machine degradation is associated with changes of parameters with time. However, since the time constants associated with the parameter change are large, parameters are modeled as time-invariant states. Elements of process noise vector $\mathbf{w}(\mathrm{t})$ introduce uncertainty factors into the model, to compensate this modeling error.

## 6.3 DYNAMIC PROCESS NOISE

In an extended Kalman filter, estimation errors due to local unobservability, filter divergence or biased estimations can invalidate results. In practice, estimation errors cannot be directly obtained since actual values of parameters are not available. Here, a validation index based on the Chi-square test of probability and statistics [92] is defined to evaluate the performance of the filter.

The measurement prediction covariance $\mathbf{S}$ and the measurement residual vector $\mathbf{r}$ in EKF are

$$\mathbf{S}_k = \mathbf{H}_k \mathbf{P}_{k|k-1} \mathbf{H}_k^{\mathrm{T}} + \mathbf{R} \tag{7}$$

$$\mathbf{r}_k = \mathbf{Y}_k - \mathbf{h}\left(\widehat{\mathbf{X}}_{k|k}, t_k\right). \tag{8}$$

The validation index is defined about each measurement as

$$\delta_k = \mathbf{r}_k^{\mathrm{T}} \mathbf{S}_k^{-1} \mathbf{r}_k. \tag{9}$$

For each estimation, the value of scalar $\delta_k$ provides an indirect indicator of the estimation error. Also, dynamic updates of the process noise covariance at each step is done using the validation index $\delta$ via

$$\mathbf{Q}_{ii} = \delta^{\alpha_i} \mathbf{Q}_{0_{ii}} \quad ; \quad i = 1, 2, \dots, n+k \tag{10}$$

Here $\mathbf{Q}_0$ is the diagonal static covariance matrix. Subscripts $ii$ indicate the diagonal elements, and the constant exponent $\alpha_i$ relates the sensitivity of the process noise element for each state to the validation index. For $\alpha_i = 0$, the process noise is

static. Higher values of $\alpha_i$ make the process noise dynamic and more sensitive to the validation index. Note that $\alpha_i$ can be different for each state.

## 6.4 STATOR AND ROTOR FAULT DETECTIONS USING EKF

A continuous-discrete extended Kalman filter, Eqs. (2-6), was applied to the induction motor (Table 10) to tune parameters associated with stator winding faults $R_{m1}$ and $R_{s1}$, broken rotor bar faults $R_r$, and bearing friction $R_{br}$. Different cases of measurements were studied (Table 11). Parameters of the actual system change independently when the motor is running.

Table 10 Induction Motor specifications

| Parameter | Value |
|---|---|
| Number of rotor coil turns, $n_r$ | 1 |
| Number of stator winding turns, $n_s$ | 111 |
| Number of rotor bars, $n$ | 34 |
| Number of poles, $p$ | 2 |
| Stator coil resistance, $R_{s1}, \dots, R_{s3}$ [Ω] | 2.1 |
| Stator magnetic losses, $R_{m1}, \dots, R_{m3}$ [1/Ω] | 0.03539 |
| Rotor bar resistance, $R_{r1}, \dots, R_{r34}$ [Ω] | 0.8663 |
| Stator inductance, $L_s$, [H] | 1.02938 |
| Rotor inductance, $L_r$, [H] | 0.9834 |
| Mutual inductance, $L_m$, [H] | 1.00130 |
| Bearing friction, $R_{br}$, [N.s/m] | 0.0085 |
| Moment of inertia, $J$, [N. m$^2$] | 0.0115 |

Table 11 Different combinations of measurements used for parameter tuning

| Case | Measurements |
|---|---|
| 1 | $I_1, \omega$ |
| 2 | $I_1, \theta$ |
| 3 | $I_1, I_2, I_3$ |

| | |
|---|---|
| 4 | $I_1, I_2, I_3, \omega$ |
| 5 | $I_1, \theta, \omega$ |
| 6 | $I_1, I_2, I_3, \theta$ |
| 7 | $I_1, I_2, \theta, \omega$ |
| 8 | $I_1, I_2, I_3, \theta, \omega$ |

The performance of the EKF tracking is shown in Figure 58. The state vector $\mathbf{X}$ contains 6 states and the 4 parameters.

$$\mathbf{X} = [\varphi_{s\alpha} \quad \varphi_{s\beta} \quad \varphi_{r\alpha} \quad \varphi_{r\beta} \quad h \quad \theta \quad R_{m1} \quad R_{s1} \quad R_r \quad R_{br}]$$

The process noise $\mathbf{w}$ and the measurement noise $\mathbf{v}$ at the EKF are assumed to be uncorrelated Gaussian noise, with diagonal covariance matrices $\mathbf{Q}$ and $\mathbf{R}$. The process noise covariance matrix should be chosen and tuned for an EKF based on uncertainties of the model and the measurement noise covariance is selected based on the nature and the accuracy of the sensors. Here, $\mathbf{Q}$ and $\mathbf{R}$ are chosen as

$$\mathbf{Q} = \text{diagonal}(10^{-4} \times [1 \quad 1 \quad 1 \quad 1 \quad 1 \quad 1 \quad 2 \quad 150 \quad 70 \quad 0.6]) \tag{11}$$

$$\mathbf{R} = \text{diagonal}[1 \quad 1 \quad 1 \quad 1] \tag{12}$$

The estimation is assigned initial values

$$\widehat{\mathbf{X}}_0 = [0 \quad 0 \quad 0 \quad 0 \quad 4.2 \quad 0 \quad 0.1 \quad 1 \quad 1 \quad 0.007]. \tag{13}$$

Note that initial estimates of parameters in (13) (last four elements of $\widehat{\mathbf{X}}_0$) vary at least 50% from the actual values and the filter is insensitive to the initial values. The initial error covariance $\mathbf{P}_0$ is the expected value $E\left[(\mathbf{X}_0 - \widehat{\mathbf{X}}_0)(\mathbf{X}_0 - \widehat{\mathbf{X}}_0)^{\mathrm{T}}\right]$. However, in

a real estimation, because the actual values of $\mathbf{X}_0$ are not known, the initial error covariance matrix was assumed to be a unity matrix. Figure 58 shows estimation results for observations: (a) $\{I_1, \omega\}$ corresponding to the unobservable case 1 in Table 11, (b) $\{I_1, I_2, I_3, \omega\}$ corresponding to the observable case 4 in Table 11. Results of observability analysis in chapter 5 showed the system with measurements $\{I_1, \omega\}$ (case 1 in Table 11) not observable. Estimation of the stator magnetic resistance was successful for both observable and unobservable cases. However, other parameters cannot be accurately tuned from $I_1$, and $\omega$ as shown in Figure 58(b-d). Adding two more current signals $I_2, I_3$ to the observations enables the EKF to tune the parameters more accurately, as the curves labeled $I_1, I_2, I_3, \omega$ suggest. Note that parameters change simultaneously in the actual system, representing severe and rapid degradation in the motor.

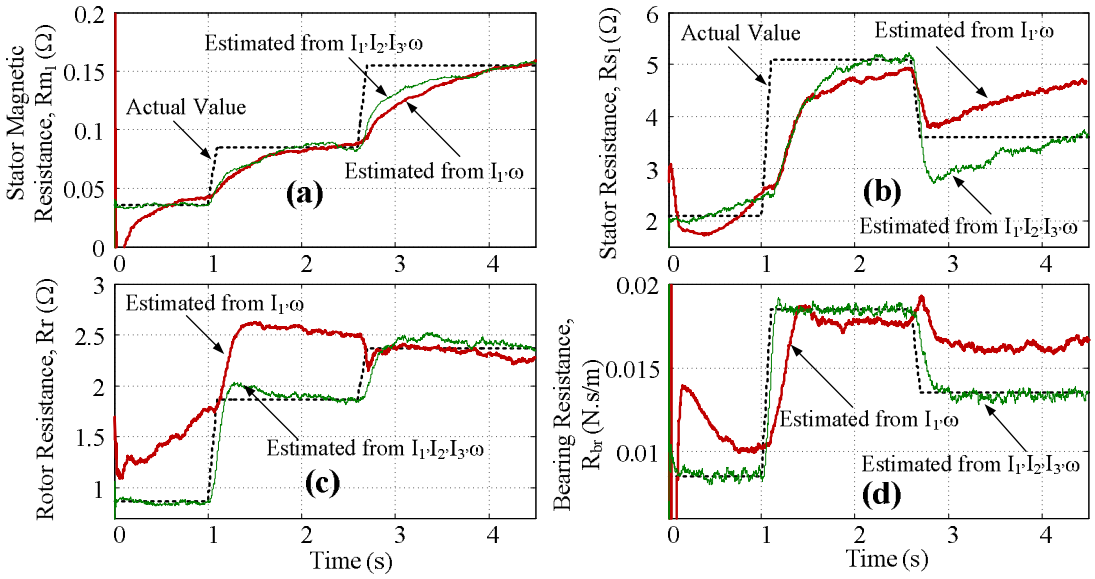


Figure 58 Tuning of parameters of a) Stator magnetic resistance $R_{sm1}$ b) stator winding resistance $R_{s1}$, c) rotor resistance $R_r$, d) bearings friction $R_{br}$ of an induction motor using EKF from different measurements: $I_1, \omega$ (unobservable case 1 in Table 11) and $I_1, I_2, I_3, \omega$ (observable case 4).

Figure 59 shows actual speed of the motor $\omega$, measured speed $\omega$ + noise, and the estimated speed $\hat{\omega}$, for parameter estimations derived from $\{I_1, I_2, I_3, \omega\}$. At the first step of degradation at $t \approx 1.1$, speed reduces. At the second stage at $t \approx 2.7$, speed increases slightly. By comparing the actual measurements contaminated with noise (solid line) to the estimated signals (fine dashed line), the EKF performance in filtering measurement noise can be observed.

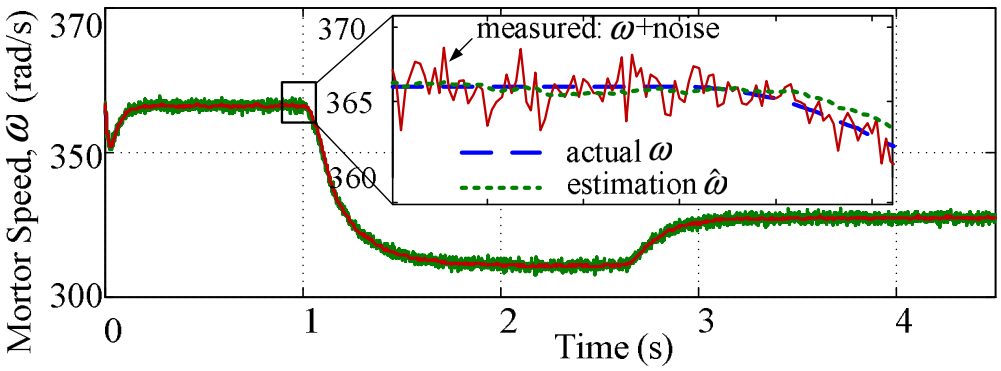


Figure 59 Motor speed during the estimation of 4 parameters $R_{m1}, R_{s1}, R_r, R_{br}$ from measurements of $I_1$, $I_2$, $I_3, \omega$.

Residuals, the difference between estimated and measured signals, are plotted versus time in Figure 60 for case 4 with measurements $\{I_1, I_2, I_3, \omega\}$, and in Figure 61 for case 1 with measurements $\{I_1, \omega\}$. The level and excursions of residuals for $I_1$ and $\omega$ in Figure 60 and Figure 61 are similar. The unobservable case 1 in Figure 61 does not generate residuals significantly greater than the observable case in Figure 60. However, the residuals of $\{I_1, \omega\}$ do not have enough information to determine a unique solution for the parameters causing incorrect estimations. With everything else in the system the same, different combinations of parameters can render the same observations. This issue is observed in parameter tuning in Figure 58(b,d), where estimated parameters

$R_{s1}$ and $R_{br}$ are biased from these actual values at $t = 4$, whereas the two other parameters are close to their actual values.

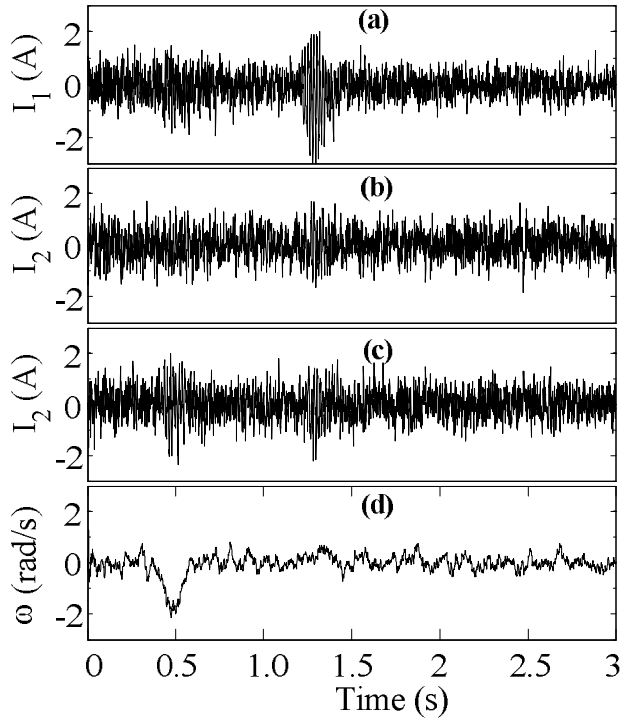


Figure 60 Residuals in parameter tuning of $R_{m1}, R_{s1}, R_r, R_{br}$ from measurements $I_1,\ I_2,\ I_3, \omega$.

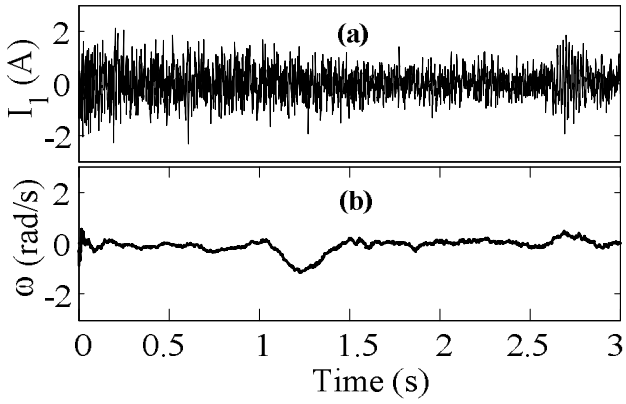


Figure 61 Residuals in parameter tuning of $R_{m1}, R_{s1}, R_r, R_{br}$ from measurements $I_1, \omega$.

A residual increase can arise from system faults, sensor faults or measurement errors. Assuming healthy sensors, the EKF minimizes the residuals by tuning the states and parameters of the system. The same technique can be used for sensor fault detection using redundant sensors. In this case, the observability analysis described in section 3 selects a sensor system with sufficient redundancy.

The performance of the EKF in detection of broken bars associated with the change of rotor resistance $R_r$ is shown in Figure 62, for different measurements. Tuning $R_r$ with $\{I_1, I_2, I_3\}$ leads to the final biased estimation. Adding observation $\omega$ can improve the accuracy of the filter.

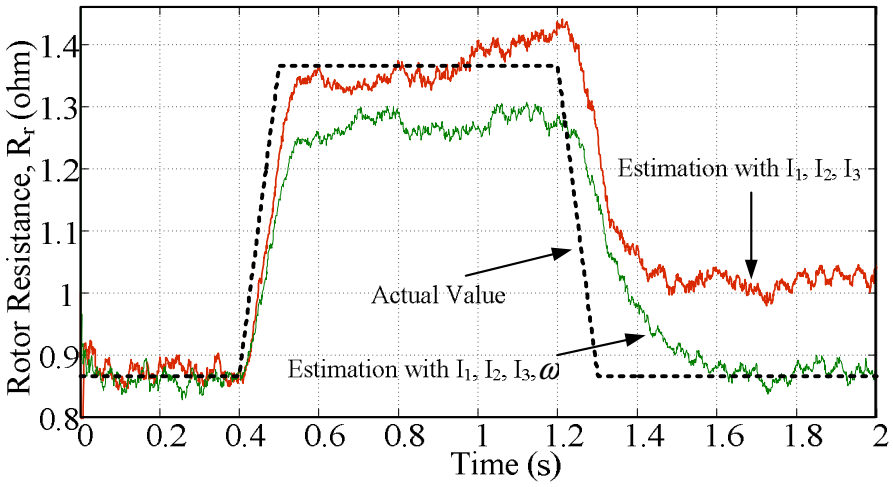


Figure 62 Effect of adding extra measurement (encoder signal, $\omega$) in detection of broken rotor bars

## 6.5 MOTOR LOAD DETECTION USING EKF

Mechanical loads significantly change motor states and measurements. Parameter tuning for model-based diagnostics in induction motors requires knowledge of the load,

since the model must emulate the real system. Torque measurement at the motor coupling is costly and often impossible. Besides diagnostics, measuring motor mechanical loads is of interest to industry. An accurate estimate of motor loads from current and speed signals, without mechanical sensors, could be useful.

The motor torque load $T_l$ can be treated as a parameter appended to the estimation vector, and estimated using the extended Kalman filter. However, due to the observability issue, EKF might find a biased estimation, if many parameters are estimated at the same time. A specifically designed filter can estimate the mechanical load from current signals, given the values of parameters. Here, a separate filter tunes the parameters of the motor without load (or with a reference load). Then, the estimated parameters are treated as constant, and the load detection filter finds and tracks $T_l$ when the motor is loaded. Figure 63 shows load estimation in the induction motor (Table 10) from measurements of $\{I_1, I_2, I_3\}$, when the motor runs with a variable load. Parameters have values associated with a healthy system (Table 10) and

$$\mathbf{Q} = \text{diagonal}(10^{-4} \times [1 \quad 1 \quad 1 \quad 1 \quad 1 \quad 1 \quad 0.1]) \tag{14}$$

$$\mathbf{R} = \text{diagonal}[1 \quad 1 \quad 1] \tag{15}$$

$$\mathbf{X} = [\varphi_{s\alpha} \quad \varphi_{s\beta} \quad \varphi_{r\alpha} \quad \varphi_{r\beta} \quad h \quad \theta \quad R_{br}] \tag{16}$$

$$\widehat{\mathbf{X}}_0 = [0 \quad 0 \quad 0 \quad 0 \quad 4.2 \quad 366 \quad 2]. \tag{17}$$

In Figure 63, actual values of motor speed drop slightly with a load increase, and elevate with a load decrease. The filter accurately follows the load profile; see Figure 63(b). The estimated motor speed roughly follows the actual motor speed trend. At the moment of the load change, a temporary false estimate of the motor speed occurs, which corrects after one second.

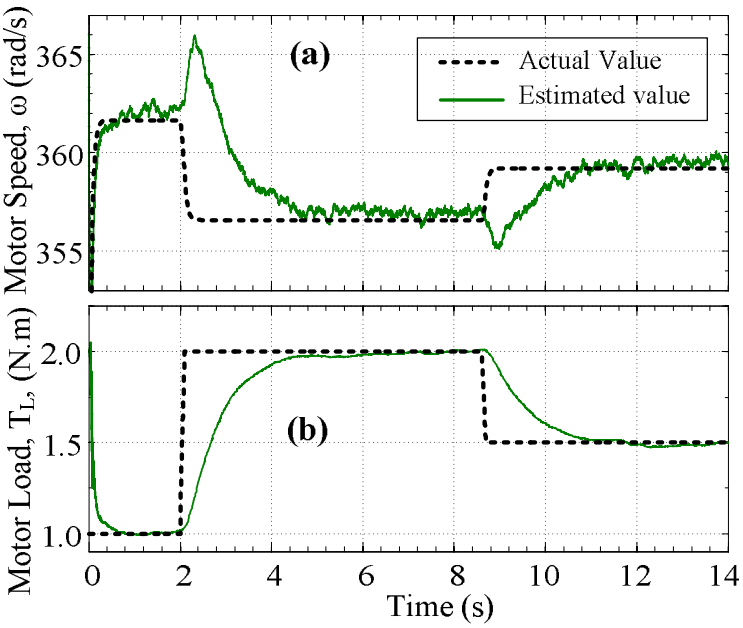


Figure 63 Estimation of motor load from measurements of $I_1, I_2, I_3$. (a) Motor speed during the estimation, (b) actual and estimated values of the load.

## 6.6 DYNAMIC PROCESS NOISE

Performance of the dynamic process noise in EKF for parameter tuning is studied here. An EKF designed to detect of broken rotor bars tunes the rotor resistance from observations $\{I_1, I_2, I_3, \omega\}$, when the rotor resistance changes from 2.1Ω to 5Ω, and then to 3.5Ω. The corresponding normalized estimation error $\left(\mathbf{R} - \widehat{\mathbf{R}}\right)/\mathbf{R}$, and normalized validation index $\delta^3$ from Eq. (9) are shown in Figure 64(a, b). In practice, since the estimation error cannot be evaluated (actual values are not available), the validation index estimates the accuracy of the filter. This value updates the process noise for each estimate, via Eq. (10). The performance of the filter is shown in Figure 65(a, b), for rotor resistance estimation with different values of $\alpha$ ($\mathbf{Q} = \delta^{\alpha}\mathbf{Q}_0$).

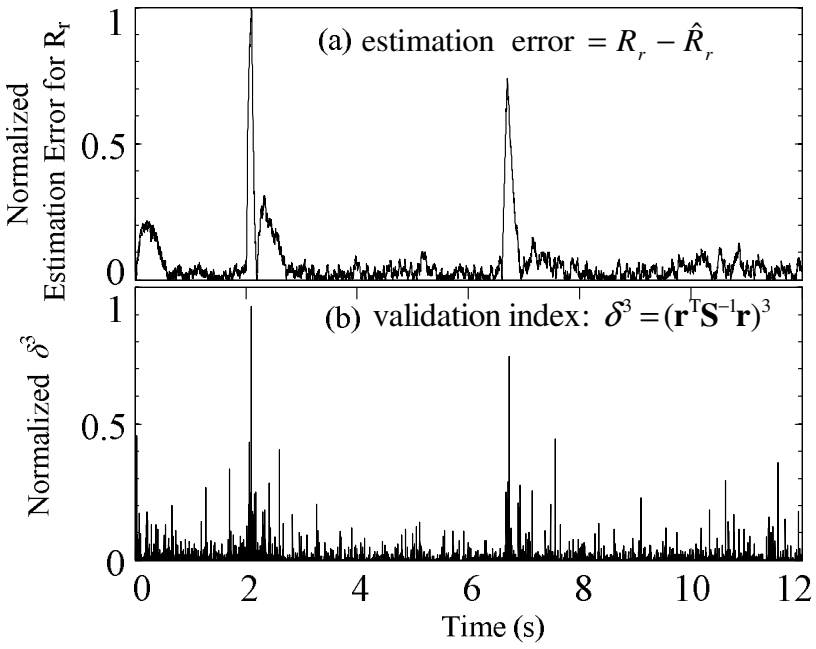


Figure 64 Validation index $\delta^3$ evaluates the estimation. a) Normalized estimation error for the rotor resistance estimation, b) Estimation validation index $\delta^3$ (Chi-square test)

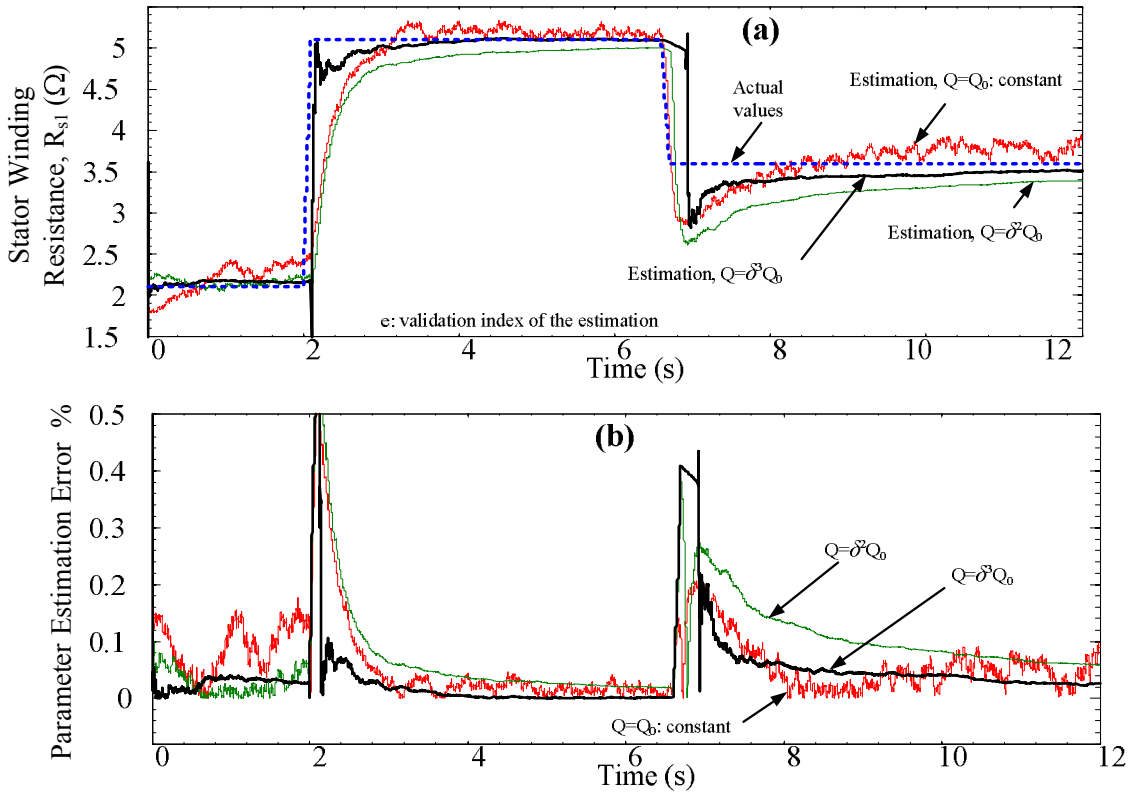


Figure 65 Performance of dynamic process noise in extended Kalman filter for estimation of stator winding resistance. Process noise covariance $\mathbf{Q}$ is updated based on the validation index $\delta$ as $\mathbf{Q} = \delta^{\alpha}\mathbf{Q}_0$, a) estimation of $R_{s1}$ with different values of $\alpha$ b) estimation error for different $\alpha$

For estimation with constant process noise ($\mathbf{Q} = \mathbf{Q_0}$), the response of the filter is slow, and steady state values of the parameter fluctuate because of intense process noise. Dynamic process noise changes matrix $\mathbf{Q}$, based on the validation index causing much less steady state error. Dynamic process noise with the higher order coefficient $\delta^3$ is much faster and more accurate than with coefficient $\delta^2$, due to higher sensitivity of the process noise to the estimation error. However, a high sensitivity might lead the system to singular points, since the process noise elements tend to increase significantly at the time of the parameter changes. For the motor, $\delta^2$ or $\delta^3$ is recommended. Note that the overshoot of estimation error for dynamic process noise is much higher than static

process noise. However, for fault detection of slowly degrading systems, the present values of parameters are desired, and the temporary overshoot error should not be an issue.

## 6.7 SUMMARY AND CONCLUSIONS

A systematic algorithm for model-based diagnostics of induction motors to detect stator and rotor faults was introduced. A continuous-discrete Extended Kalman Filter (EKF) was designed to detect stator winding faults and broken rotor bars in the induction motor. Results of parameter tuning using EKF showed four parameters—stator winding resistance, rotor resistance, stator magnetic resistance, and bearing friction—can be tuned together with measurements of currents and motor speed. Simulations showed that mechanical loads on the motor and motor speed can be estimated using EKF with measurements of three currents. The validation index evaluating filter accuracy was used to update the process noise in EKF during estimation. Dynamic process noise technique in EKF for parameter tuning of rotor resistance increased the overshoot error and decreased the steady state estimation error. Results showed that a model-based diagnostics system can detect stator and rotor faults, with estimations of bearing resistance and motor loads, as long as the system is observable with the given configuration of measurements.

# Chapter 7

# Summary and Conclusions

## 7.1 SUMMARY AND CONCLUSIONS

A detailed model of rolling element bearings developed in vector bond graphs, incorporated multibody dynamics of elements, centrifugal effects, dynamics of contacts, and surface defects. Newton-Euler's equations for each element were encoded into bond graphs, with dynamics of contacts, traction forces, and rotational frictions formulated as constitutive laws of elements. A kinematic-based fault model was introduced. Tribological faults were modeled as surface profile changes, which generate impulses via dynamic interactions of faults and bearing elements. Simulations for different clearances and radial loads show ability of the model to incorporate load zone effects in vibration signals. Experiments for healthy and faulty rolling element bearings validated the model. A parametric study investigated effects of type, size, and shape of faults on vibration responses. Dynamics of contacts under faults demonstrated how fault impulses are physically generated. The proposed modular and generic bond graph model represents complex dynamics of normal and defective bearings. With physical and kinematic parameters assigned to faults, the model can predict bearing response for fault conditions, and thus be used in diagnostics for information processing necessary for condition monitoring of machinery.

Feature plot, a signal processing technique for machine diagnostics based on time feature extraction of variable window averaging, was developed, formulated, and illustrated with a simple example of sinusoidal functions. Time feature plots and frequency feature were constructed. Fault indicators were obtained from peaks of feature

plots in fault regions. Feature plot technique was applied to rolling element bearings with localized severe and rough surface faults. Time and frequency feature plots were constructed from vibration signals of healthy and faulty bearings, and fault indicators representing type and severity of the faults were obtained from residual feature plots. 28 sets of bearing vibration measurements with localized faults: Inner Race Faults (IRF), Ball Faults (BF), Outer Race Faults (ORF), and Combined Faults (CF) were tested. Experiments included vibration signals measured in both vertical and horizontal directions with high and low sampling frequencies. For each case, fault indicators were obtained and the ability of the developed diagnostic technique to detect and isolate bearing faults was demonstrated. Also, rough surface faults that generate minimum noise carried by the other signals in the machine were tested experimentally. First and second derivatives of acceleration were used to amplify and isolate fault signals from other signals in the case of rough surface faults. Faults were detected and isolated using the feature plot technique. The performance of feature plot technique with several time features such as skewness, kurtosis, RMS, peak value, crest factor, impulse factor and mean absolute deviation in diagnostics of rolling element bearings were investigated. The effectiveness of feature plots when only a short segment of data was available was presented, and results were compared with power spectrum density technique. Results showed the effectiveness of feature plots in diagnostics of rolling element bearings. Fault regions at the first harmonics of fault components in feature plots provide rich search range to retrieve fault information and to obtain fault indicators. Feature plots can be used for fault severity analysis, since time features are directly related to the fault signals. Signal averaging makes the feature plot technique useful for faults with complicated behavior such as IRF and BF. Frequency feature plots contain high resolution in low frequencies, providing a useful diagnostic tool when signal samples are limited. Having

multiple faults in bearings, vibration signals contain more sets of periodic impulses generating peaks in feature plots. Therefore, feature plots can also detect multiple bearings defects.

A systematic algorithm for model-based diagnostics of induction motors including physics-based modeling, observability analysis and parameter tuning was presented. Detailed bond graph model of a three-phase induction motor was simulated and validated with experiments. Nonlinear observability analysis using Lie derivatives investigated the performance of the model-based diagnostics, with several configurations of measurements and parameters. Results of the observability analysis of the induction motor can be used to design a sensor configuration with enough redundancy for detection of system faults or sensor faults. A continuous-discrete Extended Kalman Filter (EKF) was designed to detect stator winding faults and broken rotor bars in the induction motor. Results of parameter tuning using EKF showed four parameters—stator winding resistance, rotor resistance, stator magnetic resistance, and the bearing friction—can be tuned together with measurements of currents and motor speed. Simulations showed that mechanical loads on the motor and motor speed can be estimated using EKF with measurements of three currents. Results suggest that complex step Jacobian technique improves computational performance of observability analysis and parameter tuning. The validation index evaluating filter accuracy was used to update the process noise in EKF during estimation. Dynamic process noise technique in EKF for parameter tuning of rotor resistance increased the overshoot error and decreased the steady state estimation error. Results showed that a model-based diagnostics system can detect stator and rotor faults, with estimations of bearing resistance and motor loads, as long as the system is observable with the given configuration of measurements.

## 7.2 CONTRIBUTIONS

Main contributions of the research are:

- A detailed vector bond graph model of rolling element bearing with physics of localized faults
- Feature plots, a new time-frequency signal processing technique for machine diagnostics. Also, a diagnostics algorithm based on the feature plot technique for detection, isolation, and assessment of localized severe and surface roughness faults in rolling element bearings were proposed.
- Nonlinear observability analysis technique for different combinations of sensors and parameters. The proposed technique can be used in model-based diagnostics to find the best configuration of sensors and parameters. Also, it can be used for sensor selections, sensor redundancy design, and sensor fusion analysis.
- An EKF tuning technique for model-based diagnostics with dynamic process noise and validation index to evaluate the performance of EKF in model-based diagnostics
- A general model-based diagnostic framework including bond graph modeling, nonlinear observability analysis, and parameter estimation using Extended Kalman Filter (EKF)

## 7.3 FUTURE WORK

Following suggestions are made to continue and improve the current research:

For modeling of the rolling element bearings:

- Incorporate flexibility and structural properties of elements and the cage into the model.

- Modify Hertzian contact to obtain contact force between non-pristine bodies, since contacts with faults are not pristine contacts.
- Incorporate the model of the structure of the machine and rotor into the bearing model. Vibration measurements of bearings are highly contaminated with misalignment, imbalance, and structural frequencies of the machine. The model can be extended to incorporate this effects and for more accurate fault diagnostics.
- For more validation of dynamic aspects of the model, the test rig can be modified to measure vertical and horizontal forces in bearing housing by installing strain gages on bearing supports.

For the feature plot technique:

- Apply the proposed feature plot diagnostic algorithm to the gears for detection, isolation, and assessment of different gear faults such as missing tooth, cracked tooth, chipped tooth, and localized surface defects.
- Apply the proposed bearing diagnostics technique to diagnostics of bearings with multiple faults.

For the observability analysis and model-based diagnostics of induction motors:

- Run experiments on an induction motor with stator winding and broken rotor bar faults to show the performance of the proposed diagnostic technique.
- Modify the induction motor model for asymmetrical time-varying rotor resistance to study the broken rotor bar and misaligned rotor faults in more detail.
- Conduct more experiments to show the effectiveness of mechanical load estimation using EKF in practice.

# Glossary

## CHAPTER 2 AND 3

| | |
|---|---|
| $C_s$ | bearing static load rating |
| $E$ | modulus of elasticity |
| $\mathbf{F}_i$ | external force vector acting on the body |
| $F_s$ | static equivalent load |
| $F_x, F_y, F_r, F_a$ | forces in $x$, $y$, radial and axial directions respectively |
| $F_\rho$ | curvatures difference |
| $\mathbf{J}$ | body rotational inertia matrix |
| $\mathbf{M}$ | body mass matrix |
| $\mathbf{T}$ | coordinate transformation matrix |
| $\mathbf{T_{GB}}$ | transformation matrix from the global to the body coordinate |
| $T_f$ | rotational resistive torque |
| $T_f$ | fault type (1: IRF, 2: BF, 3:ORF) |
| $T_{load}$ | resistive torques due to contact deformations |
| $T_{lub}$ | resistive torques due to lubrications |
| $T_{seal}$ | resistive torques due to rubbing seal |
| XYZ | global fixed coordinate |
| $b$ | contact damping factor |
| $d_b$ | balls diameter |
| $d_p$ | bearing pitch diameter |
| $f_r$ | bearing rotational speed in RPM |
| $r_f$ | fault size ratio |
| $v_0$ | kinematic viscosity of the lubricant |
| $K$ | contact stiffness |

| | |
|---|---|
| $k$ | equivalent linear stiffness of the bearing |
| $n$ | number of balls in the rolling element bearing |
| $r$ | radius of curvature |
| $\mathbf{r}$ | position vector with respect to the body coordinate |
| $s$ | contact slide-roll ratio |
| $\mathbf{x}$ | body position vector with respect to the global coordinate |
| $x^i y^i z^i$ | moving coordinate associated with the body $i$ |
| $x^{ij} y^{ij} z^{ij}$ | moving contact coordinate between bodies $i$ and $j$ |
| $v$ | Poisson's ratio |
| $w, h$ | width and depth of localized faults |
| $\Lambda$ | oil film parameter which is a function of oil film thickness |
| $\alpha_{ij}$ | orientation of the contact coordinate described in the global coordinate |
| $\beta_f$ | angular position of the fault defined in body coordinate |
| $\delta^*$ | dimensionless deflection factor |
| $\boldsymbol{\theta}$ | body angular position vector |
| $\theta_i$ | orientation of the body coordinate described in the global coordinate |
| $\mu$ | friction coefficient |
| $\mu_{bd}, \mu_{hd}$ | $\mu$ under boundary lubrication and hydrodynamic lubrication modes |
| $\rho$ | curvature |
| $\boldsymbol{\tau}$ | external torque vector acting on the body |
| $\phi$ | bearing contact angle |
| $\bar{}$ | bar accent assigned to vectors described in the body coordinate system |

## CHAPTER 4

| | |
|---|---|
| REB | Rolling Element Bearing |
| IRF | Inner Race Fault |
| BF | Ball Fault |
| ORF | Outer Race Fault |
| CF | Combined Faults: IRF and ORF |
| $\mathbf{D}$ | measurement time signal vector |
| $N$ | size of $\mathbf{D}$ in samples |
| $n_s$ | number of segments |
| $k$ | index of elements in a vector |
| $T$ | measurement time |
| $n_i$ | specific segment size in feature plots (in samples) |
| $t_i$ | specific segment size in feature plots (in time) |
| $\mathbf{d}_i$ | one segment of signals vector $\mathbf{D}$ |
| $n$ | size of data segment $\mathbf{d}$ in samples |
| $\overline{\mathbf{d}}$ | average vector obtained from $n_s$ segments $\mathbf{d}_i$ |
| SF | shape factor function |
| $d_b$ | ball diameter in bearing |
| $d_p$ | bearing pitch diameter |
| $f$ | frequency |
| $f_{BF}$ | ball fault frequency |
| $f_{IRF}$ | inner race fault frequency |
| $f_{ORF}$ | outer race fault frequency |
| $f_r$ | bearing rotational speed in RPM |
| $f_s$ | sampling frequency |

| | |
|---|---|
| $\phi$ | bearing contact angle |
| \ | quotient operator, which obtains integer part of two quantities ratio |

**CHAPTER 5 AND 6**

| | |
|---|---|
| CSJ | Complex Step Jacobian |
| EKF | Extended Kalman Filter |
| X | state vector |
| **Y** | output vector |
| **u** | input vector |
| **r** | residual vector |
| **v** | measurement noise vector |
| $I_1, I_2, I_3$ | motor phases currents |
| $n_s, n_r$ | stator winding turns and rotor turns ($n_r = 1$) |
| $n$ | number of rotor bars |
| $p$ | number of poles |
| $L_s, L$ | rotor, and stator self inductance |
| $L_m$ | mutual inductance |
| **V** | input voltages vector |
| $T_l$ | mechanical load on motor |
| $\theta$ | rotor angular position |
| $\omega$ | rotor speed |
| $\mathbf{R_s}, \mathbf{R_m}$ | diagonal matrix of electrical and magnetic resistances of stator |
| $\varphi_{s\alpha}, \varphi_{s\beta}$ | stator magnetic fluxes along $\alpha$ and $\beta$ axes |
| $\varphi_{r\alpha}, \varphi_{r\beta}$ | rotor magnetic fluxes along $\alpha$ and $\beta$ axes |

| | |
|---|---|
| $h$ | rotor angular momentum |
| $R_{br}$ | bearing resistance |
| $J$ | rotor inertia |
| $\mathbf{O}$ | observability matrix |
| $\mathbf{f}$ | nonlinear state equation vector function |
| $\mathbf{h}$ | nonlinear output vector function |
| $\boldsymbol{L_f h}$ | Lie derivative of $\mathbf{h}$ with respect to $\mathbf{f}$ |
| $_{(m\times n)}$ | subscript defining the size a vector |
| $\mathbf{S}$ | diagonal matrix of singular values |
| $\sigma$ | singular value |
| $C$ | observability index as the ratio of $\sigma_{max}/\sigma_{min}$ |
| $\mathbf{P}$ | covariance matrix |
| $\mathbf{A}, \mathbf{H}$ | linearized system and observation model |
| $\mathbf{S}$ | measurement prediction covariance |
| $\delta$ | validation index |
| $\mathbf{Q}$ | process noise covariance matrix |
| $\mathbf{w}$ | process noise vector |
| $\mathbf{R}$ | measurement covariance matrix |
| $t$ | time |
| $f$ | line frequency |
| $\widehat{\ }$ | hat accent denoting estimated values |

# Bibliography


[1] Raison, B., Rostaing, G., Butscher, O., and Maroni, C. S., 2002, "Investigations of Algorithms for Bearing Fault Detection in Induction Drives," IECON-2002: Proceedings of the 2002 28th Annual Conference of the IEEE Industrial Electronics Society, Vols 1-4, pp. 1696-1701.

[2] Paynter, H. M., 1961, *Analysis and Design of Engineering Systems*, M. I. T. Press, Cambridge, Mass.,.

[3] Gertler, J., 1998, *Fault Detection and Diagnosis in Engineering Systems*, Marcel Dekker, New York.

[4] Isermann, R., 1997, "Supervision, Fault-Detection and Fault-Diagnosis Methods - an Introduction," Control Engineering Practice, **5**(5), pp. 639-652.

[5] Frank, P. M., Ding, S. X., and Marcu, T., 2000, "Model-Based Fault Diagnosis in Technical Processes," Transactions of the Institute of Measurement and Control, **22**(1), pp. 57-101.

[6] 1985, "Report of Large Motor Reliability Survey of Industrial and Commercial Installations, Part I," Industry Applications, IEEE Transactions on, **IA-21**(4), pp. 853-864.

[7] Craig, M., Harvey, T. J., Wood, R. J. K., Masuda, K., Kawabata, M., and Powrie, H. E. G., 2009, "Advanced Condition Monitoring of Tapered Roller Bearings, Part 1," Tribology International, **42**(11-12), pp. 1846-1856.

[8] Raadnui, S., 2004, "Used Grease Analysis for Rolling Element Bearing Condition Monitoring," Quality, Reliability, and Maintenance, pp. 97-99.

[9] Kim, Y.-H., Tan, A. C. C., Mathew, J., and Yang, B.-S., 2006, Engineering Asset Management, Springer London, Condition Monitoring of Low Speed Bearings: A Comparative Study of the Ultrasound Technique Versus Vibration Measurements.

[10] Burstein, L., 2005, "Relationships for Machine Thermal Diagnostics: Theoretical and Empirical Considerations," NDT & E International, **38**(1), pp. 69-75.

[11] Jung, J. C., Chang, Y. W., and Seong, P. H., 2004, "Application of an Integrated Power Line Signal Analysis Methodology to the Detection of Major Rotating Machine Abnormalities in Nuclear Power Plants," Nuclear Engineering and Design, **229**(2-3), pp. 307-315.

[12] Yoshioka, T., and Shimizu, S., 2009, "Monitoring of Ball Bearing Operation under Grease Lubrication Using a New Compound Diagnostic System Detecting Vibration and Acoustic Emission," Tribology Transactions, **52**(6), pp. 725-730.

[13] Samanta, B., and Al-Balushi, K. R., 2003, "Artificial Neural Network Based Fault Diagnostics of Rolling Element Bearings Using Time-Domain Features," Mechanical Systems and Signal Processing, **17**(2), pp. 317-328.

[14] Patil, M. S., Mathew, J., and Rajendrakumar, P. K., 2008, "Bearing Signature Analysis as a Medium for Fault Detection: A Review," Journal of Tribology-Transactions of the Asme, **130**(1).

[15] Randall, R. B., Antoni, J., and Chobsaard, S., 2000, "A Comparison of Cyclostationary and Envelope Analysis in the Diagnostics of Rolling Element Bearings," 2000 IEEE International Conference on Acoustics, Speech, and Signal Processing, pp. 3882-3885.

[16] Shi, L., Randall, R. B., and Antoni, J., 2004, "Rolling Element Bearing Fault Detection Using Improved Envelope Analysis," Vibrations in Rotating Machinery, **2004**(2), pp. 301-311.

[17] Ho, D., and Randall, R. B., 2000, "Optimisation of Bearing Diagnostic Techniques Using Simulated and Actual Bearing Fault Signals," Mechanical Systems and Signal Processing, **14**(5), pp. 763-788.

[18] Peng, Z. K., and Chu, F. L., 2004, "Application of the Wavelet Transform in Machine Condition Monitoring and Fault Diagnostics: A Review with Bibliography," Mechanical Systems and Signal Processing, **18**(2), pp. 199-221.

[19] Nikolaou, N. G., and Antoniadis, I. A., 2002, "Rolling Element Bearing Fault Diagnosis Using Wavelet Packets," NDT & E International, **35**(3), pp. 197-205.

[20] Lakis, A. A., 2007, "Rotating Machinery Fault Diagnosis Using Time-Frequency Methods," Challenges in Power, High Voltages and Machines, pp. 139-144.

[21] Baydar, N., and Ball, A., 2001, "A Comparative Study of Acoustic and Vibration Signals in Detection of Gear Failures Using Wigner-Ville Distribution," Mechanical Systems and Signal Processing, **15**(6), pp. 1091-1107.

[22] Mcfadden, P. D., and Toozhy, M. M., 2000, "Application of Synchronous Averaging to Vibration Monitoring of Rolling Element Bearings," Mechanical Systems and Signal Processing, **14**(6), pp. 891-906.

[23] Zhu, L., Ding, H., and Zhu, X. Y., 2007, "Synchronous Averaging of Time-Frequency Distribution with Application to Machine Condition Monitoring," Journal of Vibration and Acoustics, **129**(4), pp. 441-447.

[24] Halim, E. B., Choudhury, M. a. a. S., Shah, S. L., and Zuo, M. J., 2008, "Time Domain Averaging across All Scales: A Novel Method for Detection of Gearbox Faults," Mechanical Systems and Signal Processing, **22**(2), pp. 261-278.

[25] 2003, "Virtual Machine Design Workshop – Defining the Requirements for the Next Generation of Analytical Software for the Design of Rotating Components," Technical Report No. Purde Univesrity,

[26] Jones, A. B., 1960, "A General Theory for Elastically Constrained Ball and Roller Bearing under Arbitrary Load and Speed Conditions," ASME Journal of Basic Engineering, **82**(21), pp. 309-320.

[27] Gupta, P. K., 1979, "Dynamics of Rolling-Element Bearings .1. Cylindrical Roller Bearing Analysis," Journal of Lubrication Technology-Transactions of the Asme, **101**(3), pp. 293-304.

[28] Mcfadden, P. D., and Smith, J. D., 1984, "Vibration Monitoring of Rolling Element Bearings by the High-Frequency Resonance Technique -- a Review," Tribology International, **17**(1), pp. 3-10.

[29] Afshari, N., and Loparo, K. A., 1998, "A Model-Based Technique for the Fault Detection of Rolling Element Bearings Using Detection Filter Design and Sliding Mode Technique," Proceedings of the 37th IEEE Conference on Decision and Control, Vols 1-4, pp. 2593-2598.

[30] Adams, M. L., and Loparo, K. A., 2004, "Analysis of Rolling Element Bearing Faults in Rotating Machinery - Experiments, Modelling, Fault Detection, and Diagnosis," Vibrations in Rotating Machinery, **2004**(2), pp. 511-520.

[31] Harsha, S. P., 2006, "Nonlinear Dynamic Analysis of Rolling Element Bearings Due to Cage Run-out and Number of Balls," Journal of Sound and Vibration, **289**(1-2), pp. 360-381.

[32] El-Saeidy, F. M. A., and Sticher, F., 2010, "Dynamics of a Rigid Rotor Linear/Nonlinear Bearings System Subject to Rotating Unbalance and Base Excitations," Journal of Vibration and Control, **16**(3), pp. 403-438.

[33] Liew, A., Feng, N., and Hahn, E. J., 2002, "Transient Rotordynamic Modeling of Rolling Element Bearing Systems," Journal of Engineering for Gas Turbines and Power-Transactions of the Asme, **124**(4), pp. 984-991.

[34] Sopanen, J., and Mikkola, A., 2003, "Dynamic Model of a Deep-Groove Ball Bearing Including Localized and Distributed Defects. Part 1: Theory," Proceedings of the Institution of Mechanical Engineers Part K-Journal of Multi-Body Dynamics, **217**(3), pp. 201-211.

[35] Sopanen, J., and Mikkola, A., 2003, "Dynamic Model of a Deep-Groove Ball Bearing Including Localized and Distributed Defects. Part 2: Implementation and Results," Proceedings of the Institution of Mechanical Engineers Part K-Journal of Multi-Body Dynamics, **217**(3), pp. 213-223.

[36] Jang, G., and Jeong, S. W., 2004, "Vibration Analysis of a Rotating System Due to the Effect of Ball Bearing Waviness," Journal of Sound and Vibration, **269**(3-5), pp. 709-726.

[37] Changqing, B., and Qingyu, X., 2006, "Dynamic Model of Ball Bearings with Internal Clearance and Waviness," Journal of Sound and Vibration, **294**(1-2), pp. 23-48.

[38] Patil, M. S., Mathew, J., Rajendrakumar, P. K., and Desai, S., 2010, "A Theoretical Model to Predict the Effect of Localized Defect on Vibrations Associated with Ball Bearing," International Journal of Mechanical Sciences, **52**(9), pp. 1193-1201.

[39] Wensing, J. A., 1998, "Dynamic Behaviour of Ball Bearings on Vibration Test Spindles," IMAC - Proceedings of the 16th International Modal Analysis Conference, pp. 788-794.

[40] Sassi, S., Badri, B., and Thomas, M., 2007, "A Numerical Model to Predict. Damaged Bearing Vibrations," Journal of Vibration and Control, **13**(11), pp. 1603-1628.

[41] Karkkainen, A., Helfert, M., Aeschlimann, B., and Mikkola, A., 2008, "Dynamic Analysis of Rotor System with Misaligned Retainer Bearings," Journal of Tribology-Transactions of the Asme, **130**(2).

[42] Ashtekar, A., Sadeghi, F., and Stacke, L. E., 2008, "A New Approach to Modeling Surface Defects in Bearing Dynamics Simulations," Journal of Tribology-Transactions of the Asme, **130**(4).

[43] Ashtekar, A., Sadeghi, F., and Stacke, L. E., 2010, "Surface Defects Effects on Bearing Dynamics," Proceedings of the Institution of Mechanical Engineers Part J-Journal of Engineering Tribology, **224**(J1), pp. 25-35.

[44] Isermann, R., 2005, "Model-Based Fault-Detection and Diagnosis - Status and Applications," Annual Reviews in Control, **29**(1), pp. 71-85.

[45] Kim, J., and Bryant, M. D., 1999, "Bond Graph Models of a Squirrel Cage Induction Motor and a Layshaft Gearbox for Degradation Analysis," Ph.D. thesis, The University of Texas at Austin, Austin.

[46] Kim, J., and Bryant, M. D., 2000, "Bond Graph Model of a Squirrel Cage Induction Motor with Direct Physical Correspondence," Journal of Dynamic Systems, Measurement, and Control, **122**(3), pp. 461-469.

[47] Lee, S. H., and Bryant, M. D., 2000, "Model Based Diagnostic Methods for a Squirrel Cage Induction Motor," Ph.D. thesis, The University of Texas at Austin, Austin.

[48] Hubbard, M., 1979, "Whirl Dynamics of Pendulous Flywheels Using Bond Graphs," Journal of the Franklin Institute, **308**(4), pp. 405-421.

[49] Oh, J. S., 2003, "An Extended Bond Graph Model of a Squirrel Cage Induction Motor," Ph.D. thesis, The University of Texas at Austin, Austin.

[50] Choi, J., Nakhaeinejad, M., and Bryant, M. D., 2007, "Induction Motor and Centrifugal Pump Bond Graph Models for Model Based Fault Detection," ICBGM' 07, *Proceeding of the Conf. on Bond Graph Modeling*, San Diego, CA.

[51] Southall, B., F., B. B., and Marchant, J. A., 1998, "Controllability and Observability: Tools for Kalman Filter Design," eds., **1**, pp. 164-183.

[52] De Wit, C. C., Youssef, A., Barbot, J. P., Martin, P., and Malrait, F., 2000, "Observability Conditions of Induction Motors at Low Frequencies," Proceedings of the 39th Ieee Conference on Decision and Control, Vols 1-5, pp. 2044-2049.

[53] Ibarra-Rojas, S., Moreno, J., and Espinosa-Perez, G., 2004, "Global Observability Analysis of Sensorless-Induction Motors," Automatica, **40**(6), pp. 1079-1085.

[54] Li, M. W., Chiasson, J., Bodson, M., and Tolbert, L., 2005, "Observability of Speed in an Induction Motor from Stator Currents and Voltages," 2005 44th Ieee Conference on Decision and Control & European Control Conference, Vols 1-8, pp. 3438-3443.

[55] Stocks, M., and Medvedev, A., 2006, "On Observability and Controllability of Faulty Induction Machines," 2006 American Control Conference, **1-12**, pp. 4399-4405.

[56] Vaclavek, P., and Blaha, P., 2007, "Analysis of Observability Conditions for Ac Induction Machine Sensorless Control," 2007 Ieee International Symposium on Industrial Electronics, Proceedings, Vols 1-8, pp. 2262-2267.

[57] Samantaray, A. K., Medjaher, K., Bouamama, B. O., Staroswiecki, M., and Dauphin-Tanguy, G., 2006, "Diagnostic Bond Graphs for Online Fault Detection and Isolation," Simulation Modelling Practice and Theory, **14**(3), pp. 237-262.

[58] Liu, Y., and Cui, P., 2006, "Observability Analysis of Deep-Space Autonomous Navigation System," eds., pp. 279-282.

[59] Yim, J. R., Crassidis, J. L., and Junkins, J. L., 2005, "Autonomous Orbit Navigation of Two Spacecraft System Using Relative Line of Sight Vector Measurements," Spaceflight Mechanics 2004, Vol 119, Pt 1-3, **119**(pp. 2447-2460.

[60] Van Doren, J., Van Den Hof, P., Jansen, J., and Bosgra, O., 2008, "Determining Identifiable Parameterizations for Large-Scale Physical Models in Reservoir Engineering," Seol.

[61] Loron, L., and Laliberte, G., 1993, "Application of the Extended Kalman Filter to Parameters Estimation of Induction Motors," vol. 5, pp. 85-90.

[62] Ansuj, S., Shokooh, F., and Schinzinger, R., 1989, "Parameter Estimation for Induction Machines Based on Sensitivity Analysis," Industry Applications, IEEE Transactions on, **25**(6), pp. 1035-1040.

[63] Xiaoyao, Z., Haozhong, C., and Ping, J., 2002, "The Third-Order Induction Motor Parameter Estimation Using an Adaptive Genetic Algorithm," **2**, pp. 1480-1484.

[64] De Kock, J. A., Van Der Merwe, F. S., and Vermeulen, H. J., 1994, "Induction Motor Parameter Estimation through an Output Error Technique," Energy Conversion, IEEE Transactions on, **9**(1), pp. 69-76.

[65] Lindenmeyer, D., Dommel, H. W., Moshref, A., and Kundur, P., 2001, "An Induction Motor Parameter Estimation Method," International Journal of Electrical Power & Energy Systems, **23**(4), pp. 251-262.

[66] Pappano, V., Lyshevski, S. E., and Friedland, B., 1998, "Identification of Induction Motor Parameters," eds., **1**, pp. 989-994.

[67] Kim, K., and Parlos, A. G., 2002, "Model-Based Fault Diagnosis of Induction Motors Using Non-Stationary Signal Segmentation," Mechanical Systems and Signal Processing, **16**(2-3), pp. 223-253.

[68] Hilairet, M., Auger, F., and Berthelot, E., 2009, "Speed and Rotor Flux Estimation of Induction Machines Using a Two-Stage Extended Kalman Filter," Automatica, **45**(8), pp. 1819-1827.

[69] Jul-Ki, S., and Seung-Ki, S., 2001, "Induction Motor Parameter Tuning for High-Performance Drives," Industry Applications, IEEE Transactions on, **37**(1), pp. 35-41.

[70] Said, M. S. N., Benbouzid, M. E. H., and Benchaib, A., 2000, "Detection of Broken Bars in Induction Motors Using an Extended Kalman Filter for Rotor Resistance Sensorless Estimation," Energy Conversion, IEEE Transactions on, **15**(1), pp. 66-70.

[71] Karami, F., Poshtan, J., and Poshtan, M., 2010, "Detection of Broken Rotor Bars in Induction Motors Using Nonlinear Kalman Filters," Isa Transactions, **49**(2), pp. 189-195.

[72] Kallesoe, C. S., Vadstrup, P., Rasmussen, H., and Izadi-Zamanabadi, R., 2006, "Observer Based Estimation of Stator Winding Faults in Delta-Connected Induction Motors, a Lmi Approach," eds., **5**, pp. 2427-2434.

[73] Bhattacharyya, K., and Mukherjee, A., 2006, "Modeling and Simulation of Centerless Grinding of Ball Bearings," Simulation Modelling Practice and Theory, **14**(7), pp. 971-988.

[74] Nakhaeinejad, M., Lee, S. H., and Bryant, M. D., 2010, "Finite Element Bond Graphs of Rotors," ICBMG'10, *Proc. of International Conference on Bond Graph Modeling*, Orlando, FL.

[75] Harris, T., and Kotzalas, M., 2007, *Essential Concepts of Bearing Technology*, Taylor and Francis Group, Boca Raton, FL.

[76] Akturk, N., Uneeb, M., and Gohar, R., 1997, "The Effects of Number of Balls and Preload on Vibrations Associated with Ball Bearings," Journal of Tribology, **119**(4), pp. 747-753.

[77] Kramer, E., 1993, *Dynamics of Rotors and Foundations*, Springer, Berlin.

[78] Kragselsky, V., Dobychin, N., and Kombalov, S., 1982, *Friction and Wear: Calculated Methods*, Pergamon Press, Elmsford, NY.

[79] Gupta, P., 1984, *Advanced Dynamic of Rolling Elements*, Springer-Verlag, NY.

[80] Palmgren, A., 1959, *Ball and Roller Bearing Engineering*, Philadelphia.

[81] Shin, H., 2004, "Bearing Diagnosis Using Embedded Modeling Method and System Identification Technique," Ph.D. thesis, Rensselaer Polytechnic Institute, Troy, NY.

[82] Karnopp, D. C., Margolis, D. L., and Rosenberg, R. C., 2000, *System Dynamics: Modeling and Simulation of Mechatronic System*, Wiley, New York.

[83] Shabana, A. A., 2005, *Dynamics of Multibody Systems*, Cambridge University Press, Cambridge ; New York.

[84] Harris, T., and Kotzalas, M., 2007, *Advanced Concepts of Bearing Technology*, Taylor and Francis Group, Boca Raton, FL.

[85] Kurfess, T. R., Billington, S., and Liang, S. Y., 2006, Condition Monitoring and Control for Intelligent Manufacturing, Springer London, Advanced Diagnostic and Prognostic Techniques for Rolling Element Bearings.

[86] Ghosh, B. C., and Bhadra, S. N., 1993, "Bond Graph Simulation of a Current Source Inverter Driven Induction Motor (Csi–Im) System," Electric Machines & Power Systems, **21**(1), pp. 51 - 67.

[87] Park, R. H., 1929, "Two-Reaction Theory of Synchronous Machines Generalized Method of Analysis-Part I," American Institute of Electrical Engineers, Transactions of the, **48**(3), pp. 716-727.

[88] Ogata, K., 2002, *Modern Control Engineering*, Prentice Hall, Upper Saddle River, NJ.

[89] Hermann, R., and Krener, A., 1977, "Nonlinear Controllability and Observability," Automatic Control, IEEE Transactions on, **22**(5), pp. 728-740.

[90] Stroud, K. A., and Booth, D. J., 2003, *Advanced Engineering Mathematics*, Industrial Press, Inc.,

[91] Martins, J. R. R. A., Sturdza, P., and Alonso, J. J., 2003, "The Complex-Step Derivative Approximation," ACM Transactions on Mathematical Software, **29**(3), pp. 245-262.

[92] Brumback, B. D., and Srinath, M. D., 1987, "A Chi-Square Test for Fault-Detection in Kalman Filters," Ieee Transactions on Automatic Control, **32**(6), pp. 552-554.

# Vita

Mohsen Nakhaeinejad was born in Yazd, Iran on October 1978. In 1997, he entered the Manufacturing Engineering program at Amirkabir University (Tehran Polytechnic) and received his B.Sc. degree in Mechanical Engineering in 2001. Then, he joined graduate school at Sharif University of Technology in Tehran and received his M.S. in Mechanical Engineering in 2003. After few years working in industry, Mohsen joined the doctoral program in Mechanical Engineering at The University of Texas at Austin in 2005. During his graduate study, he was awarded the Journal Editorial Fellowship from the graduate school of The University of Texas at Austin, a fellowship from University of Texas Advanced Manufacturing Center, and two Professional Development award for his research contributions.

E-mail: mosenn@gmail.com

This dissertation was typed by the author.